IMPROVED ASSESSMENT OF READING NETWORKS IN THE BRAIN USING DIFFUSION MRI

By

Qiuyun Fan

Dissertation

Submitted to the Faculty of the

Graduate School of Vanderbilt University

in partial fulfillment of the requirements

for the degree of

DOCTOR OF PHILOSOPHY

in

Biomedical Engineering

May, 2013

Nashville, Tennessee

Approved:

Professor Adam W. Anderson

Professor John C. Gore

Professor Laurie E. Cutting

Professor Nicole Davis

Professor Bennett A. Landman

ACKNOWLEDGEMENTS

As a collaborative work, it would not be possible for me to finish this dissertation without the devotion and hard work of my colleagues in the DTI group. First, I would like to express my greatest gratitude to my advisor, Prof. Adam W. Anderson, for his support during my doctoral study. His knowledge, experience, and his patience and encouragement to me led me through the technical difficulties. Many of the personal lessons I have learned from him will prove to be as important in my professional career as the technical ones. The five years in his group have been a highlight in my life and opened my eyes to a lot of innovations and opportunities. Thank you, Prof. Anderson! I would thank Prof. Laurie E. Cutting and Prof. G. Nicole Davis in the Education and Brain Research Laboratory (EBRL) for guiding and financially supporting me in my study. I am truly grateful to Prof. John C. Gore, Prof. Bennett Landman, Prof. Zhaohua Ding, Dr. Ha-Kyu Jeong, Dr. Xin Hong, Dr. Ann Choe, and Dr. Yurui Gao. They have been very kind to me in both research and my personal life and took the time to mentor me in my projects. I am also thankful to my colleagues in EBRL. Prof. Sheryl L. Rimrodt, Heather Harris, Aparna Pisupati, Laura Barquero, Lindsay M. Wilson, Scott Burns and Julie Delheimer helped me in many of my research activities. Last but not least, I express my deepest love to my family. My parents and my boyfriend gave me love and joy.

TABLE OF CONTENTS

Page

LIST OF TABLES

LIST OF FIGURES

CHAPTER I

INTRODUCTION

1.1. Overview

Diffusion tensor imaging (DTI) is a relatively new MR technique to study the white matter structures of the brain non-invasively. White matter fiber bundles, as the information transfer pathway between cortical regions, play an important role in mediating cognitive functions. Reading ability is one of such cognitive function, which relies on the cooperation of extended brain regions. Recently, DTI has been used to study white matter properties related to reading abilities, and has become an important neurobiological tool to study the mechanisms of dyslexia.

In this chapter, the following topics will be covered: (1) the basic principles of diffusion weighted MRI and DTI; (2) current opinions in reading and related DTI findings, challenges in the field and currently available HARDI techniques; and (3) goals and contributions of this dissertation.

1.2. Diffusion MRI

1.2.1. Diffusion weighted magnetic resonance imaging

Diffusion refers to the random translational motion of particles driven by thermal energy. Biological systems are comprised of an abundance of water. Under the assumption of Brownian motion, the displacement of a particular water molecule and the time allowed for it to diffuse, t, can be related through the Einstein's formula,

$$< r >= \sqrt{nDt}$$

where $< r >$ is the root mean square displacement, D is the diffusion coefficient, and n is determined by dimensionality (i.e., n = 2 for one dimensional diffusion, 4 for two dimensions and 6 for three dimensions). In a biological sample, however, the measured diffusion coefficient is the ensemble average of all the water molecules within the voxel, so the averaged diffusivity along an arbitrary direction is named the *apparent diffusivity*, or apparent diffusion coefficient (ADC) to distinguish from the intrinsic diffusion coefficient from pure water.

The extent of Brownian motion during a given time period, characterized by the ADC, can be measured by diffusion weighted imaging techniques. The Pulsed Gradient Spin Echo (PGSE) experiment makes the MR signal amplitude sensitive to diffusion

(Stejskal and Tanner, 1965) (Fig. 1.1): the intensity of the spin echo, S, is attenuated with respect to the baseline signal without diffusion weighting, S_0, via the relation,

$$\frac{S}{S_0} = e^{-bD_{app}}$$

where D_{app} is the ADC, and $b = \gamma^2 G^2 \delta^2 (\Delta - \frac{\delta}{3})$ is the diffusion weighting factor, or b factor, which depends on the gyromagnetic ratio γ, the amplitude of the gradient pulse G, pulse duration δ, and the time interval Δ between the de-phasing and refocusing gradient pulses .

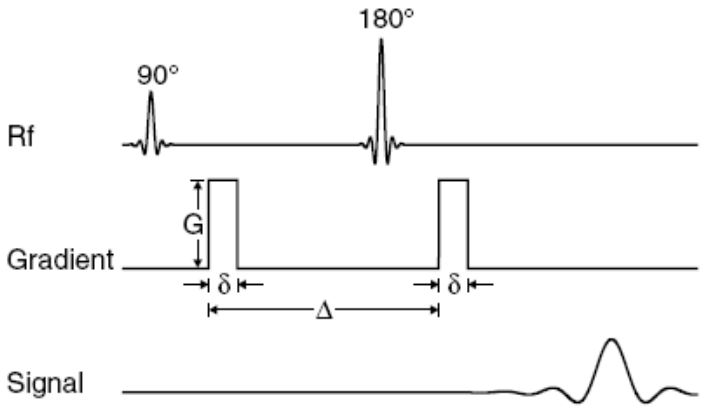

Figure 1.1. PGSE experiment diagram. A pair of identical diffusion sensitizing gradient pulses is applied along a prescribed direction before and after the 180° RF pulse. Spins are phase-encoded by their initial positions due to the first gradient pulse, and then allowed to diffuse freely for a time interval Δ. After the 180° RF pulse, the second gradient pulse of the same amplitude G and duration δ is aimed to cancel the position dependent phase if the spins remain stationary during the time interval Δ (Stejskal and Tanner, 1965).

Another aspect of diffusion is directionality. In an isotropic medium, such as in

the CSF of the ventricular system (Basser and Pierpaoli, 1996), a water molecule has equal chance to be displaced along any direction. The measured ADCs are identical when the diffusion sensitizing gradient is applied in different directions. However, in other tissues like white matter fiber bundles, where axons are wrapped with low permeability myelin membranes and are normally coherently oriented, diffusion is direction-dependent: apparent diffusivities are higher along the axons' orientation than perpendicular to them (Moseley, et al., 1990; Pierpaoli and Basser, 1996). In this case, the diffusion can no longer be characterized by a single scalar value of ADC, so a more complex model is needed to describe the anisotropic diffusion.

1.2.2. The diffusion tensor

With the assumption of Gaussian diffusion, the displacements of water molecules can be represented by a diffusion tensor (Basser et al., 1994), a 3x3 symmetric matrix, i.e.,

$$\boldsymbol{D} = \begin{bmatrix} D_{xx} & D_{xy} & D_{xz} \\ D_{xy} & D_{yy} & D_{yz} \\ D_{xz} & D_{yz} & D_{zz} \end{bmatrix}$$

where the elements on the diagonals are the apparent diffusivities along the three orthogonal axes of any arbitrary three dimensional coordinate system, and the off-diagonal elements are the covariance between molecular displacements in orthogonal

directions.

The eigenvalues of the tensor have physical meanings – the apparent diffusivities along the three primary axes of the diffusion tensor. The eigenvector corresponding to the largest eigenvalue, λ_1, is in the direction of primary (fastest) diffusion. The envelope of the tensor ellipsoid (Fig. 1.2) depicts the isosurface of the mean squared probability density function (PDF) of a spin's molecular displacements.

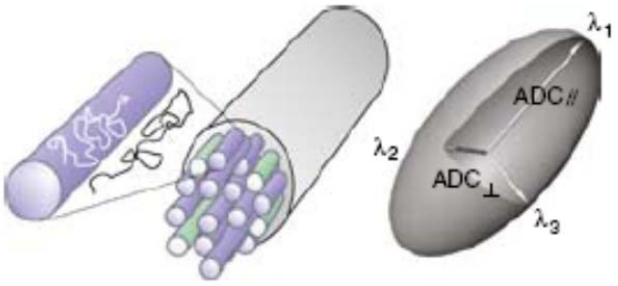

Figure 1.2. Ellipsoidal representation of the diffusion tensor. The envelope of the tensor ellipsoid depicts the iso-surface of the mean squared probability density function (PDF) of a spin's molecular displacements. The axes of the ellipsoid are scaled by the eigenvalues of the diffusion tensor (Beaulieu, 2009).

The diffusion tensor provides important information about the microscopic composition, structure and organization of the tissue under study. Fractional anisotropy (FA) (Basser and Pierpaoli, 1996; Beaulieu, 2002) is one of the most widely used scalar values derived from the eigenvalues of the diffusion tensor to quantify how much the diffusion envelope deviates from a sphere. For isotropic tissue samples, FA is close to 0,

while for very anisotropic samples, the corresponding diffusion tensor will be stretched towards poles that are oriented in the direction of the fiber bundle's orientation, and the FA can be close to 1. More often than not, a decreased FA is related to tissue damage or diseased status (Beaulieu et al., 1996) (Fig. 1.3). In addition, the principal diffusion direction indicated by the eigenvector corresponding to the largest eigenvalue of the diffusion tensor is assumed to be consistent with the orientation of the underlying structure, which becomes the basis of DTI-tractography (Mori and van Zijl, 2002; Lori et al., 2002).

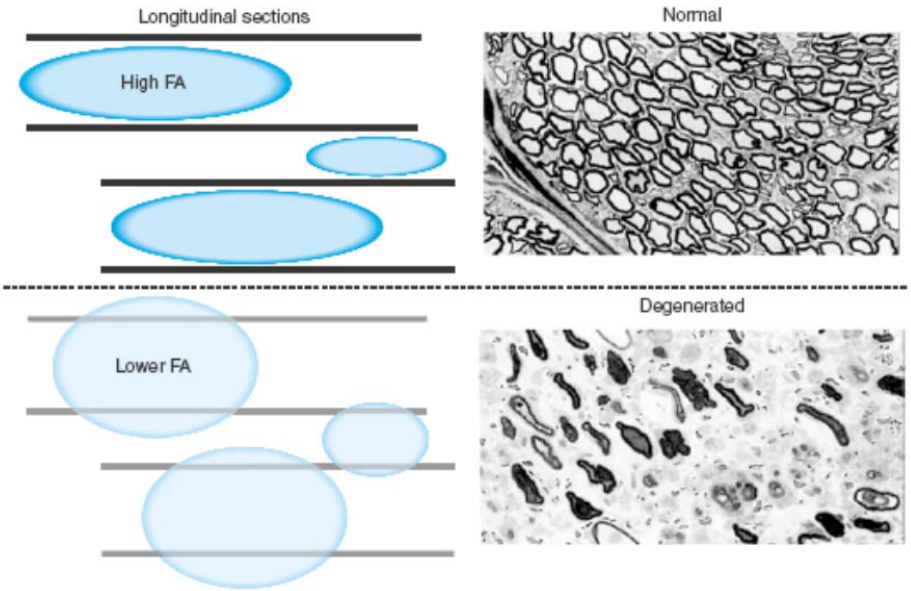

Figure 1. 3. Illustration of FA indicative of structural damage. On the left is a cartoon illustration of reduced anisotropy due to damage in axons and myelin that result in a loss of directional barriers to water diffusion. On the right, electron micrographs are adapted from normal and degenerated frog sciatic nerve (Beaulieu et al., 1996).

1.2.3. High angular resolution diffusion imaging

Despite the valuable information it can provide in white matter studies, DTI suffers from some fundamental limitations (Wiegell et al., 2000). Typical axon diameters range from less than 1 micron to more than 30 microns in the human brain, but the voxel size of a DTI acquisition for human studies on a modern MR scanner is usually 2-3 millimeters. Consequently, voxels in the white matter contain many thousands of axons and some voxels contain more than one fiber bundle. In this case, the conventional second-order tensor model which is based on the assumption of Gaussian diffusion is not able to describe non-Gaussian diffusion adequately, and thus is not able to provide reliable estimates of the underlying principal orientation and diffusion anisotropy of each fiber component.

In order to resolve complex white matter structure and address the problem of the partial volume effect, new imaging techniques and data reconstruction methods have been developed. High Angular Resolution Diffusion Imaging, or HARDI, (Tuch et al., 2002; Alexandeer et al., 2002; Frank, 2001; Ozarslan and Mareci, 2003) is a set of these methods.

To extract diffusion properties and reveal tissue micro-structural information from the HARDI signal, several different reconstruction schemes have been developed,

including the multiple tensor model (Tuch et al., 2002), generalized tensor model (Ozarslan and Mareci, 2003; Liu et al., 2004), spherical harmonic decomposition of the ADC profile (Alexander et al., 2002; Frank, 2002), spherical harmonic deconvolution (Tournier et al., 2004, 2008; Anderson, 2005), circular spectrum mapping (Zhan et al., 2004), Diffusion Spectrum Imaging (DSI, Wedeen et al., 2005), Q-Ball Imaging (QBI, Tuch et al, 2003; Tuch 2004), iterative spherical deconvolution (Dell' Acqua, et al., 2007, 2010), combined hindered and restricted model of water diffusion (Assaf et al., 2005, 2008), ensemble average propagator (EAP) (Descoteaux et al, 2009, 2011), etc. Although these techniques are capable of resolving multiple intra-voxel fiber directions, few of them provide information about the intrinsic diffusion properties of the fibers. Thus in cases where FA is altered, it is impossible to determine if the altered FA resulted from changes in the intrinsic diffusivity or fiber orientation.

The CHARMED (Assaf et al., 2005) and the AxCaliber (Assaf et al., 2008) methods are one family of the few successful trials to estimate diffusive properties of individual fiber compartments. AxCaliber builds upon CHARMED, and provides axon diameter density estimates by assuming the axon density obeys a Gamma distribution. A restriction of AxCaliber is that it only applies to single fiber bundle. Another approach that models the displacements of water molecules due to diffusion is EAP. EAP provides

a description of the location of water molecules under multiple experimental conditions, i.e. different *b* values, in a probabilistic framework. It's successful in revealing the basic physical process of diffusion directly, but lacks a straightforward biological interpretation in a tissue specimen. Both methods require measurement over a large range of *b* values, and the prohibitively long scanning time restricts their application to human studies.

Among the HARDI methods that don't measure diffusive properties of fiber bundles, spherical deconvolution is one of the most popular used to resolve organizational properties of white matter tissue using a spherical harmonic (SH) transformation. The basic idea is that the measured signal is the sum of contributions from all the individual fiber components within a voxel. In a single fiber bundle case, the amount of signal loss due to diffusion can be measured along different orientations, which is also called the single fiber response kernel. In a more complicated case, where the organization of multiple fiber bundles can be represented by a Fiber Orientation Distribution (FOD) function, the measured signal is the FOD function convolved with the corresponding single fiber response kernel. If the response kernels of all compartments are the same, once the response function is estimated, the fiber distribution can be reconstructed by deconvolution. Tournier et al. estimated the response function from a group of voxels with the highest FA in the whole dataset, and then calculated the ODF by

deconvolution (Tournier et al., 2004). In practice, there is a discrepancy between this assumed common response function and the real underlying tissue properties, which renders the algorithm vulnerable to “calibration” errors (Parker et al., 2012).

Instead of using a single response function for the whole brain, FORECAST (Anderson, 2005) estimates the response function for each voxel. The FORECAST model shows several advantages over the other methods that need to be mentioned. First, by expressing functions in SHs, the FORECAST model is computationally efficient, involving only linear matrix calculation, avoiding integration or interpolation. Second, FORECAST is capable of distinguishing two different causes of decreased FA, changes in fiber coherence and fiber intrinsic diffusivity to some extent. A drawback of FORECAST, however, is the assumption that all fiber compartments share common diffusivities. Therefore, it is difficult to determine which fiber bundle is responsible for the altered FA.

1.2.4. MR tractography

Tractography is the process of integrating voxelwise fiber orientations into a pathway that connects remote brain regions. It relies on the fundamental assumption, that the water diffusion is least restricted along the axes of axons, if the neural fibers are

coherently aligned along a common axis. Tractography algorithms can be local or global, deterministic or probabilistic, model based or model free; they can rely on simple (Mori et al., 1999) or complex (Parker and Alexander, 2003, 2005) representations of diffusion in white matter. This section briefly reviews DTI based fiber tracking techniques involved in this study, including streamline tractography and probabilistic tractography.

The most intuitive and commonly used fiber tracking technique is streamline tractography (Mori et al., 1999). From the previous sections we know that on the voxel level, a principal diffusion direction can be estimated by DTI and is assumed to be collinear with the neuronal fiber bundle axis. By starting at an appropriate seed point (i.e., in the middle of a well-organized fiber bundle), a streamline representation of the bundle can be reconstructed by following local vector information on a step-by-step basis. Since fiber tracking is an integration process, the reconstruction accuracy is very susceptible to errors in local vector estimates. To limit false positives, the algorithm is stopped when the front of the streamline steps into a local area where the directional uncertainty is above a preset threshold. This directional uncertainty is often parametrized as hypo-intensity in FA maps, which may due to various causes such as low SNR, partial volume effects at boundaries of white matter and gray matter or at the intersection of multiple fiber bundles, etc. Another criterion for a streamline to stop is high curvature of a streamline, because it

is assumed that no sharp turns exist in deep white matter. The employment of spatial interpolation (Mori et al., 1999; Lazar and Alexander, 2003; Pajevic et al., 2002) can overcome, to some degree, the effects of noise in the local orientation estimates and improve the smoothness of reconstructed fiber tracts, but a simple streamline algorithm is still very vulnerable to error accumulation due to its deterministic nature. Probabilistic algorithms have been recently proposed to be more robust to regions with high uncertainty. These approaches repetitively sample from distributions of voxel-wise principal diffusion directions, each time computing a streamline through these sampled local estimates to generate a sample of the true streamline. By taking many such samples, the posterior distribution of the streamline or the connectivity distribution at a location can be built up (Behrens et al., 2007). Both deterministic and probabilistic tractography have been used to study the neuronal networks that support cognition and how changes in these networks relate to cognitive disorders.

1.3. Opportunities and challenges of DTI in reading studies

1.3.1. Current opinions in reading and related DTI findings

Dyslexia is a developmental reading disorder that affects a significant number (5-

17%) of individuals. It is characterized by deficits in phonological processing which consequently impede the development of adequate word recognition or decoding. These deficits are specific, and are present despite adequate instruction and intelligence (Lyon, 1995; Shaywitz, 1998). While the behavioral characteristics of dyslexia are fairly well known, the neurobiological characteristics of this disorder are still under examination. Note that in the reading research literatures so far, the term of dyslexia have been used to refer to populations with slightly different behavioral characteristics. To clarify the definition of dyslexia, in this dissertation, we use the term dyslexia to refer to the child population who has lower reading skills and difficulties in word recognition. With the advent of neuroimaging, especially functional MRI (fMRI), over the last two decades in particular, studies have mapped the areas in the brain that are associated with good and poor reading. Converging findings reveal that proficient reading performance is associated with a coordinated left hemisphere network that involves temporo-parietal, occipitotemporal, inferior frontal and anterior perisylvian regions, including sensorimotor, premotor, pars opercularis and triangularis (Broca's) areas (Heilman et al., 1996).

Serving as the information transfer pathways for this complicated network are the white matter bundles. Normally, it takes approximately one fifth of a second for the brain to finish the whole process from seeing a string of letters, recognizing it as a language

notion, to recall its meaning (Tarkiainen et al., 2002). Since reading relies so much on information transfer between cortical regions, how white matter properties affect reading performance becomes a key in understanding how the brain functions to mediate reading behavior.

Current research supports the hypothesis that white matter structure variations in individuals are behaviorally relevant and that they can be studied in vivo with DTI. In fact, differences in white matter have been shown in several studies comparing children with reading difficulty to normal readers (Beaulieu et al., 2005; Deutsch et al., 2005; Klingberg et al., 2000; Niogi and McCandliss, 2006), where significant differences in white matter integrity were reported in temporal-parietal regions. Lower FA in the left Corona Radiata (CR) / Superior Longitudinal Fasciculus (SLF) is consistently reported, and was considered to be relevant to poor reading performance. Although a precise prediction of functional and behavioral consequences of white matter changes is still hard to make, more and more evidence suggests that white matter properties such as myelination, packing density, and fiber coherence might affect behavior by modulating information transfer across brain networks. Specific for reading, how strongly the cortical regions within the Perisylvian territories are connected to each other appears to be associated with reading ability.

1.3.2. Mapping the visual word form area connectivity patterns

As mentioned earlier, functional MRI (fMRI) studies have mapped the areas in the brain that are associated with good and poor reading. Regarding visual orthographic conversion, in particular, a region in the left ventral occipitotemporal region is reproducibly found to be selectively responsive of written strings relative to other categories such as line drawings. This region is known as the putative visual word form area (VWFA, Cohen, 2000). Evidence in support of the finding is seen in lesion studies (Epelbaum et al, 2008; Mandonnet et al., 2009), PET (Petersen et al., 1990; Price et al., 1996), fMRI and ERP studies (Braet et al., 2012; Brem et al., 2006, 2009, 2010; Cohen et al., 2002), and the locations reported converge fairly well to the left occipitotemporal sulcus bordering the fusiform gyrus.

Reading is a complex cognitive behavior, which requires the cooperation of a number of brain regions. On this view, despite the abundance of domain-specific findings within the VWFA, little is known about the role of VWFA in the network of reading related regions. Not until recently have researchers started to look into the structural aspects of the VWFA, aiming to explore its connections to other language related brain regions in normal German speaking children (Yeatman et al., 2012). The findings of this

study bring the field a step forward by answering the question: what physical connections are available for the VWFA to communicate with the rest of the brain? However, it is still unclear what feature(s) of the connections are crucial for word form recognition. Or as Dehaene and Cohen (Dehaene and Cohen, 2011) suggest as research direction for the field in the future, 'can its connectivity pattern explain its specific role in written word recognition'?

The network intrinsic to visual word form processing has not yet been established. However, the VWFA connectivity profile of each individual, estimated by DTI and tractography, can be analyzed together with the individual's behavioral profiles. Specifically, a recent study (Saygin et al., 2012) has shown by combining DTI and fMRI data, the technique was precise enough to predict fMRI activation with structural connectivity estimated by probabilistic tractography in the fusiform face area (FFA, right fusiform gyrus, Kanwisher et al., 1997; Barton et al., 2002; Pitcher et al., 2007). Coincidentally, the putative VWFA, as reported in previous studies, is located in a contralateral homologous region as FFA. All these findings put together indicate that the VWFA connectivity profile might already contain enough information to differentiate between good and poor readers. The purpose of the current work was to examine VWF-system structural connectivity patterns in children with and without reading difficulty.

1.3.3. Revealing thalamic connectivity related to reading

While the primary focus of neuroimaging work to date in dyslexia has been on cortical regions, more recently there has been an interest in subcortical regions. The thalamus acts as an information processing way station for the brain, relaying signals contributing to the regulation of arousal (Portas et al., 1998) and cognition (Johnson and Ojemann, 2000; Karussis et al., 2000). It is logical that there would be connections between the thalamus and reading related areas, and the activity of the output region is likely mediated by thalamic activity and/or thalamo-cortical connectivity. Previous studies have reported individual variability in functional (Díaz et al., 2012; Fiebach et al., 2002; Hoeft et al., 2007; Preston et al., 2010; Price et al., 1994; Turkeltaub et al., 2002) and structural (e.g., Galaburda and Eidelberg, 1982) aspects of the thalamus that relate to differences in reading skills, suggesting linkages between the thalamus and reading ability. However, whether the thalamo-cortical connectivity is related to reading ability remains unclear.

DTI and tractography have made it possible to study the relationship between thalamo-cortical connectivity and reading ability. Good agreement has been shown between the thalamic subdivisions identified by connectivity estimated by DT-

tractography and subdivisions defined by cytoarchitecture (Johansen-Berg, 2005). Furthermore, the tractography defined thalamo-cortical connectivity has been shown to be able to reveal structural alterations in patients, such as those with Alzheimer's disease (Zarei, 2010) and schizophrenia (Marenco, 2012). Another purpose of the current work was to investigate the potential relationship between thalamo-cortical connectivity and children's reading ability, by the use of diffusion tractography.

1.3.4. Challenges in reading studies

Despite the success of DTI in finding abnormal FA in the CR/SLF area in individuals with reading difficulty, the interpretation of these findings remains ambiguous due to some of its fundamental limitations (Wiegell et al., 2000). Namely, in the region where CR and SLF cross, the typical voxel size of DW MRI scans is about (2~3 mm^3), which may contain tissues from both fiber bundles. As a result, in order to study the integrity intrinsic to each fiber bundle, a model more complex than DTI is needed to better represent the white matter structures.

As mentioned earlier, HARDI techniques were developed to represent crossing structures. These methods include Diffusion Spectrum Imaging (DSI, Wedeen et al., 2005), Q-Ball Imaging (QBI, Tuch et al, 2003; Tuch 2004), spherical harmonic

deconvolution (Tournier et al., 2004, 2007, 2008), and iterative spherical deconvolution (Dell' Acqua, et al., 2007, 2010). Although these techniques are capable of resolving multiple intra-voxel fiber directions, few of them provide information about the intrinsic diffusion properties of the fibers. Thus in cases where FA is altered, it is impossible to determine if the altered FA resulted from changes in the intrinsic diffusivity or fiber orientation. As mentioned earlier, AxCaliber (Assaf et al., 2008), which was built upon CHARMED (Assaf et al., 2005), provides axon diameter density estimates by assuming the axon diameter density obeys a Gamma distribution. However, the methods require measurement over a large range of q values (max. q = 89.4 mm^{-1}, equivalent to b = 44000 s/mm^2 for CHARMED and max. q = 51.1 mm^{-1}, equivalent to b = 15320 s/mm^2 for AxCaliber), and the long scanning time (CHARMED 18 hours, AxCaliber 30 hours) restricts their applications to *in vivo* human studies.

In summary, as partial volume averaging may take place in the CR/SLF area, it is difficult to determine the real cause of the decreased FA value: Do structural alterations occur in the CR, SLF, both or none? Is it different crossing angle or partial volume averaging between CR and SLF that makes the difference? Both DTI and currently available HARDI techniques are unable to provide a solution to answer these questions. In order to address the problem, new techniques need to be developed to provide more

detailed information.

1.4. Goals and contributions of this dissertation

1.4.1. Overall goal and specific aims

The overall goal of this work is to investigate the neurocorrelates of reading in the brain. Within this scope, my work focuses on structural aspects of the reading circuits in the brain, which leads to three specific aims: (1) to map the cortical connectivity pattern in the VWFA to study contributions to visual word form recognition in the brain; (2) to investigate subcortical components in the reading system, such as the thalamus; and (3) to develop new MR techniques that have the potential to study the complex white matter structures implicated by the DTI findings.

1.4.2. Contributions of this dissertation

The main body of this dissertation is composed of three studies to address the three specific aims respectively. Chapter II examines the VWF-system connectivity pattern, and is the first study to examine the structural VWFA connectivity pattern in children ranging in reading ability. It provides a framework to analyze connectivity

patterns identified by DT-tractography with the flexibility of incorporating behavioral performance, opened a window for future exploration of the VWF-system, and can be useful for other neurobiological studies carried out in a similar manner. Chapter III examines thalamo-cortical connectivity as it relates to children's reading ability. This work applies existing MR techniques to studying reading mechanisms and adds knowledge to the field by providing a missing piece of information about the potential roles of subcortical structures, specifically the thalamus, in mediating reading behavior. Chapter IV proposes a MR method aimed to provide more detailed neurobiological properties of the complex white matter structures in the language network. The multiple kernel spherical deconvolution (MKSD) model proposed in this study is able to address the partial volume problem, and estimate the intrinsic diffusion properties and fiber orientation distribution (FOD) of each individual fiber bundle in a voxel. The framework has the flexibility to fit into different experimental settings in terms of signal-to-noise ratio (SNR) and scan time, and was demonstrated to provide stable diffusivity estimates in *in vivo* experiments.

REFERENCES

1. Alexander, D.C., Barker, G.J., Arridge, S.R., 2002. Detection and modeling of

non-Gaussian apparent diffusion coefficient profiles in human brain data. Magn Reson Med 48, 331-340.

2. Anderson, A.W., 2005. Measurement of fiber orientation distributions using high angular resolution diffusion imaging. Magn Reson Med 54, 1194-1206.

3. Assaf, Y., Basser, P.J., 2005. Composite hindered and restricted model of diffusion (CHARMED) MR imaging of the human brain. Neuroimage 27, 48-58.

4. Assaf, Y., Blumenfeld-Katzir, T., Yovel, Y., Basser, P.J., 2008. AxCaliber: a method for measuring axon diameter distribution from diffusion MRI. Magn Reson Med 59, 1347-1354.

5. Assaf, Y., Freidlin, R.Z., Rohde, G.K., Basser, P.J., 2004. New modeling and experimental framework to characterize hindered and restricted water diffusion in brain white matter. Magn Reson Med 52, 965-978.

6. Barton, J.J., Press, D.Z., Keenan, J.P., O'Connor, M., 2002. Lesions of the fusiform face area impair perception of facial configuration in prosopagnosia. Neurology 58, 71-78.

7. Basser, P.J., Mattiello, J., LeBihan, D., 1994. MR diffusion tensor spectroscopy and imaging. Biophys J 66, 259-267.

8. Basser, P.J., Pierpaoli, C., 1996. Microstructural and physiological features of tissues elucidated by quantitative-diffusion-tensor MRI. J Magn Reson B 111, 209-219.

9. Beaulieu, C., 2002. The basis of anisotropic water diffusion in the nervous system - a technical review. NMR Biomed 15, 435-455.

10. Beaulieu, C., 2009. The Biological Basis of Diffusion Anisotropy. In: Johansen-Berg, H., Timothy, B. (Eds.), Diffusion MRI from quantitative measurement to in-vivo neuroanatomy. Academic Press, 32 Jamestown Road, London NW1 7BY, UK

11. Beaulieu, C., Allen, P.S., 1996. An in vitro evaluation of the effects of local magnetic-susceptibility-induced gradients on anisotropic water diffusion in nerve. Magn Reson Med 36, 39-44.

12. Beaulieu, C., Plewes, C., Paulson, L.A., Roy, D., Snook, L., Concha, L., Phillips, L., 2005. Imaging brain connectivity in children with diverse reading ability. Neuroimage 25, 1266-1271.

13. Behrens, T.E., Berg, H.J., Jbabdi, S., Rushworth, M.F., Woolrich, M.W., 2007. Probabilistic diffusion tractography with multiple fibre orientations: What can we gain? Neuroimage 34, 144-155.

14. Braet, W., Wagemans, J., Op de Beeck, H.P., 2012. The visual word form area is organized according to orthography. Neuroimage 59, 2751-2759.

15. Brem, S., Bach, S., Kucian, K., Guttorm, T.K., Martin, E., Lyytinen, H., Brandeis, D., Richardson, U., 2010. Brain sensitivity to print emerges when children learn letter-speech sound correspondences. Proc Natl Acad Sci U S A 107, 7939-7944.

16. Brem, S., Bucher, K., Halder, P., Summers, P., Dietrich, T., Martin, E., Brandeis, D., 2006. Evidence for developmental changes in the visual word processing network beyond adolescence. Neuroimage 29, 822-837.

17. Brem, S., Halder, P., Bucher, K., Summers, P., Martin, E., Brandeis, D., 2009. Tuning of the visual word processing system: distinct developmental ERP and fMRI effects. Hum Brain Mapp 30, 1833-1844.

18. Cohen, L., Dehaene, S., Naccache, L., Lehéricy, S., Dehaene-Lambertz, G., Hénaff, M.A., Michel, F., 2000. The visual word form area: spatial and temporal characterization of an initial stage of reading in normal subjects and posterior split-brain patients. Brain 123 (Pt 2), 291-307.

19. Cohen, L., Lehéricy, S., Chochon, F., Lemer, C., Rivaud, S., Dehaene, S., 2002. Language-specific tuning of visual cortex? Functional properties of the Visual Word Form Area. Brain 125, 1054-1069.

20. Dehaene, S., Cohen, L., 2011. The unique role of the visual word form area in reading. Trends Cogn Sci 15, 254-262.

21. Dell'Acqua, F., Rizzo, G., Scifo, P., Clarke, R.A., Scotti, G., Fazio, F., 2007. A model-based deconvolution approach to solve fiber crossing in diffusion-weighted MR imaging. IEEE Trans Biomed Eng 54, 462-472.

22. Dell'acqua, F., Scifo, P., Rizzo, G., Catani, M., Simmons, A., Scotti, G., Fazio, F., 2010. A modified damped Richardson-Lucy algorithm to reduce isotropic background effects in spherical deconvolution. Neuroimage 49, 1446-1458.

23. Descoteaux, M., Deriche, R., Le Bihan, D., Mangin, J.F., Poupon, C., 2009. Diffusion propagator imaging: using Laplace's equation and multiple shell acquisitions to reconstruct the diffusion propagator. Inf Process Med Imaging 21, 1-13.

24. Descoteaux, M., Deriche, R., Le Bihan, D., Mangin, J.F., Poupon, C., 2011. Multiple q-shell diffusion propagator imaging. Med Image Anal 15, 603-621.

25. Deutsch, G.K., Dougherty, R.F., Bammer, R., Siok, W.T., Gabrieli, J.D., Wandell, B., 2005. Children's reading performance is correlated with white matter structure measured by diffusion tensor imaging. Cortex 41, 354-363.

26. Díaz, B., Hintz, F., Kiebel, S.J., von Kriegstein, K., 2012. Dysfunction of the auditory thalamus in developmental dyslexia. Proc Natl Acad Sci U S A 109, 13841-13846.

27. Epelbaum, S., Pinel, P., Gaillard, R., Delmaire, C., Perrin, M., Dupont, S., Dehaene, S., Cohen, L., 2008. Pure alexia as a disconnection syndrome: new diffusion imaging evidence for an old concept. Cortex 44, 962-974.

28. Fiebach, C.J., Friederici, A.D., Müller, K., von Cramon, D.Y., 2002. fMRI evidence for dual routes to the mental lexicon in visual word recognition. J Cogn Neurosci 14, 11-23.

29. Frank, L.R., 2002. Characterization of anisotropy in high angular resolution

diffusion-weighted MRI. Magn Reson Med 47, 1083-1099.

30. Galaburda, A.M., Eidelberg, D., 1982. Symmetry and asymmetry in the human posterior thalamus. II. Thalamic lesions in a case of developmental dyslexia. Arch Neurol 39, 333-336.

31. Heilman, K.M., Voeller, K., Alexander, A.W., 1996. Developmental dyslexia: a motor-articulatory feedback hypothesis. Ann Neurol 39, 407-412.

32. Hoeft, F., Meyler, A., Hernandez, A., Juel, C., Taylor-Hill, H., Martindale, J.L., McMillon, G., Kolchugina, G., Black, J.M., Faizi, A., Deutsch, G.K., Siok, W.T., Reiss, A.L., Whitfield-Gabrieli, S., Gabrieli, J.D., 2007. Functional and morphometric brain dissociation between dyslexia and reading ability. Proc Natl Acad Sci U S A 104, 4234-4239.

33. Johansen-Berg, H., Behrens, T.E., Sillery, E., Ciccarelli, O., Thompson, A.J., Smith, S.M., Matthews, P.M., 2005. Functional-anatomical validation and individual variation of diffusion tractography-based segmentation of the human thalamus. Cereb Cortex 15, 31-39.

34. Johnson, M.D., Ojemann, G.A., 2000. The role of the human thalamus in language and memory: evidence from electrophysiological studies. Brain Cogn 42, 218-230.

35. Kanwisher, N., McDermott, J., Chun, M.M., 1997. The fusiform face area: a module in human extrastriate cortex specialized for face perception. J Neurosci 17, 4302-4311.

36. Karussis, D., Leker, R.R., Abramsky, O., 2000. Cognitive dysfunction following thalamic stroke: a study of 16 cases and review of the literature. J Neurol Sci 172, 25-29.

37. Klingberg, T., Hedehus, M., Temple, E., Salz, T., Gabrieli, J.D., Moseley, M.E., Poldrack, R.A., 2000. Microstructure of temporo-parietal white matter as a basis for reading ability: evidence from diffusion tensor magnetic resonance imaging. Neuron 25, 493-500.

38. Lazar, M., Alexander, A.L., 2003. An error analysis of white matter tractography methods: synthetic diffusion tensor field simulations. Neuroimage 20, 1140-1153.

39. Liu, C., Bammer, R., Acar, B., Moseley, M.E., 2004. Characterizing non-Gaussian diffusion by using generalized diffusion tensors. Magn Reson Med 51, 924-937.

40. Lori, N.F., Akbudak, E., Shimony, J.S., Cull, T.S., Snyder, A.Z., Guillory, R.K., Conturo, T.E., 2002. Diffusion tensor fiber tracking of human brain connectivity: aquisition methods, reliability analysis and biological results. NMR Biomed 15, 494-515.

41. Lyon, G.R., 1995. Toward a definition of dyslexia. Annals of Dyslexia 45, 3-27.

42. Marenco, S., Stein, J.L., Savostyanova, A.A., Sambataro, F., Tan, H.Y., Goldman, A.L., Verchinski, B.A., Barnett, A.S., Dickinson, D., Apud, J.A., Callicott, J.H., Meyer-Lindenberg, A., Weinberger, D.R., 2012. Investigation of anatomical thalamo-cortical connectivity and FMRI activation in schizophrenia. Neuropsychopharmacology 37, 499-507.

43. Mori, S., Crain, B.J., Chacko, V.P., van Zijl, P.C., 1999. Three-dimensional tracking of axonal projections in the brain by magnetic resonance imaging. Ann Neurol 45, 265-269.

44. Mori, S., van Zijl, P.C., 2002. Fiber tracking: principles and strategies - a technical review. NMR Biomed 15, 468-480.

45. Moseley, M.E., Cohen, Y., Kucharczyk, J., Mintorovitch, J., Asgari, H.S., Wendland, M.F., Tsuruda, J., Norman, D., 1990. Diffusion-weighted MR imaging of anisotropic water diffusion in cat central nervous system. Radiology 176, 439-445.

46. Niogi, S.N., McCandliss, B.D., 2006. Left lateralized white matter microstructure accounts for individual differences in reading ability and disability. Neuropsychologia 44, 2178-2188.

47. Ozarslan, E., Mareci, T.H., 2003. Generalized diffusion tensor imaging and

analytical relationships between diffusion tensor imaging and high angular resolution diffusion imaging. Magn Reson Med 50, 955-965.

48. Pajevic, S., Aldroubi, A., Basser, P.J., 2002. A continuous tensor field approximation of discrete DT-MRI data for extracting microstructural and architectural features of tissue. J Magn Reson 154, 85-100.

49. Parker, G.D., Marshall, D., Rosin, P.L., Drage, N., Richmond, S., Jones, D.K., 2012. A pitfall in the reconstruction of fibre ODFs using spherical deconvolution of diffusion MRI data. Neuroimage 65C, 433-448.

50. Parker, G.J., Alexander, D.C., 2003. Probabilistic Monte Carlo based mapping of cerebral connections utilising whole-brain crossing fibre information. Inf Process Med Imaging 18, 684-695.

51. Parker, G.J., Alexander, D.C., 2005. Probabilistic anatomical connectivity derived from the microscopic persistent angular structure of cerebral tissue. Philos Trans R Soc Lond B Biol Sci 360, 893-902.

52. Petersen, S.E., Fox, P.T., Snyder, A.Z., Raichle, M.E., 1990. Activation of extrastriate and frontal cortical areas by visual words and word-like stimuli. Science 249, 1041-1044.

53. Pierpaoli, C., Basser, P.J., 1996. Toward a quantitative assessment of diffusion anisotropy. Magn Reson Med 36, 893-906.

54. Pitcher, D., Walsh, V., Yovel, G., Duchaine, B., 2007. TMS evidence for the involvement of the right occipital face area in early face processing. Curr Biol 17, 1568-1573.

55. Portas, C.M., Rees, G., Howseman, A.M., Josephs, O., Turner, R., Frith, C.D., 1998. A specific role for the thalamus in mediating the interaction of attention and arousal in humans. J Neurosci 18, 8979-8989.

56. Preston, J.L., Frost, S.J., Mencl, W.E., Fulbright, R.K., Landi, N., Grigorenko, E., Jacobsen, L., Pugh, K.R., 2010. Early and late talkers: school-age language,

literacy and neurolinguistic differences. Brain 133, 2185-2195.

57. Price, C.J., Wise, R.J., Frackowiak, R.S., 1996. Demonstrating the implicit processing of visually presented words and pseudowords. Cereb Cortex 6, 62-70.

58. Price, C.J., Wise, R.J., Watson, J.D., Patterson, K., Howard, D., Frackowiak, R.S., 1994. Brain activity during reading. The effects of exposure duration and task. Brain 117 (Pt 6), 1255-1269.

59. Saygin, Z.M., Osher, D.E., Koldewyn, K., Reynolds, G., Gabrieli, J.D., Saxe, R.R., 2012. Anatomical connectivity patterns predict face selectivity in the fusiform gyrus. Nat Neurosci 15, 321-327.

60. Shaywitz, S.E., 1998. Dyslexia. N Engl J Med 338, 307-312.

61. Stejskal, E.O., Tanner, J.E., 1965. Spin Diffusion Measurements: Spin Echoes in the Presence of a Time-Dependent Field Gradient. J. Chem. Phys. 42, 5.

62. Tarkiainen, A., Cornelissen, P.L., Salmelin, R., 2002. Dynamics of visual feature analysis and object-level processing in face versus letter-string perception. Brain 125, 1125-1136.

63. Tournier, J.D., Calamante, F., Connelly, A., 2007. Robust determination of the fibre orientation distribution in diffusion MRI: non-negativity constrained super-resolved spherical deconvolution. Neuroimage 35, 1459-1472.

64. Tournier, J.D., Calamante, F., Gadian, D.G., Connelly, A., 2004. Direct estimation of the fiber orientation density function from diffusion-weighted MRI data using spherical deconvolution. Neuroimage 23, 1176-1185.

65. Tournier, J.D., Yeh, C.H., Calamante, F., Cho, K.H., Connelly, A., Lin, C.P., 2008. Resolving crossing fibres using constrained spherical deconvolution: validation using diffusion-weighted imaging phantom data. Neuroimage 42, 617-625.

66. Tuch, D.S., 2004. Q-ball imaging. Magn Reson Med 52, 1358-1372.

67. Tuch, D.S., Reese, T.G., Wiegell, M.R., Makris, N., Belliveau, J.W., Wedeen, V.J., 2002. High angular resolution diffusion imaging reveals intravoxel white matter fiber heterogeneity. Magn Reson Med 48, 577-582.

68. Tuch, D.S., Reese, T.G., Wiegell, M.R., Wedeen, V.J., 2003. Diffusion MRI of complex neural architecture. Neuron 40, 885-895.

69. Turkeltaub, P.E., Eden, G.F., Jones, K.M., Zeffiro, T.A., 2002. Meta-analysis of the functional neuroanatomy of single-word reading: method and validation. Neuroimage 16, 765-780.

70. Wedeen, V.J., Hagmann, P., Tseng, W.Y., Reese, T.G., Weisskoff, R.M., 2005. Mapping complex tissue architecture with diffusion spectrum magnetic resonance imaging. Magn Reson Med 54, 1377-1386.

71. Wiegell, M.R., Larsson, H.B., Wedeen, V.J., 2000. Fiber crossing in human brain depicted with diffusion tensor MR imaging. Radiology 217, 897-903.

72. Yeatman, J.D., Rauschecker, A.M., Wandell, B.A., 2012. Anatomy of the visual word form area: Adjacent cortical circuits and long-range white matter connections. Brain Lang.

73. Zarei, M., Patenaude, B., Damoiseaux, J., Morgese, C., Smith, S., Matthews, P.M., Barkhof, F., Rombouts, S.A., Sanz-Arigita, E., Jenkinson, M., 2010. Combining shape and connectivity analysis: an MRI study of thalamic degeneration in Alzheimer's disease. Neuroimage 49, 1-8.

74. Zhan, W., Stein, E.A., Yang, Y., 2004. Mapping the orientation of intravoxel crossing fibers based on the phase information of diffusion circular spectrum. Neuroimage 23, 1358-1369.

CHAPTER II

THE STRUCTURAL CONNECTIVITY PATTERNS OF THE VISUAL WORD FORM AREA AND CHILDREN'S READING ABILITY

2.1. Introduction

A significant number (5-17%) of individuals are affected by dyslexia, a developmental reading disorder characterized by difficulty recognizing and decoding words, or with phonological to orthographic conversions despite adequate instruction and intelligence (Fletcher et al., 1998; Lyon, 1995; Shaywitz, 1998). While the behavioral characteristics of dyslexia are fairly well understood, the exploration of the underpinning neural mechanisms is still ongoing.

With the advent of neuroimaging techniques, especially functional MRI (fMRI), studies have mapped the areas in the brain that are associated with good and poor reading. Regarding visual orthographic conversion, in particular, a region in the left ventral occipitotemporal/fusiform region, known as the putative visual word form area (VWFA, Cohen et al., 2000; Petersen et al., 1988), is reproducibly found to be selectively responsive to written strings relative to other categories such as line drawings and is

thought to be important for fast and efficient word recognition (McCandliss et al., 2003). In contrast to this ventral word reading system, a dorsal route has been proposed as important for orthographic-to-phonological conversions (Pugh et al., 2000). Evidence in support of the ventral word reading system is seen in lesion studies (Epelbaum et al., 2008; Mandonnet et al., 2009), PET (Petersen et al., 1990; Price et al., 1996), fMRI and ERP studies (Braet et al., 2012; Brem et al., 2010; Brem et al., 2006; Brem et al., 2009; Cohen et al., 2002; Nestor et al., 2012; Rauschecker et al., 2011).

Despite the abundance in domain-specific findings within the VWFA, little is known about the role of the VWFA in terms of its structural connectivity to other reading related regions. While Diffusion Tensor Imaging (DTI) has been utilized in numerous neuroimaging studies to successfully relate brain connectivity patterns to its functions (Behrens et al., 2003a; Behrens et al., 2003b; Johansen-Berg et al., 2005; Marenco et al., 2012; Menke et al., 2010; Saygin et al., 2012; Zarei et al., 2010), fewer researchers have explored the structural aspects of occipitotemporal/fusiform regions using deterministic DT-tractography. Very recent studies have examined anatomical connections of the VWFA in an adult epilepsy patient (Epelbaum et al., 2008) and typically developed children (Yeatman et al., 2012), which reveal that peri-VWFA regions have connections to occipital cortex through the inferior longitudinal fasciculus and vertical occipital

fasciculus, and to perisylvian language areas through the arcuate fasciculus. Other studies have mapped regions homologous to the putative VWFA using analyses combining DTI and fMRI. Specifically, Saygin et al. (Saygin et al., 2012) showed by using probabilistic tractography that structural connectivity patterns can predict face selectivity revealed by fMRI in the fusiform face area (FFA; right fusiform gyrus, Barton et al., 2002; Kanwisher et al., 1997; Pitcher et al., 2007), suggesting that linking brain structure and function is feasible in the fusiform regions. Therefore, overall, the combined VWFA and FFA DTI literature suggest that the VWFA connectivity profile of each individual, estimated by DT-tractography, may reveal important neurobiological information related to reading development, and therefore that VWFA connectivity profiles may be able to differentiate between good and poor readers.

Here we examine, for the first time, VWF-system connectivity patterns along a posterior-anterior gradient as well as compare these connectivity patterns between children with reading disabilities (RD) and typically developing children (TD). In order to obtain a fine grained understanding of VWFA connectivity, five consecutive spherical regions of interest (ROI) were defined within the ventral occipitotemporal region, which was based upon the functional neuroimaging literature (Brem et al., 2009). These ROIs progressed along a posterior to anterior gradient along the putative VWFA (Fig. 2.1).

Within each ROI, we examined connectivity patterns to various cortical regions (Fig. 2.2). Based upon the previous literature, we had several hypotheses, including: (1) we would find different VWFA-cortical connectivity patterns across the five ROIs; (2) we would find different VWFA-cortical connectivity patterns for children with reading disabilities (RD) versus those who were typically developing readers (TD); and finally, (3) the group differences would be differences in relative emphasis of connectivity to more basic visual areas versus those putatively involved in the fast and effective ventral pathway for word recognition.

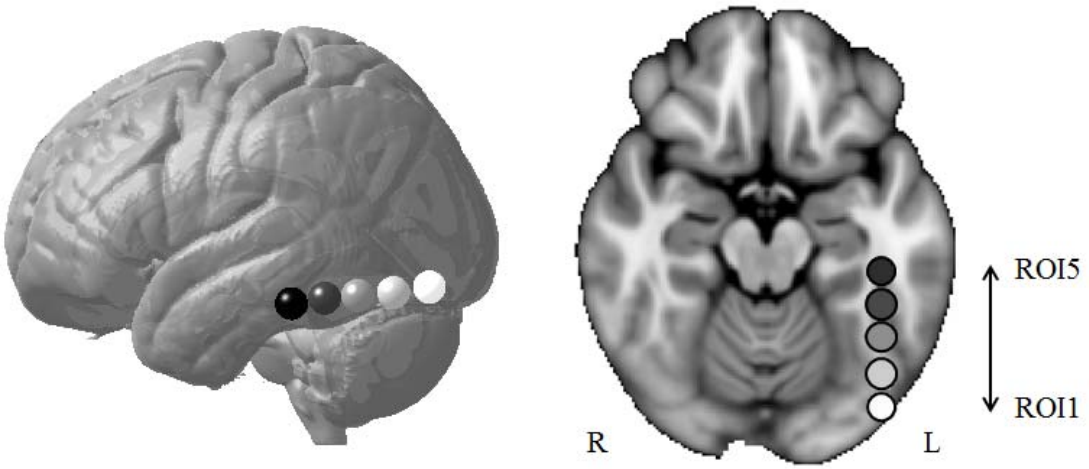

Figure 2.1. Illustration of five ROIs in the VWF-system. The five ROIs progress along a posterior to anterior gradient, each with a radius of 6 mm. The brightest ROI was numbered 1, and the 3rd ROI in the middle represents the putative VWFA.

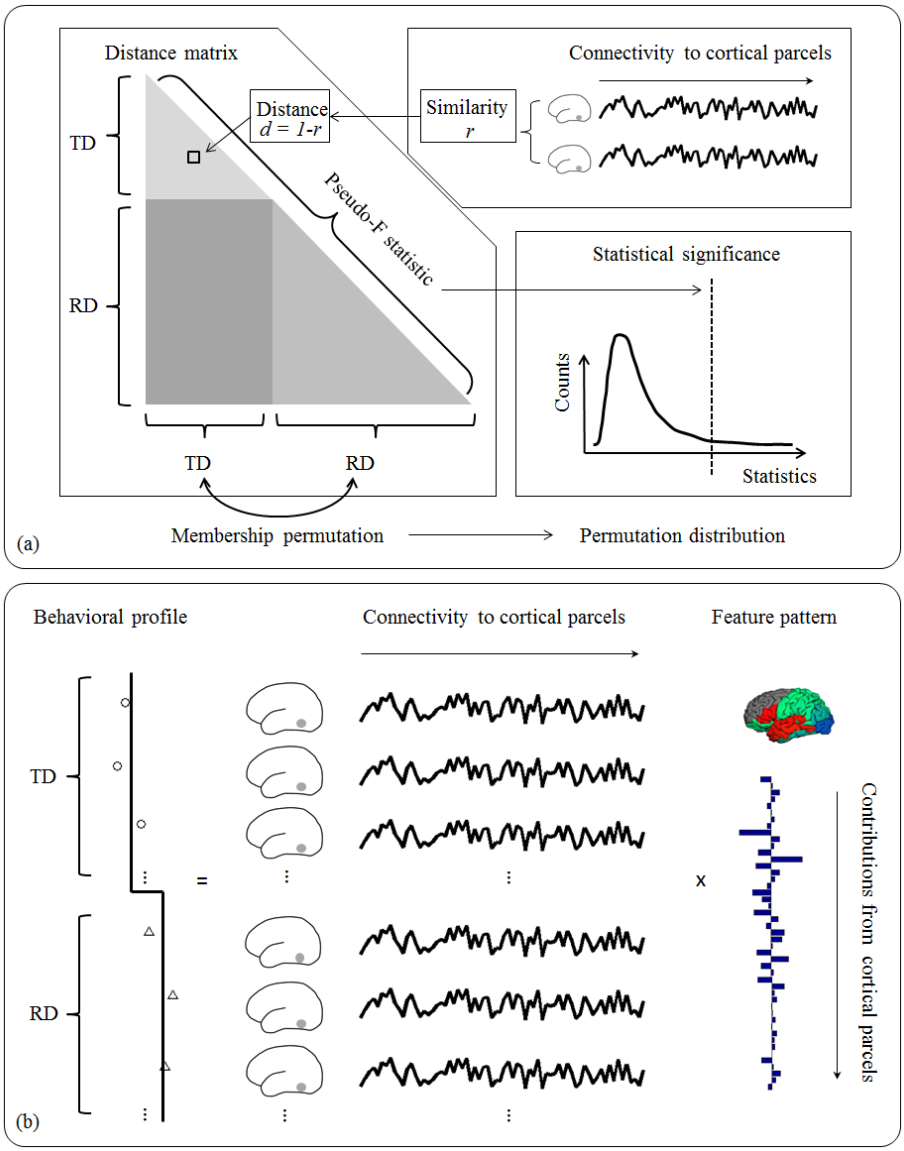

Figure 2.2. Schematic method design. We bear two questions in mind: (a) whether there is a group difference in connectivity pattern; and (b) if so, what is the feature pattern that best differentiates between groups. To answer question (a), we performed a distance-based permutation test, where correlation coefficient was computed pair-wisely to estimate similarity. Distance, or dissimilarity, was calculated as one minus similarity. The triangular matrix yielded a single value of *pseudo-F* statistic that estimates how well group membership explains the distances between individuals. Then group membership was permuted to build a *pseudo-F* distribution and determine statistical significance. If a significant difference was found, a linear regression of group membership onto connectivity profiles was performed to compute cortical contributions to group difference (b).

2.2. Methods

2.2.1. Participants

A total of 50 children participated in this study, and 4 were excluded due to imaging artifacts. All of these children are right handed, and 20 were female. Before entering the study, parents of children were administered an informal screening measure over the phone to ensure that participants met the study's inclusionary criteria: 1) native English speakers, 2) normal hearing and vision, 3) no history of major psychiatric illness, 4) no traumatic brain injury/epilepsy, and 5) no contraindication to the MRI. Each parent gave written consent while a separate written assent was obtained from each child at the start of the study, with procedures carried out in accordance with the university's Institutional Review Board. During their visit, participants were given a comprehensive battery of psychoeducational and academic achievement measures. Each individual received the Wechsler Intelligence Scale for Children-III (WISC-III; Wechsler, 1991) to determine eligibility based upon FSIQ criteria. Eligible participants completed a battery of standardized tests to determine reading ability (RD or TD). The behavioral measurement battery consisted of the following standardized measures of intellectual and academic achievement: the Test of Silent Contextual Reading Fluency (TOSCRF-Form A;

Hammill et al., 2006); Phonological Decoding Efficiency (PDE) and Sight Word Efficiency (SWE) from the Test of Word Reading Efficiency (TOWRE; Torgesen et al, 1997); and Word Attack (WA), Word Identification (Word ID), and Passage Comprehension (PC) subtests from the Woodcock Johnson –III (WJ-III; Woodcock, 2001; Woodcock et al., 2003).

Participants met criteria for RD if they had a standard score at or below the 25th percentile on the Basic Reading Composite (BR) on the WJ-III, which consists of the Word ID and WA measures. Participants met criteria to be TD by having a standard score at or above the 37th percentile on the BR. Of the eligible participants, 17 met criteria for RD and 24 met criteria for TD.

The two groups of children were not significantly different in age, gender or non-verbal IQ. Multivariate ANOVA (MANOVA) showed their behavioral profiles related to reading and language skills were significantly different ($F[1, 26] = 6.257$, $p < 0.001$, ($\eta_p^2 = 0.684$)). There were no significant difference in there behavioral profiles otherwise. See Table 2.1 for detailed demographic and behavioral profiles.

Table 2. 1. Demographic and neuropsychological profiles of each group (mean ± S.E.M.)

	TD	RD	p	η_p^2
Demographic and General Intelligence Measures				
Gender	9F / 8M	11F / 13M		
Age	11.5 ± 0.7	12.1 ± 0.6	0.54	0.011
WISC VCI	107.1 ± 3.4	97.2 ± 2.8	0.03	0.130
WISC PRI	100.5 ± 3.8	101.7 ± 3.2	0.81	0.002
Standardized Word-level and Language Measures				
TOSCRF	94.2 ± 3.0	82.6 ± 2.5	0.005	0.210
TOWRE PDE	98.5 ± 2.9	80.1 ± 2.5	< 0.001	0.401
TOWRE SWE	100.5 ± 3.1	82.6 ± 2.6	< 0.001	0.364
WJ LWID	104.2 ± 2.4	82.3 ± 2.0	< 0.001	0.591
WJ WA	102.2 ± 2.0	88.1 ± 1.7	< 0.001	0.452
WJ PC	101.3 ± 3.3	85.2 ± 2.8	< 0.001	0.289

Abbreviations: SEM = Standard Error of the Mean; WISC = Wechsler Intelligence Scale for Children; VCI = Verbal Comprehension Index; PRI = Perceptual Reasoning Index; TOSCRF = Test of Silent Contextual Reading Fluency (Form A); TOWRE = Test of Word Reading Efficiency; PDE = Phonological Decoding Efficiency; SWE = Sight Word Efficiency; WJ = Woodcock Johnson (from WRMT-R/NU); LWID = Letter Word Identification; WA = Word Attack; PC = Passage Comprehension.
η_p^2 is the partial eta squared as a measure of effect size.

2.2.2. MRI procedures

Data Acqusition Diffusion-weighted images were acquired on a 3.0-T Philips MR scanner using a single shot echo planar imaging sequence, SENSE factor 2.5, 60- x 2.2-mm thick axial slices, field of view 212 x 212 mm^2, acquired in 96 x 96 matrices, interpolated to 256 x 256, yielding 0.828 x 0.828 x 2.2 mm^3 voxel size. Diffusion weighting was isotropically distributed along 32 directions with maximum b-value of 700

s/mm^2. A structural scan was acquired for each participant using a magnetization-prepared rapid acquisition gradient-echo (MPRAGE) pulse sequence (TR/TE = 8.0/3.7 ms, flip angle = 8^o, SENSE factor = 2, voxel size 1 x 1 x 1 mm^3).

Data Processing The MR data were processed using Freesurfer and FSL. The T1-weighted images were used to perform brain parcellations using Freesurfer (Fischl et al., 2002; Fischl et al., 2004). On each side of the brain, the cortex was segmented into 34 non-overlapping regions (Desikan et al., 2006). The non-diffusion-weighted images were registered to T1-weighted images by 12 degrees of freedom affine registration in FSL (Jenkinson et al., 2002; Jenkinson and Smith, 2001), and then the transformation was inverted and applied to the parcellated T1-weighted images. Head motion and eddy current artifacts were corrected by linearly registering diffusion-weighted images to the non-diffusion-weighted image. The imaging data and each step of processing were visually checked to ensure the absence of motion artifact or parcellation/registration failure. Probabilistic fiber tracking was performed from each of the five spherical ROIs to the remaining cortex, comprised of 68 parcels. Briefly, the five ROIs were designed to cover the putative VWFA in the left fusiform gyrus, each had a radius of 6 mm, and were located along an anterior-posterior axes (Brem et al., 2009) (Fig. 2.1). The MNI coordinates of ROI centers were: ROI1 (-42, -80, -14), ROI2 (-42, -68, -16), ROI3 (-42, -

54, -17), ROI4 (-42, -42, -18), and ROI5 (-42, -30, -20). Specifically, ROI3 represented the putative VWFA as described previously (Cohen et al., 2000). 10,000 samples were initiated for probabilistic fiber tracking in each seed voxel, and the CSF region was excluded for streamlines to pass through. For each of the five ROIs, the number of streamlines found by the fiber tracking algorithm to connect to the 68 target cortical parcels was calculated.

2.2.3. Connectivity pattern analysis

Distance Matrix and Permutation Test The distance-based permutation test, a non-parametric multivariate analysis for group difference detection (Reiss et al., 2010), was performed. The test started by measuring the similarity between each pair of participants. Similarity was represented by the linear correlation coefficient $r_{ij} = corr(c_i, c_j), 1 \leq i, j \leq N, i \neq j$, where c_i, an $1 \times n_{parc}$ vector, where n_{parc} was the total number of cortical parcels, was the connectivity profile for the i^{th} subject, and N was the total number of subjects in all groups. An $N \times N$ lower triangular matrix of distance D was created, where each element, $d_{i,j} = 1 - r_{ij}$, represents the dissimilarity or distance between subjects, ranging from 0 for being coherently varying, to 2 for being negatively coherent, and 1 represents being purely unrelated. A *pseudo-F* statistic was

computed to estimate how well group membership explains the distances between participants (Shehzad et al., 2011). Then the group membership was shuffled 15,000 times to build up a permutation distribution. Significance level p was calculated as the percentage of random permutations which yielded a *pseudo-F* statistic greater than the real group membership did. A critical value of $p = 0.05$ was used to determine statistical significance.

Pattern Difference Identification First, the connectivity profiles were normalized by the total fiber counts, so that for each subject, the percentages of fiber counts originating from one particular ROI connecting to all cortical parcels sum up to 100%. Principal component analysis (PCA) was then performed on the total connectivity profile C, an $N \times n_{parc}$ matrix, and the minimum number of components accounting for >90% of total variance in the dataset, n_{PC}, was determined. The scores corresponding to these components, X, in an $N \times n_{PC}$ matrix, were used as predictor variables, and group membership, Y, in an $N \times 1$ vector, as response matrix, i.e., $Y_i = 1$, for $1 \leq i \leq N_{TD}$; $Y_i = 0$, for $N_{TD} + 1 \leq i \leq N$, $N = N_{TD} + N_{RD}$, where N_{TD} and N_{RD} were the number of participants in TD group and RD group, respectively. The linear regression coefficients β_{PC}, an n_{PC}-dimensional vector, was a linear combination of n_{PC} principal components that best differentiate between groups, which was then translated to a connectivity profile

space, or $\beta = PC * \beta_{PC}$, where β was an $n_{PC} \times 1$ vector, and PC was a $N \times n_{PC}$ matrix comprised of the first n_{comp} principal components. Additionally, a 2-tailed two sample T-test on $\hat{Y}$ was performed, where $\hat{Y} = Y + residuals$.

2.3. Results

2.3.1. Comparison across five ROIs

To estimate similarity between ROIs across participants, a distance matrix was computed, in which TD and RD groups were combined (Fig. 2.3). Hot color represents greater between-subject distance, and cold color represents higher degree of similarity. To investigate whether differences in connectivity patterns existed between the five ROIs, a pair-wise contrast permutation test was performed. Results from this analysis showed that statistically significant differences existed between many of the ROIs, except between ROI3 and ROI4 (Table 2.2).

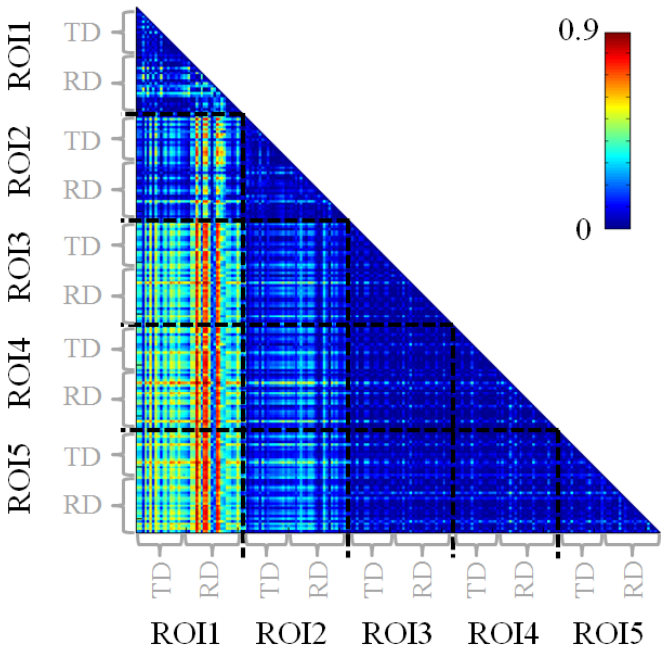

Figure 2.3. Distance matrix across subjects and ROIs. Subjects of TD and RD groups were combined to compute the distance matrix across the five ROIs. The pairwise correlation coefficient was computed to estimate similarity in the connectivity profile between participants or between ROIs. Distance, or dissimilarity, was calculated as one minus similarity, which ranges from 0 for being coherently varying to 2 for being negatively coherent, and 1 represents being purely unrelated. The triangular subdivisions noted by the dashed lines near the diagonal border reflected how individuals' connectivity profiles for the same ROI were different from each other, and the square subdivisions reflected how individuals' connectivity profiles of one particular ROI was different from all participants' connectivity profiles of another ROI.

Table 2. 2. Distance-based permutation test between ROIs

Pairwise *pseudo-F* / Pairwise *p* value	ROI1	ROI2	ROI3	ROI4	ROI5
ROI1		24.6	59.1	63.6	58.3
ROI2	<0.001		24.7	32.2	30.7
ROI3	<0.001	<0.001		1.7	4.8
ROI4	<0.001	<0.001	0.11		2.9
ROI5	<0.001	<0.001	<0.001	0.009	

A total of 15,000 permutations were computed, and *p* was calculated as the percentage of random permutations which yielded a *pseudo-F* statistic greater than the real group membership did. The pair-wise *pseudo-F* statistics are listed in the upper triangular portion of the table, and the *p* values are listed in the lower triangular portion.

To further explore the factor(s) driving these differences, a pairwise comparison was calculated in which ROI locations were linearly regressed on each ROI's connectivity profile. Findings demonstrated that occipital connections progressively decreased along an anterior to posterior gradient. From ROI1 to ROI3, the ratio of connections to inferior temporal and fusiform was found to increase; from ROI3 to ROI5, ratio of connections to fusiform started to decrease, and a higher portion of connections to medial areas was found, such as para-hippocampus and entorhinal regions (Fig. 2.4, Table 2.3). No significant difference was found between ROI4 and ROI3; therefore, ROI4 was not included in this comparison.

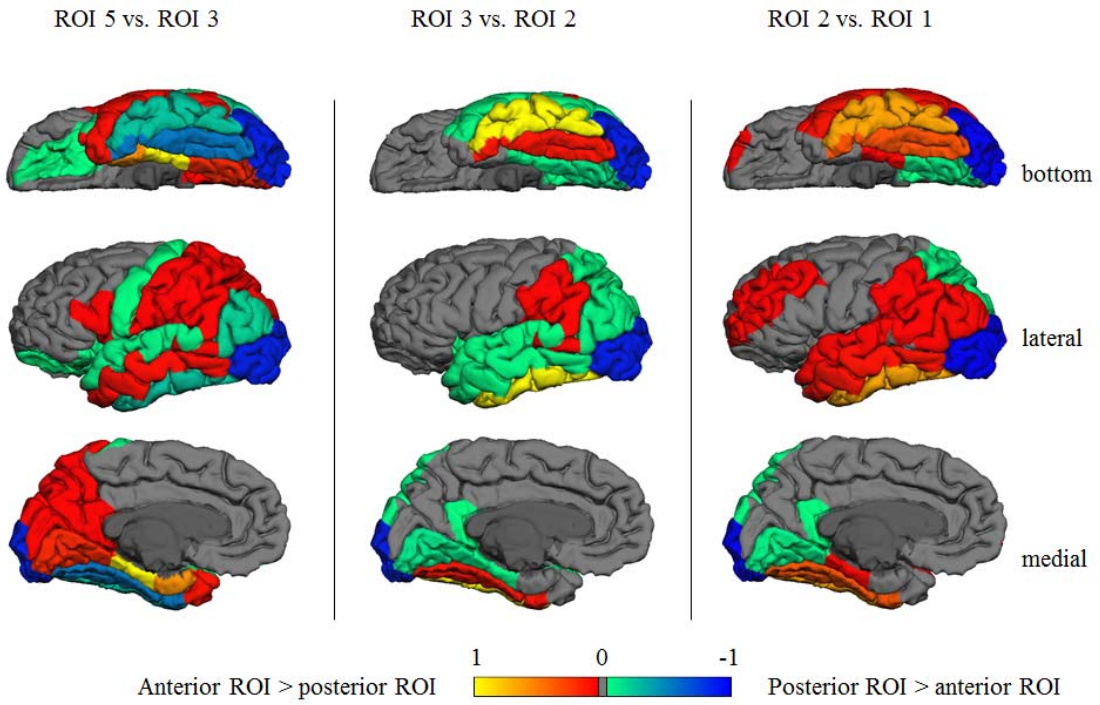

Figure 2. 4. Cortical contributions to connectivity pattern difference between consecutive ROIs. A linear regression of ROI membership (1 for anterior, 0 for posterior) onto connectivity profiles was performed, and regression coefficients, β, are displayed in color to show contributions from each cortical parcel that best described the contrast, i.e., hot colors represent cortical parcels that had a higher connection ratio to the anterior ROI than the posterior one, and vice versa. To better reveal the color distribution, β shown here was rescaled to a range of -1 to 1.

Table 2. 3. Cortical contributions to differentiating between consecutive ROIs

Cortical parcels	coefficient	Cortical parcels	coefficient
ROI2 > ROI1		ROI1 > ROI2	
L inferiortemporal	0.9753	L lateraloccipital	-1.5124
L fusiform	0.4803	L lingual	-0.0706
L middletemporal	0.0833	L superiorparietal	-0.0088
L inferiorparietal	0.0306	L isthmuscingulate	-0.0025
L superiortemporal	0.0090		
L supramarginal	0.0066		
L parahippocampal	0.0043		
L rostralmiddlefrontal	0.0026		
L cuneus	0.0020		
R precuneus	0.0014		
L postcentral	0.0013		
ROI3 > ROI2		ROI2 > ROI3	
L inferiortemporal	2.0295	L lateraloccipital	-1.8226
L fusiform	0.1384	L lingual	-0.1576
L supramarginal	0.0053	L inferiorparietal	-0.0694
L bankssts	0.0033	L parahippocampal	-0.0433
		L middletemporal	-0.0369
		L superiorparietal	-0.0136
		L superiortemporal	-0.0120
		L isthmuscingulate	-0.0047
		L insula	-0.0035
		R superiorparietal	-0.0027
		R isthmuscingulate	-0.0019
		R lateraloccipital	-0.0017
		R precuneus	-0.0017
		L pericalcarine	-0.0014
ROI5 > ROI3		ROI3 > ROI5	
L parahippocampal	4.4607	L lateraloccipital	-3.9450
L entorhinal	2.5366	L fusiform	-2.3820
L lingual	0.6277	L inferiortemporal	-1.0386
L temporalpole	0.2485	L inferiorparietal	-0.7419
L pericalcarine	0.1901	L superiortemporal	-0.1779

L middletemporal	0.1828	L insula	-0.1042
L bankssts	0.0863	L lateralorbitofrontal	-0.0126
L cuneus	0.0156	R superiorparietal	-0.0045
L superiorparietal	0.0128	L precentral	-0.0029
R lingual	0.0114	L transversetemporal	-0.0020
L precuneus	0.0093		
L supramarginal	0.0070		
L isthmuscingulate	0.0054		
R precuneus	0.0052		
R isthmuscingulate	0.0040		
L parsopercularis	0.0037		
L postcentral	0.0027		
L parstriangularis	0.0018		
L frontalpole	0.0016		
L parsorbitalis	0.0014		

Positive predictors are listed on the left, and negative predictors were on the right.

2.3.2. Group differences in connectivity patterns

For each ROI, we performed a distance-based permutation test to explore whether the VWFA connectivity pattern differed between TD (N = 17) compared to RD groups (N = 24, see Table 2.4 for demographic and behavioral data). Statistically significant differences were found between groups in ROI3 (Table 2.5), the putative center of the VWFA, (*pseudo-F*[1,39] = 1.167, and $p = 0.027$) and ROI2, (*pseudo-F*[1,39] = 1.153, and $p = 0.028$). We performed two sample t tests contrasting the group connectivity profiles within ROI2 and ROI3. Results showed greater between-group than within-group distances (ROI2: $t = -1.434$, $p = 0.152$; ROI3: $t = -2.381$, $p = 0.0175$),

indicating that the connectivity profile of a particular TD subject was more similar to the profile of other TD participants than RD participants. These findings suggest differentiation between the TD and RD groups with regards to their respective connectivity profile features.

Table 2. 4. Permutation test for connectivity pattern

	pseudo-F[a]	*p(pr > pseudo-F)*[b]
ROI1	1.01	0.323
ROI2*	1.15	0.028
ROI3*	1.17	0.027
ROI4	0.96	0.834
ROI5	0.96	0.740

a. Similar to a standard F statistic, a greater *pseudo-F* value represents greater between group variance, see method session for more details.
b. A total number of 15,000 permutations were computed, and *p* was calculated as percentage (*pr*) of random permutations which yielded a *pseudo-F* statistic greater than the real group membership did.
* $p < 0.05$.

2.3.3. Characterization of the group differences in connectivity patterns

A multiple linear regression of group membership on connectivity profiles was computed to identify the feature of the connectivity pattern that best differentiate groups (Figure 2.5 and Table 2.5). In ROI3, the VWFA, the RD group compared to the TD group had weaker connections to left fusiform gyrus and more connections to left lateral

occipital cortex. In ROI2, RD group had fewer connections to both left fusiform gyrus and left inferior temporal gyrus, and more connections to left lateral occipital cortex. The outcome of the regression model showed significant group difference in ROI2 ($t = 2.97$, $p = 0.005$) and ROI3 ($t = 2.59$, $p = 0.014$). The same approach could not replicate significant group difference for other ROIs, which was consistent with the results of the non-parametric permutation test.

Table 2. 5. The connectivity pattern characteristic of group difference

Cortical parcels	coefficient	Cortical parcels	coefficient
ROI2			
TD > RD		RD > TD	
L fusiform	0.9524	L lateraloccipital	-1.2782
L inferiortemporal	0.5261	L lingual	-0.0789
L supramarginal	0.0034	L inferiorparietal	-0.0547
L insula	0.0025	L parahippocampal	-0.0410
L rostralmiddlefrontal	0.0019	L middletemporal	-0.0209
L lateralorbitofrontal	0.0017	L superiorparietal	-0.0065
L postcentral	0.0013	L isthmuscingulate	-0.0033
		R superiorparietal	-0.0024
		L pericalcarine	-0.0017
		R lateraloccipital	-0.0017
		R isthmuscingulate	-0.0014
ROI3			
TD > RD		RD > TD	
L fusiform	1.5761	L lateraloccipital	-0.9997
L parahippocampal	0.0475	L middletemporal	-0.3221
L entorhinal	0.0243	L inferiortemporal	-0.1631
L insula	0.0030	L inferiorparietal	-0.1030
L cuneus	0.0023	L superiortemporal	-0.0331
L medialorbitofrontal	0.0016	L lingual	-0.0168
L lateralorbitofrontal	0.0014	L superiorparietal	-0.0085
L temporalpole	0.0012	L supramarginal	-0.0050
		L postcentral	-0.0031
		L pericalcarine	-0.0021

Predictors positively contributing to TD group were listed on the left.

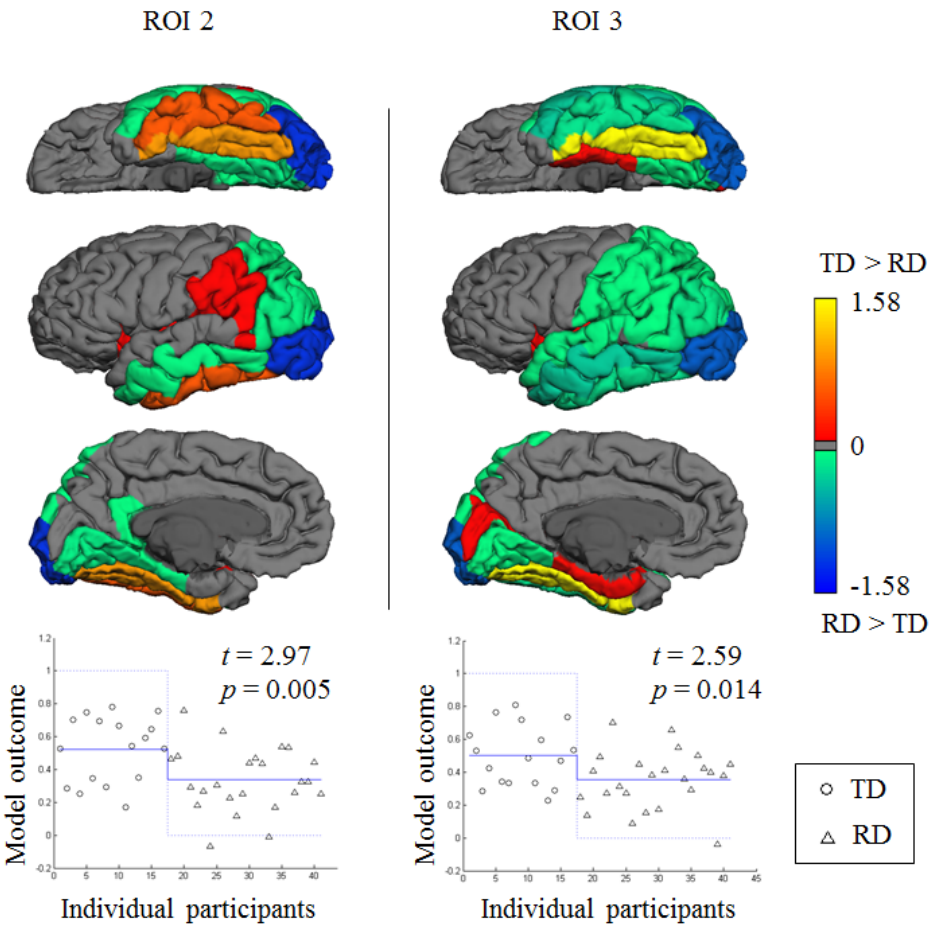

Figure 2. 5. Cortical contributions to the pattern feature and outcome of the model. A linear regression of ROI membership (1 for TD, 0 for RD) onto connectivity profiles was performed, and regression coefficients, β, were displayed in colors to show contributions from each cortical parcel that best described the group difference, i.e., cortical parcels that had a higher connection ratio in TD than RD were labeled with hot colors, and vice versa. A two-tailed T-test was performed on the model outcomes, which showed significant difference between groups. The same approach was also performed on other ROIs, but could not tell group difference significantly.

2.4. Discussion and conclusion

The current study examined the VWF-system structural connectivity patterns in children ranging in reading ability. Across all children, we found evidence that is

consistent with fMRI VWFA findings. Specifically, we demonstrated that progressing along a posterior to anterior gradient, the connectivity pattern varied significantly, namely that decreasing connectivity to visual areas (lateral occipital lobe) was observed moving from the posterior to anterior ROIs; in contrast, increasing connectivity to classic word recognition areas (e.g., fusiform and supramarginal gyri) was observed moving from posterior to anterior ROIs. Furthermore, when group differences were examined, we found evidence of a relationship between structural connectivity patterns related to the children's reading ability. In particular, results showed that in the central VWFA ROIs, differences in connectivity patterns were revealed, such that TD showed more connectivity to fusiform regions, whereas RD had more connections to visual areas.

The five ROIs utilized in this study included the VWFA and adjacent regions of the VWF-system, where a posterior-anterior progression of increased specialized response to print has been found in children (Brem et al., 2009; van der Mark et al., 2009) and in adolescents and adults (Brem et al., 2006; Brem et al., 2009; Vinckier et al., 2007). Previous studies have demonstrated that more anterior regions in the VWF-system are engaged in increasingly multimodal and semantic computations, whereas posterior regions are more responsible for perception of the visual aspect of print, including false-fonts (Cohen et al., 2004; Cohen et al., 2002). Because these seed ROIs used in the

current study have been shown by fMRI to have distinct functions, which therefore presumably would be linked to distinct cortical areas, we hypothesized that networks comprising these sub-systems, i.e., white matter connectivity patterns, would be differentiable from each other. Consistent with our expectations, from ROI1 (the most posterior ROI) to ROI3 (the putative VWFA), we found that the connectivity pattern in the consecutive ROIs progressively changed from heavily connected to visual cortex to favoring regions responsible for VWF recognition in the left inferior-temporal region (McCandliss et al., 2003). A somewhat unexpected finding was that towards the anterior tip of the VWF-system, ROI5 (the most anterior ROI) differed from ROI3 by favoring entorhinal and parahippocampal regions instead of the fusiform gyrus. Entorhinal cortex and parahippocampal areas are an important part of neural circuitry for establishing long-term memory and are related to recognition memory, particularly automated recognition memory (Murray and Richmond, 2001; Squire and Zola-Morgan, 1991). Therefore, the finding of a higher connection ratio to these regions in the anterior portion of the VWF-system may reflect the mechanism readers use for rapid memory-based retrieval of word meaning. Indeed, fMRI findings show that activation anteriorly in the VWF-system is correlated with reading speed, regardless of age (Brem et al., 2006).

Fluent reading requires efficient and well-tuned left hemisphere circuitry, and

therefore difficulties with reading have long been hypothesized to be reflective of inefficiencies in cortical connections; such suppositions date as far back as the initial studies of pure alexia, the original "disconnection syndrome" (Charcot, 1890; Dejerine, 1892; Kussmaul, 1877). In the first study examining the anatomical connections of VWFA, Epelbaum and colleagues (Epelbaum et al., 2008) used DT-tractography to map connectivity of the VWFA in an adult epilepsy patient before and after surgery. Before surgery, the patient was a proficient reader, and DT-tractography showed that the VWFA (identified by fMRI) was linked to the occipital lobe and to supramarginal gyrus through the inferior longitudinal (ILF) and arcuate fasciculi (AF), respectively. During surgery a small part of the VWFA was removed. Post-surgery, preservation of the AF was observed, but degeneration of the ILF was revealed; in conjunction with these findings, pure alexia with letter-by-letter reading developed in the patient. This case study provided sound evidence that the connection between VWFA and occipital cortex plays a key role in visual word form conversion, and that disruption to connections can result in reading difficulty. Consistent with the long- standing hypotheses regarding inefficient connectivity being related to reading difficulty, our results showed that differences between TD and RD in structural connectivity patterns were found in regions crucial for visual spatial processing (Kanwisher and Wojciulik, 2000) (ROI2) and relay of visual

stimuli to specific linguistic networks (van der Mark et al., 2011) (ROI3). More specifically, in the ROIs central to the VWFA (ROI2 and ROI3), feature cortical connectivity patterns yielded group differences in lateral occipital gyrus, left fusiform and inferior temporal gyrus. For both ROI2 and ROI3, the lateral occipital cortex connectivity was found to be a negative predictor for reading ability, which was coupled with left fusiform as a positive predictor, i.e., in TD, VWFA had a stronger tendency to connect to local fusiform gyrus, while in RD, a larger portion of white matter tracts were dedicated for communication with brain regions that support visual perception. In contrast to ROI2 and ROI3, no differences were found in the VWFA ROI thought to be mainly responsible for lower level processing (ROI1), or for those that have been found to be responsible for modality independent lexical-semantic processing (ROI4 and ROI5, Lau et al., 2008; Vigneau et al., 2006).

Overall, our results showed that the VWF-system for both RD and TD were comprised of connectivity to regions important for visual word form recognition, for example, occipital cortex and fusiform gyrus. Nevertheless, the relative load on cortical regions for children with RD was different from TD, with RD showing greater preferential connectivity to more basic visual processing areas, while TD showed preferential connectivity to areas that putatively play a role in integrating meaning and

form, i.e., the left fusiform gyrus, which is thought to relate visual stimuli to the linguistic specific network (van der Mark et al., 2011). A higher connection ratio of occipital cortex in RD could be interpreted as reflecting deficient connections to critical regions involved in distinguishing verbal from non-verbal forms, which thus give rise to difficulty with reading, and is therefore indicative of a relatively lower dedication in RD of connections supporting the processing of word forms. Nevertheless, it is important to mention that while differences were found between TD and RD, these differences are relative differences, reflecting preferential connectivity patterns; overall, across both groups, connections were evident in fusiform regions, suggesting that while the circuitry in RD may be different, it may not be wholly disrupted. Indeed, it has been suggested that the linguistic system in RD is poorly tuned, but not completely disrupted (Pugh et al., 2008).

In closing, in previous eras, there could only be speculation of the existence of a visual word-form system either in ventral occipital temporal cortex (Kinsbourne and Warrington, 1963) or in temporal parietal cortex (Warrington and Shallice, 1980) because of the limited neurobiological techniques available. With the advent of fMRI and DTI, modern techniques are now precise enough to predict brain functions with structural information alone (Saygin et al., 2012) and numerous fMRI studies have reliably found that the left ventral occipitotemporal/fusiform region is selectively responsive of written

strings relative to other categories. Among the pioneers initiating the investigation of the VWFA using fMRI (Cohen et al., 2000), Dehaene and Cohen recently asked (Dehaene and Cohen, 2011): “what are the precise connections of the VWFA? Can its connectivity pattern explain its specific role in written word recognition?” The findings of the current study contribute towards answering these questions, and provide a foundation for further explorations of connectivity patterns in the VWFA, especially patterns that may be less than optimal in RD.

REFERENCES

1. Barton, J.J., Press, D.Z., Keenan, J.P., O'Connor, M., 2002. Lesions of the fusiform face area impair perception of facial configuration in prosopagnosia. Neurology 58, 71-78.

2. Behrens, T.E., Johansen-Berg, H., Woolrich, M.W., Smith, S.M., Wheeler-Kingshott, C.A., Boulby, P.A., Barker, G.J., Sillery, E.L., Sheehan, K., Ciccarelli, O., Thompson, A.J., Brady, J.M., Matthews, P.M., 2003a. Non-invasive mapping of connections between human thalamus and cortex using diffusion imaging. Nat Neurosci 6, 750-757.

3. Behrens, T.E., Woolrich, M.W., Jenkinson, M., Johansen-Berg, H., Nunes, R.G., Clare, S., Matthews, P.M., Brady, J.M., Smith, S.M., 2003b. Characterization and propagation of uncertainty in diffusion-weighted MR imaging. Magn Reson Med 50, 1077-1088.

4. Braet, W., Wagemans, J., Op de Beeck, H.P., 2012. The visual word form area is organized according to orthography. Neuroimage 59, 2751-2759.

5. Brem, S., Bach, S., Kucian, K., Guttorm, T.K., Martin, E., Lyytinen, H., Brandeis, D., Richardson, U., 2010. Brain sensitivity to print emerges when children learn letter-speech sound correspondences. Proc Natl Acad Sci U S A 107, 7939-7944.

6. Brem, S., Bucher, K., Halder, P., Summers, P., Dietrich, T., Martin, E., Brandeis, D., 2006. Evidence for developmental changes in the visual word processing network beyond adolescence. Neuroimage 29, 822-837.

7. Brem, S., Halder, P., Bucher, K., Summers, P., Martin, E., Brandeis, D., 2009. Tuning of the visual word processing system: distinct developmental ERP and fMRI effects. Hum Brain Mapp 30, 1833-1844.

8. Cohen, L., Dehaene, S., Naccache, L., Lehéricy, S., Dehaene-Lambertz, G., Hénaff, M.A., Michel, F., 2000. The visual word form area: spatial and temporal characterization of an initial stage of reading in normal subjects and posterior split-brain patients. Brain 123 (Pt 2), 291-307.

9. Cohen, L., Jobert, A., Le Bihan, D., Dehaene, S., 2004. Distinct unimodal and multimodal regions for word processing in the left temporal cortex. Neuroimage 23, 1256-1270.

10. Cohen, L., Lehéricy, S., Chochon, F., Lemer, C., Rivaud, S., Dehaene, S., 2002. Language-specific tuning of visual cortex? Functional properties of the Visual Word Form Area. Brain 125, 1054-1069.

11. Dehaene, S., Cohen, L., 2011. The unique role of the visual word form area in reading. Trends Cogn Sci 15, 254-262.

12. Epelbaum, S., Pinel, P., Gaillard, R., Delmaire, C., Perrin, M., Dupont, S., Dehaene, S., Cohen, L., 2008. Pure alexia as a disconnection syndrome: new diffusion imaging evidence for an old concept. Cortex 44, 962-974.

13. Fletcher, J.M., Francis, D.J., Shaywitz, S.E., Lyon, G.R., Foorman, B.R., Stuebing, K.K., Shaywitz, B.A., 1998. Intelligent testing and the discrepancy model for children with learning disabilities. Learning Disabilities Research & Practice 13, 186-203.

14. Johansen-Berg, H., Behrens, T.E., Sillery, E., Ciccarelli, O., Thompson, A.J., Smith, S.M., Matthews, P.M., 2005. Functional-anatomical validation and individual variation of diffusion tractography-based segmentation of the human thalamus. Cereb Cortex 15, 31-39.

15. Kanwisher, N., McDermott, J., Chun, M.M., 1997. The fusiform face area: a module in human extrastriate cortex specialized for face perception. J Neurosci 17, 4302-4311.

16. Kanwisher, N., Wojciulik, E., 2000. Visual attention: insights from brain imaging. Nat Rev Neurosci 1, 91-100.

17. Kinsbourne, M., warrington, E.K., 1963. The localizing significance of limited simultaneous visual form perception. Brain 86, 697-702.

18. Lau, E.F., Phillips, C., Poeppel, D., 2008. A cortical network for semantics: (de)constructing the N400. Nat Rev Neurosci 9, 920-933.

19. Lyon, G.R., 1995. Toward a definition of dyslexia. Annals of Dyslexia 45, 3-27.

20. Mandonnet, E., Gatignol, P., Duffau, H., 2009. Evidence for an occipito-temporal tract underlying visual recognition in picture naming. Clin Neurol Neurosurg 111, 601-605.

21. Marenco, S., Stein, J.L., Savostyanova, A.A., Sambataro, F., Tan, H.Y., Goldman, A.L., Verchinski, B.A., Barnett, A.S., Dickinson, D., Apud, J.A., Callicott, J.H., Meyer-Lindenberg, A., Weinberger, D.R., 2012. Investigation of anatomical thalamo-cortical connectivity and FMRI activation in schizophrenia. Neuropsychopharmacology 37, 499-507.

22. McCandliss, B.D., Cohen, L., Dehaene, S., 2003. The visual word form area: expertise for reading in the fusiform gyrus. Trends Cogn Sci 7, 293-299.

23. Menke, R.A., Jbabdi, S., Miller, K.L., Matthews, P.M., Zarei, M., 2010. Connectivity-based segmentation of the substantia Nigra in human and its implications in Parkinson's disease. Neuroimage.

24. Murray, E.A., Richmond, B.J., 2001. Role of perirhinal cortex in object perception, memory, and associations. Curr Opin Neurobiol 11, 188-193.

25. Nestor, A., Behrmann, M., Plaut, D.C., 2012. The Neural Basis of Visual Word Form Processing: A Multivariate Investigation. Cereb Cortex.

26. Petersen, S.E., Fox, P.T., Posner, M.I., Mintun, M., Raichle, M.E., 1988. Positron emission tomographic studies of the cortical anatomy of single-word processing. Nature 331, 585-589.

27. Petersen, S.E., Fox, P.T., Snyder, A.Z., Raichle, M.E., 1990. Activation of extrastriate and frontal cortical areas by visual words and word-like stimuli. Science 249, 1041-1044.

28. Pitcher, D., Walsh, V., Yovel, G., Duchaine, B., 2007. TMS evidence for the involvement of the right occipital face area in early face processing. Curr Biol 17, 1568-1573.

29. Price, C.J., Devlin, J.T., 2011. The interactive account of ventral occipitotemporal contributions to reading. Trends Cogn Sci 15, 246-253.

30. Price, C.J., Wise, R.J., Frackowiak, R.S., 1996. Demonstrating the implicit processing of visually presented words and pseudowords. Cereb Cortex 6, 62-70.

31. Pugh, K.R., Frost, S.J., Sandak, R., Landi, N., Rueckl, J.G., Constable, R.T., Seidenberg, M.S., Fulbright, R.K., Katz, L., Mencl, W.E., 2008. Effects of stimulus difficulty and repetition on printed word identification: an fMRI comparison of nonimpaired and reading-disabled adolescent cohorts. J Cogn Neurosci 20, 1146-1160.

32. Pugh, K.R., Mencl, W.E., Jenner, A.R., Katz, L., Frost, S.J., Lee, J.R., Shaywitz, S.E., Shaywitz, B.A., 2000. Functional neuroimaging studies of reading and reading disability (developmental dyslexia). Ment Retard Dev Disabil Res Rev 6, 207-213.

33. Rauschecker, A.M., Bowen, R.F., Parvizi, J., Wandell, B.A., 2012. Position

sensitivity in the visual word form area. Proc Natl Acad Sci U S A 109, E1568-1577.

34. Rauschecker, A.M., Bowen, R.F., Perry, L.M., Kevan, A.M., Dougherty, R.F., Wandell, B.A., 2011. Visual feature-tolerance in the reading network. Neuron 71, 941-953.

35. Reiss, P.T., Stevens, M.H., Shehzad, Z., Petkova, E., Milham, M.P., 2010. On distance-based permutation tests for between-group comparisons. Biometrics 66, 636-643.

36. Saygin, Z.M., Osher, D.E., Koldewyn, K., Reynolds, G., Gabrieli, J.D., Saxe, R.R., 2012. Anatomical connectivity patterns predict face selectivity in the fusiform gyrus. Nat Neurosci 15, 321-327.

37. Schlaggar, B.L., McCandliss, B.D., 2007. Development of neural systems for reading. Annu Rev Neurosci 30, 475-503.

38. Shaywitz, S.E., 1998. Dyslexia. N Engl J Med 338, 307-312.

39. Shehzad, Z., Reiss, P.T., Adelstein, J., Emerson, J.W., Chabernaud, C., Mennes, M., DiMartino, A., McMahon, K., Copland, D., Castellanos, F.X., Kelly, C., Milham, M.P., 2011. Connectome-Wide Association Studies (CWAS): A Multivariate Distance-Based Approach. Proc. Organization for Hum. Brain Mapp., Quebec City, Canada.

40. Squire, L.R., Zola-Morgan, S., 1991. The medial temporal lobe memory system. Science 253, 1380-1386.

41. van der Mark, S., Bucher, K., Maurer, U., Schulz, E., Brem, S., Buckelmüller, J., Kronbichler, M., Loenneker, T., Klaver, P., Martin, E., Brandeis, D., 2009. Children with dyslexia lack multiple specializations along the visual word-form (VWF) system. Neuroimage 47, 1940-1949.

42. van der Mark, S., Klaver, P., Bucher, K., Maurer, U., Schulz, E., Brem, S., Martin, E., Brandeis, D., 2011. The left occipitotemporal system in reading: disruption of

focal fMRI connectivity to left inferior frontal and inferior parietal language areas in children with dyslexia. Neuroimage 54, 2426-2436.

43. Vigneau, M., Beaucousin, V., Hervé, P.Y., Duffau, H., Crivello, F., Houdé, O., Mazoyer, B., Tzourio-Mazoyer, N., 2006. Meta-analyzing left hemisphere language areas: phonology, semantics, and sentence processing. Neuroimage 30, 1414-1432.

44. Vinckier, F., Dehaene, S., Jobert, A., Dubus, J.P., Sigman, M., Cohen, L., 2007. Hierarchical coding of letter strings in the ventral stream: dissecting the inner organization of the visual word-form system. Neuron 55, 143-156.

45. Wandell, B.A., Rauschecker, A.M., Yeatman, J.D., 2012. Learning to see words. Annu Rev Psychol 63, 31-53.

46. Warrington, E.K., Shallice, T., 1980. Word-form dyslexia. Brain 103, 99-112.

47. Yeatman, J.D., Rauschecker, A.M., Wandell, B.A., 2012. Anatomy of the visual word form area: Adjacent cortical circuits and long-range white matter connections. Brain Lang.

48. Zarei, M., Patenaude, B., Damoiseaux, J., Morgese, C., Smith, S., Matthews, P.M., Barkhof, F., Rombouts, S.A., Sanz-Arigita, E., Jenkinson, M., 2010. Combining shape and connectivity analysis: an MRI study of thalamic degeneration in Alzheimer's disease. Neuroimage 49, 1-8.

CHAPTER III

THALAMOCORTICAL CONNECTIVITY: WHAT CAN DIFFUSION TRACTOGRAPHY TELL US ABOUT READING DIFFICULTIES IN CHILDREN?

3.1. Introduction

Dyslexia is a developmental reading disorder that affects a significant number (5-17%) of individuals, and is characterized by deficits in phonological processing which consequently impede the development of adequate word recognition/decoding. These deficits are specific, and are present despite adequate instruction and intelligence (Lyon, 1995; Shaywitz, 1998). While the behavioral characteristics of dyslexia are fairly well known, the neurobiological characteristics of this disorder are still under examination. However, with the advent of neuroimaging, especially functional MRI (fMRI), over the last two decades, studies have mapped the areas in the brain that are associated with good and poor reading. Converging findings reveal that proficient reading performance is associated with a coordinated left hemisphere network that involves temporo-parietal, occipitotemporal, inferior frontal and anterior perisylvian regions, including sensorimotor, premotor, pars opercularis and triangularis (Broca's) areas (Heilman et al., 1995).

Conversely, in those who demonstrate impaired performance (dyslexia), the homologous right hemisphere regions are recruited, with underactivation seen in particular in left fusiform gyrus (Richlan et al., 2011).

In addition to differences in functional activation, the strength of connectivity between these regions may also influence reading skill. Accurate and fluent reading requires a synthesis of information between cortical processing regions via white matter tracks connecting these regions. For this reason, in order to understand more about dyslexia, structural neuroimaging studies have been employed to map white matter microstructure through the use of Diffusion Tensor Imaging (DTI). Consistent with findings from functional imaging studies, white matter microstructural anomalies have been reported in regions such as left inferior frontal gyrus, left temporo-parietal region, left insula, and left fusiform (Davis et al., 2010; Niogi and McCandliss, 2006; Rimrodt et al., 2010). These findings suggest that the characteristics of white matter pathways between distant cortical regions are potentially an important aspect of the neurobiology of dyslexia.

While the primary focus of neuroimaging work to date in dyslexia has been on cortical regions, more recently there has been an interest in subcortical regions. In particular, previous studies have reported individual variability in functional (Díaz et al.,

2012; Fiebach et al., 2002; Hoeft et al., 2007; Preston et al., 2010; Price et al., 1994; Turkeltaub et al., 2002;) and structural (e.g., Galaburda and Eidelberg, 1982) aspects of the thalamus that relate to differences in reading skills. That there is thalamic involvement in dyslexia is not surprising because the thalamus acts as an information processing way station for the brain, relaying signals contributing to the regulation of arousal (Portas et al., 1998) and cognition (Johnson and Ojemann, 2000; Karussis et al., 2000). It is therefore logical that the cortical regions implicated in dyslexia may be due to anomalous thalamo-cortical connectivity. Nevertheless, despite the thalamus' central "relay station" role, and functional imaging studies showing thalamic anomalies in dyslexia, to date no *in vivo* study has examined whether thalamo-cortical structural connectivity is related to reading ability. This may be because it is technically complex to capture thalamo-cortical connectivity, given the small size of the white matter tracts within the thalamus. However, studies have shown that agreement exists between thalamic subdivisions identified by cytoarchitecture and those identified by diffusion tractography connectivity measures (Behrens et al., 2003a; Johansen-Berg et al., 2005). In fact, tractography defined thalamo-cortical connectivity has revealed structural alterations in a number of disorders, such as Alzheimer's disease (Zarei et al., 2010) and schizophrenia (Marenco et al., 2012), suggesting that examination of thalamo-cortical

connectivity is feasible.

In this chapter we examine the connectivity between the thalamus and cortical regions that have been implicated in dyslexia. Establishing whether white matter anomalies are present in pathways from such a critical subcortical region of the brain may shed light on subcortical-cortical interactions in dyslexia, and where anomalies may exist. Given the lack of previous studies in dyslexia examining potential connectivity differences between those with dyslexia and typically developing readers, our hypotheses were necessarily general; however, given the differences in functional activation in the thalamus between typically developing and dyslexic groups, and the cytoarchitectural findings, we expected that we would find differences in connectivity between the thalamus and cortical regions. While specificity of these regions was difficult to pinpoint, in the one previous connectivity study (Davis et al., 2010), we showed differences in thalamo-cortical connectivity between responders and non-responders to reading intervention. Therefore, we expected thalamo-cortical differences between groups in the standard language-related regions near the perisylvian cortex, such as the occipito-temporal cortex (OTC) and the temporo-parietal cortex (TPC). We also expected to find group differences in connectivity between the thalamus and areas within the anterior perisylvian region, including sensorimotor cortex. Activation in this area during word

recognition tasks (Zatorre et al. 1992) may reflect the underlying association between speech sound articulations and reading (Heilman et al., 1995).

3.2. Methods

3.2.1. Participants

A total of 50 children participated in this study, and 4 children were excluded due to imaging artifacts. All of these children are right handed, 20 were female. Before entering the study, parents of children were administered an informal screening measure over the phone to ensure that participants met the study's inclusion criteria: 1) native English speakers, 2) normal hearing and vision, 3) no history of major psychiatric illness, 4) no traumatic brain injury/epilepsy, and 5) no contraindication to MRI. Each parent gave written consent while a separate written assent was obtained from each child at the start of the study, with procedures carried out in accordance with the university's Institutional Review Board. During their visit, participants were given a comprehensive battery of psychoeducational and academic achievement measures. Each individual received the Wechsler Intelligence Scale for Children-III (WISC-III; Wechsler, 1991) to determine eligibility based upon FSIQ criteria. Eligible participants completed a battery

of standardized tests to determine reading ability (RD or TD). The battery consisted of the following standardized measures of intellectual and academic achievement: Rapid Naming subtest from the Comprehensive Test of Phonological Processing (CTOPP; Wagner et al., 1999); the Test of Silent Contextual Reading Fluency (TOSCRF-Form A; Hammill et al., 2006); Phonological Decoding Efficiency (PDE) and Sight Word Efficiency (SWE) from the Test of Word Reading Efficiency (TOWRE; Torgesen et al, 1997); Verbal Comprehension Index (VCI) and Perceptual Reasoning Index (PRI) subsets from Wechsler Intelligence Scale for Children, Fourth Edition (WISC-IV; Wechsler, 2003); Spelling and Fundamental Literacy Index (FLI) subsets from the Word Identification and Spelling Test (WIST; Wilson and Felton, 2004); and Word Attack (WA), Word Identification (Word ID), and Passage Comprehension (PC) subtests from the Woodcock Johnson –III (WJ-III; Woodcock, 2001; Woodcock et al., 2003).

Participants met criteria for RD if they had a standard score at or below the 25th percentile on the Basic Reading Composite (BR) on the WJ-III, which consists of the Word ID and WA measures. Participants met criteria to be TD by having a standard score at or above the 40th percentile on the BR. Of the eligible participants, 23 met criteria for RD and 21 met criteria for TD.

The two groups of children were not significantly different in age, gender or non-

verbal IQ. Multivariate ANOVA (MANOVA) showed their behavioral profiles related to reading and language skills were significantly different, and there were no significant difference in there behavioral profiles otherwise. See Table 3.1 for detailed demographic and behavioral profiles.

3.2.2. MRI procedures

MR Data Acquisition High resolution T1 weighted images and Diffusion Weighted (DW) images were acquired on a Philips 3T MR scanner. The T1 images had a FOV of 256 x 200 x 256 mm^3, and isotropic voxel size of 1 mm^3. The DW scan was comprised of image volumes with diffusion weighting along 32 gradient directions evenly distributed on a unit sphere, b = 700 s/mm^2. The data were initially acquired in 96 × 96 matrices with a FOV of 212 × 212 × 143 mm^3, and then interpolated into 256 x 256 matrices, yielding 0.828 × 0.828 × 2.2mm^3 voxel sizes.

Image Processing Image analysis was performed in Freesurfer and FSL. T1-weighted images were used for brain parcellation using Freesurfer. Briefly, this automated process includes motion correction, brain tissue extraction (Ségonne et al., 2004), white and grey matter segmentation (Fischl et al., 2002, 2004), intensity normalization (Sled et al, 1998), tessellation of the gray/white matter boundary,

automated topology correction (Fischl et al., 2001; Ségonne et al., 2007), and surface deformation (Dale and Sereno, 1993; Dale et al., 1999; Fischl and Dale, 2000). On each side of the brain, the cortex was segmented into 9 non-overlapping regions (Fig. 3.1) from the original Freesurfer parcellations (Desikan et al, 2006). The non-diffusion-weighted images were registered to T1-weighted images by 12 degrees of freedom affine registrations (Jenkinson and Smith, 2001; Jenkinson et al., 2002), and then the transformation was inverted and applied to the parcellated T1 images. Head motion and eddy current artifacts were corrected by linearly registering diffusion-weighted images to the non-diffusion-weighted image. The imaging data and each step of processing were visually checked to ensure the absence of motion artifact or parcellation/registration failure.

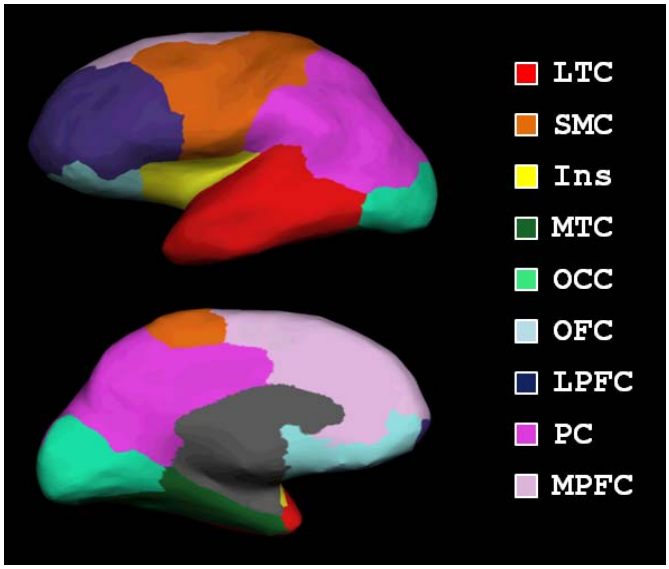

Figure 3. 1. Cortical ROIs in one TD subject. The subdivisions of the cortex used in the analysis are shown for the left hemisphere in a lateral (top) and medial (bottom) view with color labels for reference. Bilateral ROIs were used in the analysis, whereas unilateral ROIs are shown here for visualization. The cortex was segmented into nine non-overlapping regions with the original Freesurfer parcellations (Desikan et al, 2006): lateral temporal cortex (LTC: transverse temporal cortex, superior temporal gyrus, banks of the superior temporal sulcus, inferior temporal gyrus, middle temporal gyrus, temporal pole), sensorimotor cortex (SMC: precentral gyrus, caudal middle frontal gyrus, post-central gyrus, paracentral lobule), insula cortex (Ins: insula cortex), medial temporal cortex (MTC: entorhinal cortex, parahippocampal gyrus, fusiform gyrus), occipital cortex (OCC: pericalcarine cortex, lingual gyrus, lateral occipital cortex, cuneus cortex), orbitofrontal cortex (OFC: pars orbitalis, medial orbitofrontal cortex, lateral orbitofrontal cortex), lateral prefrontal cortex (LPFC: pars triangularis, frontal pole, rostral middle frontal gyrus, pars opercularis), parietal cortex (PC: inferior parietal cortex, supramarginal gyrus, precuneus cortex, posterior cingulate cortex, isthmus cingulate, superior parietal cortex), and medial prefrontal cortex (MPFC: caudal anterior cingulate, rostral anterior cingulate, superior frontal gyrus).

DTI Analysis Diffusion tensor image analysis was performed using the FDT tool (Behrens et al., 2003b). The probabilistic diffusion parameters were modeled with up to 2

fiber compartments (Behrens et al., 2007), and probabilistic tractography (ProbTrackX[1]) was performed between thalami and the segmented cortical target regions. In each thalamic voxel, 25,000 samples were drawn. Ventricles were avoided for fiber tracking. For each voxel in the thalamus, the number of samples reaching each of the target regions was counted, and the ***connection ratio*** to a specific cortical region was calculated as the ratio of the number of samples reaching this cortical region versus the total number of samples reaching any of the cortical regions.

Thalamo-cortical Connectivity For each ROI in the cortex, the thalamo-cortical connectivity was calculated as the average connection ratio in the ipsi-lateral thalamus. Thalamic voxels with zero connection densities were excluded from the connectivity calculation. The thalamo-cortical connectivity was then compared between groups. Additionally, correlations between connectivity indices and behavioral scores were examined. Considering that the connectivities of homologous structures on both sides were not completely independent measurements, repeated measures ANOVAs (R-ANOVAs) were performed between thalamo-cortical connectivity in both hemispheres and behavioral scores. Effects of age and gender on findings were also examined. Finally, it is important to note that because the connection density was calculated as the ratio of

[1] http://www.fmrib.ox.ac.uk/fsl/fdt/fdt_probtrackx.html

the number of fibers reaching one ROI versus reaching all ipsi-lateral ROIs, the relative size of an ROI could exert an impact on the calculated connectivity quantities. To control for this potential confound, the effects of relative ROI sizes were also examined in the R-ANOVA analyses. In addition, the absolute cortex and ROI volumes were also compared between groups.

3.3. Results

3.3.1. Demographic and neuropsychological data

Demographic variables were compared between groups using multivariate *ANOVA* (*MANOVA*). The two groups of children had similar characteristics in age (F[1,35] = 0.19, p = 0.67, (η_p^2 = 0.005)) and gender (Table 3.1). As expected, children with dyslexia had significantly lower reading test scores compared with TD children (Table 3.2, all p<0.001).

Table 3. 1. Demographic and neuropsychological profile of each group (mean ± SEM)

	TD	RD	*p*
Demographic and General Intelligence Measures			
Gender	10 F, 11 M	10 F, 13 M	
Age	11.9 ± 0.7	12.3 ± 0.7	0.67
WISC VCI	106.2 ± 2.9	98.7 ± 2.8	0.07
WISC PRI	101.3 ± 3.6	98.5 ± 3.5	0.58
Standardized Word-level and Language Measures			
CTOPP RaN	103.6 ± 3.3	82.1 ± 3.2	< 0.001
TOSCRF	95.9 ± 2.5	80.9 ± 2.4	< 0.001
TOWRE PDE	102.3 ± 2.6	79.5 ± 2.5	< 0.001
TOWRE SWE	102.5 ± 2.6	82.3 ± 2.5	< 0.001
TOWRE TotWRE	102.9 ± 2.9	77.0 ± 2.7	< 0.001
WIST Spell	101.8 ± 3.3	70.7 ± 3.1	< 0.001
WIST FLI	101.5 ± 3.5	66.6 ± 3.3	< 0.001
WJ LWID	105.2 ± 2.2	82.8 ± 2.1	< 0.001
WJ WA	103.9 ± 2.0	87.4 ± 1.9	< 0.001
WJ PC	100.8 ± 2.8	85.3 ± 2.7	< 0.001
WJ BRS	105.1 ± 2.0	84.7 ± 1.9	< 0.001

WISC = Wechsler Intelligence Scale for Children; VCI = Verbal Comprehension Index; PRI = Perceptual Reasoning Index; CTOPP = Comprehensive Test of Phonological Processing; RaN = Rapid Naming; TOSCRF = Test of Silent Contextual Reading Fluency (Form A); TOWRE = Test of Word Reading Efficiency; PDE = Phonological Decoding Efficiency; SWE = Sight Word Efficiency; TotWRE = Total Word Reading Efficiency; WIST = Word Identification and Spelling Test; Spell = Spelling; FLI = Fundamental Literacy Index; WJ = Woodcock Johnson; LWID = Letter Word Identification(from WRMT-R/NU); WA = Word Attack (from WRMT-R/NU); PC = Passage Comprehension (from WRMT-R/NU); BRS = Basic Reading Score (from WRMT-R/NU).

3.3.2. Volumetric data

On each side of the brain, the cortex was segmented into 9 non-overlapping regions (Fig. 3.1). The *R-ANOVA* was performed to compare the sizes of brain regions

between groups. No significant statistical difference was observed between the TD group and the RD group in total cortex volume or volumes of each ROI (Tables 3.2, 3.3). The relative size of the SMC was found to be greater in RD than TD (F[1, 41] = 4.134, p = 0.049, (η_p^2 = 0.092)) when considering left and right sides together in a repeated GLM measurement. The relative size of insula cortex on the right side was found to be greater for the TD group than the group with RD (t = 2.339, p = 0.02, (η_p^2 = 0.118)) in a repeated GLM measurement, but this category difference became insignificant when performing a regular GLM analysis on each side separately (left side: F[1, 42] = 0.61, p = 0.44, (η_p^2 = 0.014); right side: F[1, 42] = 3.8, p = 0.06, (η_p^2 = 0.083)). No significant statistical difference was observed in terms of relative ROI size for the rest of the regions. All statistics reported were calculated in SPSS and controlled for age.

Table 3. 2. Group comparison of brain region sizes (cm^3)

	Total			Left			Right		
	mean ± SEM		*p*	mean ± SEM		*p*	mean ± SEM		*p*
	TD	RD		TD	RD		TD	RD	
OFC[a]	17.2 ± 0.5	17.5 ± 0.5	0.67	17.3 ± 0.5	17.3 ± 0.5	0.94	17.2 ± 0.6	17.8 ± 0.6	0.48
MPFC	27.5 ± 0.8	27.7 ± 0.7	0.89	27.4 ± 0.8	27.5 ± 0.8	0.91	27.6 ± 0.8	27.8 ± 0.7	0.87
LPFC	27.9 ± 0.7	28.2 ± 0.7	0.80	26.8 ± 0.8	27.4 ± 0.7	0.59	29.1 ± 0.8	29.0 ± 0.7	0.96
SMC	33.6 ± 0.9	35.0 ± 0.9	0.31	33.6 ± 0.9	34.9 ± 0.9	0.28	33.7 ± 1.0	35.0 ± 0.9	0.35
PC	59.0 ± 2.0	58.6 ± 2.0	0.88	58.7 ± 2.0	58.5 ± 2.0	0.94	59.2 ± 2.0	58.7 ± 2.0	0.83
MTC	14.6 ± 0.5	14.4 ± 0.5	0.84	15.0 ± 0.5	14.7 ± 0.4	0.66	14.2 ± 0.6	14.2 ± 0.5	1.00
LTC	44.7 ± 1.0	44.1 ± 1.0	0.76	45.5 ± 1.0	44.5 ± 1.0	0.62	43.9 ± 2.0	43.6 ± 2.0	0.92
OCC	25.5 ± 0.7	25.4 ± 0.6	0.93	25.0 ± 0.6	25.2 ± 0.6	0.89	25.9 ± 0.7	25.7 ± 0.7	0.77
Ins	7.2 ± 0.2	6.9 ± 0.2	0.16	7.3 ± 0.2	7.0 ± 0.2	0.39	7.2 ± 0.2	6.7 ± 0.2	0.07
Thal[b]	7.1 ± 0.2	7.3 ± 0.1	0.47	7.1 ± 0.2	7.3 ± 0.1	0.43	7.2 ± 0.2	7.3 ± 0.1	0.52

a. The abbreviations in this and following tables are consistent with Figure 1.

b. Thal = Thalamus.

Table 3. 3. Group comparison of ROI relative sizes[a] (%)

	Total			Left			Right		
	mean ± SEM		*p*	mean ± SEM		*p*	mean ± SEM		*p*
	TD	RD		TD	RD		TD	RD	
OFC	6.7 ± 0.1	6.8 ± 0.1	0.33	6.7 ± 0.1	6.7 ± 0.1	0.88	6.6 ± 0.1	6.9 ± 0.1	0.15
MPFC	10.7 ± 0.1	10.7 ± 0.1	0.70	10.7 ± 0.2	10.7 ± 0.1	0.81	10.7 ± 0.1	10.8 ± 0.1	0.65
LPFC	10.9 ± 0.1	10.9 ± 0.1	0.67	10.4 ± 0.2	10.7 ± 0.2	0.37	11.3 ± 0.1	11.2 ± 0.1	0.80
SMC	13.1 ± 0.2	13.6 ± 0.2	0.049*	13.1 ± 0.2	13.6 ± 0.2	0.08	13.1 ± 0.2	13.6 ± 0.2	0.07
PC	22.9 ± 0.2	22.7 ± 0.2	0.49	22.9 ± 0.3	22.7 ± 0.3	0.63	22.9 ± 0.2	22.7 ± 0.2	0.41
MTC	5.7 ± 0.2	5.6 ± 0.1	0.76	5.9 ± 0.1	5.7 ± 0.1	0.54	5.5 ± 0.2	5.5 ± 0.2	0.99
LTC	17.4 ± 0.3	17.0 ± 0.3	0.38	17.7 ± 0.3	17.2 ± 0.3	0.24	17.0 ± 0.3	16.8 ± 0.3	0.65
OCC	9.9 ± 0.2	9.9 ± 0.2	0.91	9.8 ± 0.2	9.8 ± 0.2	0.88	10.1 ± 0.2	10 ± 0.2	0.71
Ins	2.8 ± 0.1	2.7 ± 0.0	0.05	2.8 ± 0.1	2.7 ± 0.0	0.25	2.8 ± 0.1	2.6 ± 0.1	0.02*
Thal	6.7 ± 0.1	6.8 ± 0.1	0.33	6.7 ± 0.1	6.7 ± 0.1	0.88	6.6 ± 0.1	6.9 ± 0.1	0.15

a. The relative size was calculated as the ratio of individual ROI size versus the total volume of the ipsi-lateral cortical regions.

* $p<0.05$

3.3.3. Thalamo-cortical connectivity

Three regions were revealed to have significant thalamo-cortical connectivity differences between groups (Table 3.4): 1) the orbital frontal cortex (OFC), 2) the insula (Ins), and 3) the sensorimotor cortex (SMC). For the left OFC, the TD group showed greater connectivity to the thalamus than RD (t = 2.245, p = 0.03, (η_p^2 = 0.109)). For the right Ins, the TD group showed greater connectivity to the thalamus than RD (t = 2.032, p = 0.049, (η_p^2 = 0.091)). Additionally, greater connectivity between left SMC and the thalamus was found in the RD group as compared to TD (t = -2.578, p = 0.014, (η_p^2 = 0.140)). On the right side, the same trend was found, although it did not reach the level of statistical significance. As a result, if left and right sides are considered together, the RD group showed significantly greater thalamo-SMC connectivity than the TD group (F[1, 41] = 7.88, p = 0.008, (η_p^2 = 0.161)).

Table 3. 4. Group comparison of thalamo-cortical connectivity[a] (%)

	Total			Left			Right		
	mean ± SEM		*p*	mean ± SEM		*p*	mean ± SEM		*p*
	TD	RD		TD	RD		TD	RD	
OFC	15.9 ± 1.9	11.2 ± 1.9	0.09	16.2 ± 1.9	10.3 ± 1.8	0.03*	15.7 ± 2.5	12.0 ± 2.4	0.30
MPFC	17.5 ± 1.3	18.2 ± 1.2	0.71	16.0 ± 1.4	16.7 ± 1.3	0.71	19.1 ± 1.7	19.7 ± 1.7	0.79
LPFC	21.9 ± 1.4	24.6 ± 1.4	0.16	20.8 ± 1.9	22.6 ± 1.9	0.50	22.9 ± 2.0	26.7 ± 1.9	0.19
SMC	17.0 ± 1.1	21.4 ± 1.1	0.01*	18.8 ± 1.6	24.7 ± 1.6	0.01*	15.2 ± 1.1	18.2 ± 1.1	0.07
PC	17.8 ± 1.3	17.7 ± 1.2	0.97	19.2 ± 1.5	17.9 ± 1.4	0.53	16.3 ± 1.5	17.4 ± 1.5	0.59
MTC	6.1 ± 0.8	6.6 ± 0.8	0.66	6.9 ± 1.0	6.8 ± 1.0	0.96	5.3 ± 0.9	6.4 ± 0.9	0.40
LTC	6.8 ± 0.9	7.9 ± 0.9	0.42	6.6 ± 1.0	7.2 ± 0.9	0.69	7.1 ± 1.5	8.6 ± 1.4	0.45
OCC	3.9 ± 0.6	3.7 ± 0.6	0.89	4.6 ± 0.8	4.4 ± 0.8	0.88	3.1 ± 0.6	3.1 ± 0.6	0.95
Ins	4.2 ± 0.7	3.2 ± 0.6	0.26	3.2 ± 0.8	3.7 ± 0.7	0.64	5.3 ± 0.9	2.6 ± 0.9	0.049*

a. For each voxel in the thalamus, the number of samples reaching each target region was counted, and the ***connection density*** to a specific cortical region is calculated as the ratio of the number of samples reaching this cortical region versus the total number of samples reaching any of the cortical regions. For each ROI in the cortex, the ***thalamo-cortical connectivity*** was calculated as the average ***connection density*** in the ipsi-lateral thalamus.

* $p<0.05$

Since the precentral and postcentral cortices in the sensorimotor territory have distinct brain functions, the statistics, including group comparison and correlation analyses, were also performed on thalamic connectivity with precentral and postcenteral cortices separately. The results showed a great commonality between pre- and post-central cortices, and were largely consistent with the results of sensorimotor cortex.

In summary, no group difference was found for brain volume or absolute ROI sizes. The relative ROI size for SMC was greater in RD than TD in a repeated GLM measurement when considering left and right sides together. The relative size of insula cortex on the right side was found to be greater for the TD group than the group with RD in a repeated GLM measurement, but this difference became insignificant when performing a GLM analysis on each side separately. The thalamo-insula connectivity on the right side was found to be greater in the TD group, thalamo-OFC connectivity on the left side was greater in TD, and the thalamo-SMC connectivity on the left side and both sides considered together were greater in the RD group.

3.4. Discussion and conclusion

This study used diffusion tractography to examine the association between thalamo-cortical connectivity and children's reading ability. Given the thalamus' central

role in neural function, we hypothesized that we would see thalamo-cortical connectivity differences in reading related regions between groups of good and poor readers. Results showed no differences in OTC or TPC; however, we did find group differences in the anterior perisylvian region. Specifically, the most prominent group differences were found in sensorimotor cortex (SMC), particularly on the left side, with RD showing *greater* thalamic-SMC connectivity than TD; SMC also showed greater relative SMC gray matter volume in RD. Additional findings showed greater left orbital frontal cortex (OFC) and right insula (Ins) thalamic connectivity in TD.

The central findings of abnormal thalamic and SMC connectivity suggests a thalamo-cortical role in reading that until now has not been a central focus in neuroimaging studies of RD, although a role of sensori-motor function in reading development has long been hypothesized (Heilman et al., 1995). More specifically, acquiring phonological representations and connections to orthographic forms (most often occurring within the context of writing) is thought to engage thalamo-SMC connections. These connections would be most critical in the early phases of reading acquisition, and would presumably be less relied upon with increased reading proficiency. From this standpoint, the greater thalamo-SMC connectivity in RD as compared to TD may reflect a prolonged multisensory engagement phase in developing reading skills for

the children with RD. During development, pruning of gray matter is a central part of maturation. Indeed, the process of cortical brain maturation begins first in dorsal parietal cortices, particularly the primary sensorimotor areas, and then spreads rostrally over the frontal cortex and caudally and laterally over the parietal, occipital, and finally the temporal cortex (Gogtay et al., 2004). This finding, in combination with the greater connectivity of SMC may suggest a less mature subcortical-SMC system in children with RD. Indeed, there is evidence that an early motor delay is associated with later language development and a delay in acquiring fluent reading skill (Viholainen et al., 2006). Although this finding was obtained from a younger population ranging from 2-5 years old, the delay in reading skills acquisition could cascade to the adolescent stage, due to a deficiency in an integrated neural system. Specifically, when a child first comes to read, his/her neural basis for linguistics, such as visual and motor processes, has already been well-established, yet these systems are not integrated in a way that supports reading. In response to the demands of learning to read on extant circuits for mapping print to sounds, novel functional connections also form between circuits (Schlaggar and McCandliss, 2007), as seen in the case of multisensory integration studies of letter and letter-sounds (Van Atteveldt et al. 2004). Also, previous literature has reported a pattern of strong recruitment of extrastriate regions in young readers when performing word generation

tasks, which gradually diminishes with age (Brown et al. 2005; Schlaggar et al. 2002). This could reflect migration of core brain regions in the circuits to deal with new cognitive demands in response to learning and practicing, or in other words, a reflection of increased automaticity.

In contrast to the SMC findings, both Ins and OFC showed greater thalamic connectivity for TD as compared to RD. These regions have far less specificity than SMC, supporting a variety of different cognitive processes. The insula plays an integrative role in mediating cognitive brain functions. Previous studies have shown that insula contributes to multi-modal processes, including motion (all motor tasks, such as movement of face, mouth and tongue, irrespective of side) and language (semantic, syntactic, phonological, orthographic decisions and listening to language; Kurth et al., 2010). All these findings may suggest that the insula could be a more domain general component of the neural network that supports phonological decoding skills, i.e., insula is not necessarily particularly selective to serve the language network alone, but it may play a role therein. Alternatively, given its integrative role, the insula may simply serve as a way-station between regions performing domain specific tasks. Similarly, the OFC is known for higher level cognitive functions, and therefore may also play an integrative or supervisory role (Elliott et al., 2000; Hampshire and Owen, 2006) in coordinating

subcortical-cortical regions. Our findings therefore support the supposition that the TD group shows more well developed connectivity patterns between multi-function cortical areas, whereas the RD group shows more thalamic connections in basic sensory-motor systems.

In summary, our findings suggest that RD subjects have substantially greater connectivity between thalamus and SMC, coupled with greater gray matter volumes in SMC. In contrast, the TD group showed greater thalamo-cortical connectivity to regions that subserve multiple cognitive functions. These findings present one possible intriguing interpretation: that during normal reading development, there is an initial reliance on sensorimotor cortex for developing phonemic representations and orthographic forms; however, with maturation and pruning of SMC, and developing efficiency in reading networks, connectivity for typically developing readers migrate away from primary motor/sensorimotor regions to tertiary cortical regions. Clearly, longitudinal studies and innovative experimental designs will be needed to disentangle these hypotheses, but the current study offers insights and future directions for studying the areas of abnormality in subcortical-cortical connectivity patterns in RD.

It is important to mention that the current study used the whole insula as a cortical target region, yet the anterior insula and posterior insula have been reported to

have distinct functions (Kurth et al., 2010; Menon and Uddin, 2010). Therefore, it would be fruitful for future connectivity studies to divide the insula according to its functional differentiations, and also do more fine grained division of other cortical regions. While we did not find differences when dividing SMC into smaller regions, it is possible that more advanced fiber tracking algorithms would reveal differences between various parts of SMC.

The current study examined, for the first time, the *in vivo* relationship between thalamo-cortical connectivity and children's reading ability. The results suggest that the thalamus may play a key role in reading behavior by mediating the functions of task specific cortical regions; such findings lay the foundation for future studies to investigate further anomalies in the development of thalamo-cortical connectivity in RD.

This study shows that DTI and DT-based tractography can provide useful evidence of the role of the thalamus in mediating reading behavior among children with and without reading difficulties. Similar approaches might be useful in the study of subcortical structures in neurodegenerative disorders.

REFERENCES

1. Behrens, T.E., Berg, H.J., Jbabdi, S., Rushworth, M.F., Woolrich, M.W., 2007.

Probabilistic diffusion tractography with multiple fibre orientations: What can we gain? Neuroimage 34, 144-155.

2. Behrens, T.E., Johansen-Berg, H., Woolrich, M.W., Smith, S.M., Wheeler-Kingshott, C.A., Boulby, P.A., Barker, G.J., Sillery, E.L., Sheehan, K., Ciccarelli, O., Thompson, A.J., Brady, J.M., Matthews, P.M., 2003a. Non-invasive mapping of connections between human thalamus and cortex using diffusion imaging. Nat Neurosci 6, 750-757.

3. Behrens, T.E., Woolrich, M.W., Jenkinson, M., Johansen-Berg, H., Nunes, R.G., Clare, S., Matthews, P.M., Brady, J.M., Smith, S.M., 2003b. Characterization and propagation of uncertainty in diffusion-weighted MR imaging. Magn Reson Med 50, 1077-1088.

4. Brown, T.T., Lugar, H.M., Coalson, R.S., Miezin, F.M., Petersen, S.E., Schlaggar, B.L., 2005. Developmental changes in human cerebral functional organization for word generation. Cereb Cortex 15, 275-290.

5. Dale, A.M., Fischl, B., Sereno, M.I., 1999. Cortical surface-based analysis. I. Segmentation and surface reconstruction. Neuroimage 9, 179-194.

6. Dale, A.M., Sereno, M.I., 1993. Improved localization of cortical activity by combining EEG and MEG with MRI cortical surface reconstruction: a linear approach. J Cogn Neurosci 5, 162–176.

7. Davis, N., Fan, Q., Compton, D.L., Fuchs, D., Fuchs, L.S., Cutting, L.E., Gore, J.C., Anderson, A.W., 2010. Influences of Neural Pathway Integrity on Children's Response to Reading Instruction. Front Syst Neurosci 4, 150.

8. Desikan, R.S., Ségonne, F., Fischl, B., Quinn, B.T., Dickerson, B.C., Blacker, D., Buckner, R.L., Dale, A.M., Maguire, R.P., Hyman, B.T., Albert, M.S., Killiany, R.J., 2006. An automated labeling system for subdividing the human cerebral cortex on MRI scans into gyral based regions of interest. Neuroimage 31, 968-980.

9. Díaz, B., Hintz, F., Kiebel, S.J., von Kriegstein, K., 2012. Dysfunction of the auditory thalamus in developmental dyslexia. Proc Natl Acad Sci U S A 109,

13841-13846.

10. Elliott, R., Dolan, R.J., Frith, C.D., 2000. Dissociable functions in the medial and lateral orbitofrontal cortex: evidence from human neuroimaging studies. Cereb Cortex 10, 308-317.

11. Fiebach, C.J., Friederici, A.D., Müller, K., von Cramon, D.Y., 2002. fMRI evidence for dual routes to the mental lexicon in visual word recognition. J Cogn Neurosci 14, 11-23.

12. Fischl, B., Dale, A.M., 2000. Measuring the thickness of the human cerebral cortex from magnetic resonance images. Proc Natl Acad Sci U S A 97, 11050-11055.

13. Fischl, B., Liu, A., Dale, A.M., 2001. Automated manifold surgery: constructing geometrically accurate and topologically correct models of the human cerebral cortex. IEEE Trans Med Imaging 20, 70-80.

14. Fischl, B., Salat, D.H., Busa, E., Albert, M., Dieterich, M., Haselgrove, C., van der Kouwe, A., Killiany, R., Kennedy, D., Klaveness, S., Montillo, A., Makris, N., Rosen, B., Dale, A.M., 2002. Whole brain segmentation: automated labeling of neuroanatomical structures in the human brain. Neuron 33, 341-355.

15. Fischl, B., Salat, D.H., van der Kouwe, A.J., Makris, N., Ségonne, F., Quinn, B.T., Dale, A.M., 2004. Sequence-independent segmentation of magnetic resonance images. Neuroimage 23 Suppl 1, S69-84.

16. Galaburda, A.M., Eidelberg, D., 1982. Symmetry and asymmetry in the human posterior thalamus. II. Thalamic lesions in a case of developmental dyslexia. Arch Neurol 39, 333-336.

17. Gogtay, N., Giedd, J.N., Lusk, L., Hayashi, K.M., Greenstein, D., Vaituzis, A.C., Nugent, T.F., Herman, D.H., Clasen, L.S., Toga, A.W., Rapoport, J.L., Thompson, P.M., 2004. Dynamic mapping of human cortical development during childhood through early adulthood. Proc Natl Acad Sci U S A 101, 8174-8179.

18. Hammill, D.D., Weiderholt, J.L., Allen, E.A., 2006. Test of Silent Contextual Reading Fluency (TOSCRF) Austin, TX: Pro-Ed.

19. Hampshire, A., Owen, A.M., 2006. Fractionating attentional control using event-related fMRI. Cereb Cortex 16, 1679-1689.

20. Heilman, K.M., Voeller, K., Alexander, A.W., 1996. Developmental dyslexia: a motor-articulatory feedback hypothesis. Ann Neurol 39, 407-412.

21. Hoeft, F., Meyler, A., Hernandez, A., Juel, C., Taylor-Hill, H., Martindale, J.L., McMillon, G., Kolchugina, G., Black, J.M., Faizi, A., Deutsch, G.K., Siok, W.T., Reiss, A.L., Whitfield-Gabrieli, S., Gabrieli, J.D., 2007. Functional and morphometric brain dissociation between dyslexia and reading ability. Proc Natl Acad Sci U S A 104, 4234-4239.

22. James, K.H., Gauthier, I., 2006. Letter processing automatically recruits a sensory-motor brain network. Neuropsychologia 44, 2937-2949.

23. Jenkinson, M., Bannister, P., Brady, M., Smith, S., 2002. Improved optimization for the robust and accurate linear registration and motion correction of brain images. Neuroimage 17, 825-841.

24. Jenkinson, M., Smith, S., 2001. A global optimisation method for robust affine registration of brain images. Med Image Anal 5, 143-156.

25. Johansen-Berg, H., Behrens, T.E., Sillery, E., Ciccarelli, O., Thompson, A.J., Smith, S.M., Matthews, P.M., 2005. Functional-anatomical validation and individual variation of diffusion tractography-based segmentation of the human thalamus. Cereb Cortex 15, 31-39.

26. Johnson, M.D., Ojemann, G.A., 2000. The role of the human thalamus in language and memory: evidence from electrophysiological studies. Brain Cogn 42, 218-230.

27. Karussis, D., Leker, R.R., Abramsky, O., 2000. Cognitive dysfunction following thalamic stroke: a study of 16 cases and review of the literature. J Neurol Sci 172,

25-29.

28. Kurth, F., Zilles, K., Fox, P.T., Laird, A.R., Eickhoff, S.B., 2010. A link between the systems: functional differentiation and integration within the human insula revealed by meta-analysis. Brain Struct Funct 214, 519-534.

29. Lyon, G.R., 1995. Toward a definition of dyslexia. Annals of Dyslexia 45, 3-27.

30. Marenco, S., Stein, J.L., Savostyanova, A.A., Sambataro, F., Tan, H.Y., Goldman, A.L., Verchinski, B.A., Barnett, A.S., Dickinson, D., Apud, J.A., Callicott, J.H., Meyer-Lindenberg, A., Weinberger, D.R., 2012. Investigation of anatomical thalamo-cortical connectivity and FMRI activation in schizophrenia. Neuropsychopharmacology 37, 499-507.

31. Menon, V., Uddin, L.Q., 2010. Saliency, switching, attention and control: a network model of insula function. Brain Struct Funct 214, 655-667.

32. Niogi, S.N., McCandliss, B.D., 2006. Left lateralized white matter microstructure accounts for individual differences in reading ability and disability. Neuropsychologia 44, 2178-2188.

33. Portas, C.M., Rees, G., Howseman, A.M., Josephs, O., Turner, R., Frith, C.D., 1998. A specific role for the thalamus in mediating the interaction of attention and arousal in humans. J Neurosci 18, 8979-8989.

34. Preston, J.L., Frost, S.J., Mencl, W.E., Fulbright, R.K., Landi, N., Grigorenko, E., Jacobsen, L., Pugh, K.R., 2010. Early and late talkers: school-age language, literacy and neurolinguistic differences. Brain 133, 2185-2195.

35. Price, C.J., Wise, R.J., Watson, J.D., Patterson, K., Howard, D., Frackowiak, R.S., 1994. Brain activity during reading. The effects of exposure duration and task. Brain 117 (Pt 6), 1255-1269.

36. Richlan, F., Kronbichler, M., Wimmer, H., 2011. Meta-analyzing brain dysfunctions in dyslexic children and adults. Neuroimage 56, 1735-1742.

37. Rimrodt, S.L., Peterson, D.J., Denckla, M.B., Kaufmann, W.E., Cutting, L.E., 2010. White matter microstructural differences linked to left perisylvian language network in children with dyslexia. Cortex 46, 739-749.

38. Schlaggar, B.L., Brown, T.T., Lugar, H.M., Visscher, K.M., Miezin, F.M., Petersen, S.E., 2002. Functional neuroanatomical differences between adults and school-age children in the processing of single words. Science 296, 1476-1479.

39. Schlaggar, B.L., McCandliss, B.D., 2007. Development of neural systems for reading. Annu Rev Neurosci 30, 475-503.

40. Shaywitz, S.E., 1998. Dyslexia. N Engl J Med 338, 307-312.

41. Sled, J.G., Zijdenbos, A.P., Evans, A.C., 1998. A nonparametric method for automatic correction of intensity nonuniformity in MRI data. IEEE Trans Med Imaging 17, 87-97.

42. Ségonne, F., Dale, A.M., Busa, E., Glessner, M., Salat, D., Hahn, H.K., Fischl, B., 2004. A hybrid approach to the skull stripping problem in MRI. Neuroimage 22, 1060-1075.

43. Ségonne, F., Pacheco, J., Fischl, B., 2007. Geometrically accurate topology-correction of cortical surfaces using nonseparating loops. IEEE Trans Med Imaging 26, 518-529.

44. Torgesen, J.K., Wagner, R., Rashotte, C., 1997. Test of word reading efficiency (TOWRE). Austin, TX: PRO-ED.

45. Turkeltaub, P.E., Eden, G.F., Jones, K.M., Zeffiro, T.A., 2002. Meta-analysis of the functional neuroanatomy of single-word reading: method and validation. Neuroimage 16, 765-780.

46. van Atteveldt, N., Formisano, E., Goebel, R., Blomert, L., 2004. Integration of letters and speech sounds in the human brain. Neuron 43, 271-282.

47. Viholainen, H., Ahonen, T., Lyytinen, P., Cantell, M., Tolvanen, A., Lyytinen, H.,

2006. Early motor development and later language and reading skills in children at risk of familial dyslexia. Dev Med Child Neurol 48, 367-373.

48. Wagner, R.K., Torgesen, J.K., Rashotte, C.A., 1999. Comprehensive Test of Phonological Processing (CTOPP). Austin, TX: Pro-Ed.

49. Wechsler, D.L., 2003. Wechsler intelligence scale for children-IV (WISC). San Antonio, TX: The Psychological Corporation.

50. Wilson, B.A., Felton, R., 2004. Word Identification and Spelling Test (WIST). Austin, TX: PRO-ED.

51. Woodcock, R.W., 2001. Technical manual. Woodcock Johnson III. Itasca, IL: Riverside Publishing.

52. Woodcock, R.W., McGrew, K.S., Mather, N., Schrank, F.A., 2003. Woodcock–Johnson III diagnostic supplement to the tests of cognitive abilities. Itasca, IL: Riverside Publishing.

53. Zarei, M., Patenaude, B., Damoiseaux, J., Morgese, C., Smith, S., Matthews, P.M., Barkhof, F., Rombouts, S.A., Sanz-Arigita, E., Jenkinson, M., 2010. Combining shape and connectivity analysis: an MRI study of thalamic degeneration in Alzheimer's disease. Neuroimage 49, 1-8.

75. Zatorre, R.J., Evans, A.C., Meyer, E., Gjedde, A., 1992. Lateralization of phonetic and pitch discrimination in speech processing. Science 256, 846-849.

CHAPTER IV

MULTIPLE KERNEL SPHERICAL DECONVOLUTION

4.1. Introduction

Diffusion Weighted Imaging (DWI) (LeBihan et al., 1986) is an MR technique to characterize tissue microstructure *in vivo*, based upon the fact that the diffusion of water molecules is restricted by cellular membranes. Diffusion Tensor Imaging (DTI) (Basser et al., 1994) has become the most widely used tool to study the white matter structures of the brain non-invasively in clinical and experimental neurobiological research. By fitting the DW signal to a tensor model and identifying the primary diffusion direction of spins, DTI can reveal the orientation of major white matter fiber bundles (Basser et al., 2000). Parameters derived from DTI, such as mean diffusivity (MD) and fractional anisotropy (FA), have been demonstrated to provide valuable information on white matter microstructures in numerous neurobiological studies (Klingberg et al., 2000; Niogi ad McCandliss, 2006; Rimrodt et al., 2010). However, one of the fundamental drawbacks of DTI is the assumption of Gaussion diffusion, which limits its efficacy in brain regions where multiple white matter fiber bundles coexist. Given that the voxel size of a DTI

acquisition for human studies on a modern MR scanner is usually 2-3 mm and the typical axon diameter ranges from less than 1 micron to more than 30 microns in the human brain, the majority of voxels in the territories of brain white matter contain multiple fiber populations (Behrens et al., 2007; Jeurissen et al., 2012).

To address complex white matter structures, such as the coexistence of multiple fiber orientations, high angular resolution diffusion imaging (HARDI) methods have been developed. For example, diffusion spectrum imaging (DSI) (Wedeen et al., 2005), persistent angular structure MRI (PAS-MRI) (Jansons and Alexander, 2003), Q-ball Imaging (QBI) (Tuch 2004), and spherical deconvolution (SD) (Tournier et al., 2004) have all be proposed to overcome the limitations of DT-MRI. Diffusion Spectrum Imaging (DSI) and Persistent Angular Structure (PAS) are based on the Fourier transformation relationship between MR signals in q-space and protons' diffusion propagator function that reflects intra-voxel complex white matter structure. While DSI requires multiple q-shells be evaluated, PAS is feasible for single q-shell data. The acquisition time for DSI and computation time for PAS prohibit them from being widely used. Being a variation of DSI, QBI allows the orientation distribution function (ODF) to be evaluated from data acquired at a single b-value, by the use of the Funk–Radon Transform (FRT) of the diffusion weighted signal as an approximation to the ODF, which

describes the probability for a spin to diffuse in a given direction. Based on point spread function theory, the SD approach assumes the measured signal in a DW MR experiment is the fiber orientation distribution (FOD) function convolved with a response kernel. SD is applicable to DW MR measurements with a single b-value, and the FOD functions show sharper peaks than the ODF derived from QBI, and therefore reveals white matter structures more clearly.

The FODs can be estimated through spherical harmonic (SH) transformation directly (Tournier et al., 2004; Anderson, 2005), or obtained via a damped Richard-Lucy like algorithm iteratively (Dell'acqua et al., 2007, 2010). Both approaches require *a priori* knowledge of a response kernel, i.e., the DW signal profile of a single-fiber population. In most situations, the response kernel is axially symmetric about the fiber axis, and the most commonly used model for the response kernel is the diffusion tensor. Clearly, the response kernel contains information that is characteristic of structural properties of nerve tissues, and may provide valuable information for neurobiological studies to explore for neural biomarkers. The deconvolution approaches generally rely on *a priori* knowledge of the response kernel, and thus do not provide an estimate of this property. The FORECAST model incorporates the response kernel as an unknown parameter and provides estimates of a common radial diffusivity that is shared by all fiber populations in

a single voxel. While this approach provides more information than standard SD, the assumption that different fiber populations share the same response kernel is not likely to be true. Hence, the interpretation of radial diffusivity estimates obtained from FORECAST is difficult.

With single shell DW data, it has been demonstrated that accurate fitting for multiple tensors in the general case is impossible (Scherrer et al., 2010). The difficulty rests in differentiating between isotropic components of the signal. Since the isotropic components do not show orientation dependence, one shell of DW data will yield a series of solutions, where contrast from volume fractions and diffusivities can compensate for each other. In this work, we propose a new MR method based on DW measurements, acquired at a few different b-values, which can resolve orientations of concurrently present multiple fiber populations and provide estimates of the diffusion properties intrinsic to each single-fiber population. We demonstrate that this framework is feasible for *in vivo* studies in terms of experimental settings. It is expected that the new method relaxes the "calibration" issues in SD FOD reconstruction (Parker et al., 2012).

4.2. Methods

4.2.1. Theory

4.2.1.1. Diffusion weight NMR signal and response kernel

In the DW experiment, the measured NMR signal has an exponential relationship with the diffusion tensor, $\boldsymbol{D}$, and the diffusion weighting matrix, $\boldsymbol{b}$,

$$S(\boldsymbol{b}) = S_0 e^{\left(-tr(\boldsymbol{b})\cdot \boldsymbol{r}^T \boldsymbol{D} \boldsymbol{r}\right)} \quad [1]$$

where S_0 is the corresponding signal with no diffusion weighting, $tr(\boldsymbol{b})$ is the trace of the $\boldsymbol{b}$ matrix, $\boldsymbol{r}$ is a unit vector along the direction of the diffusion weighting gradient, and $\boldsymbol{D}$ is the diffusion tensor. Under the assumption of short ramp time of gradients, the elements in the $\boldsymbol{b}$ matrix can be written as

$$b_{ij} = r_i r_j \cdot \gamma^2 G^2 \delta^2 (\Delta - \frac{\delta}{3}) \quad [2]$$

where γ is the gyromagnetic ratio of hydrogen, G and δ are the amplitude and duration of the diffusion weighting gradient pulses respectively, and Δ is the time between their rising edges.

In the situation of single fiber population, and assuming diffusion is symmetric about the axis of the fiber bundle, the corresponding diffusion tensor can be written in the form

$$D = \begin{bmatrix} \lambda_\perp & 0 & 0 \\ 0 & \lambda_\perp & 0 \\ 0 & 0 & \lambda_\parallel \end{bmatrix} \quad [3]$$

where $\lambda_\parallel$ denotes the diffusivity parallel to the axis of fiber bundle, called parallel diffusivity, and $\lambda_\perp$ denotes the diffusivity perpendicular to the fiber axis, called radial diffusivity. This is the simplest representation of a single-fiber response kernel. The diffusion measured along an arbitrary direction $D(\alpha, \beta)$, where α, β are the azimuthal and polar angles respectively, can be calculated according to the tensor by

$$\begin{aligned} D(\alpha,\beta) &= [\sin\beta\cos a \quad \sin\beta\sin a \quad \cos\beta] \begin{bmatrix} \lambda_\perp & 0 & 0 \\ 0 & \lambda_\perp & 0 \\ 0 & 0 & \lambda_\parallel \end{bmatrix} \begin{bmatrix} \sin\beta\cos a \\ \sin\beta\sin a \\ \cos\beta \end{bmatrix} \\ &= \sin^2\beta\cdot\lambda_\perp + \cos^2\beta\cdot\lambda_\parallel = \lambda_\perp + \cos^2\beta\cdot(\lambda_\parallel - \lambda_\perp) \\ &= \lambda_\perp + 3\cos^2\beta\cdot\left(\bar{\lambda} - \lambda_\perp\right) \end{aligned} \quad [4]$$

where $\bar{\lambda} = (\lambda_\parallel + 2\lambda_\perp)/3$ is the mean diffusivity.

In the presence of multiple fiber populations, the measured NMR signal has contributions from all compartments weighted by the volume fraction of each, or

$$S(tr(\boldsymbol{b}), \boldsymbol{r}) = S_0 \sum_{i=1}^{N_f} f_i e^{-tr(\boldsymbol{b})\cdot(\lambda_{\perp i} + 3\cos^2\beta_i\cdot(\bar{\lambda}_i - \lambda_{\perp i}))} \quad [5]$$

where i denotes the i^{th} fiber compartment, N_f is the total number of fiber compartments present, and f_i is the volume fraction of the i^{th} fiber compartment. In other words, the diffusion weighted signal measured in a DW NMR experiment depends

on angles between fiber axes and the direction of diffusion weighting gradient, the radial diffusivity and the difference between the mean diffusivity and radial diffusivity of each fiber compartments.

The representation of equation [5] can be generalized to arbitrary angular distributions of fibers:

$$S(tr(\boldsymbol{b}),\theta,\varphi) = S_0 \cdot \sum_{i=1}^{N_f} \int_0^{2\pi} \int_0^{\pi} P_i(\theta',\varphi') e^{-tr(\boldsymbol{b})\cdot(\lambda_{\perp i}+3\cos^2\beta_{RR'i}\cdot(\bar{\lambda}_i-\lambda_{\perp i}))} \sin\theta'\, d\theta'\, d\varphi' \quad [6]$$

where θ,φ are the polar and azimuthal angles of the diffusion weighting gradient direction R respectively, θ',φ' are the polar and azimuthal angles of fiber axis direction R' respectively, $P_i(\theta',\varphi')$ is the FOD function of the i^{th} single-fiber compartment, and $\beta_{RR'i}$ is the angle between R and R'. According to point spread function theory, $S(\theta,\varphi)$ is the convolution of $P_i(\theta',\varphi')$ with the corresponding kernel $e^{-tr(\boldsymbol{b})\cdot(\lambda_{\perp i}+3\cos^2\beta_i\cdot(\bar{\lambda}_i-\lambda_{\perp i}))}$ summed over all the fiber populations.

4.2.1.2. Spherical harmonics and orientation estimates

Any continuous function defined on a sphere, $F(\theta,\varphi)$, can be expanded in spherical harmonics by

$$F(\theta,\varphi) = \sum_{l=0}^{\infty} \sum_{m=-l}^{l} f_{lm} Y_{lm}(\theta,\varphi) \quad [7]$$

where $Y_{lm}(\theta,\varphi)$ is the spherical harmonic of order l and degree m evaluated at polar and azimuthal angles of (θ,φ), and its coefficients $f_{l,m}$ can be calculated by

$$f_{l,m} = \int_0^{2\pi}\int_0^{\pi} Y_{lm}^*(\theta,\varphi)F(\theta,\varphi)\sin\theta\, d\theta\, d\varphi \quad [8]$$

As shown in Figure 4.1, the spherical harmonic basis with even order $l > 0$ and degree $m = 0$ has a bipolar shape. For any axially symmetric real functions $F(\theta,\varphi)$, if the axis of $F(\theta,\varphi)$ is aligned with the primary (z) axis of the spherical harmonics, the corresponding SH coefficients bear a few characteristics: (1) $f_{l,-m} = (-1)^m \cdot (f_{l,m})^*$; (2) $f_{l,m} = 0$ for $m \neq 0$; and (3) $f_{l,m} = 0$ for $l = odd\ integers$, if $F(\theta,\varphi)$ is also symmetric about the origin. These mathematical characteristics of the spherical harmonic transformation provide an opportunity to decompose the NMR signal contributions from multiple differently oriented fiber populations. Specifically, again, the mixture signal is the summation of contributions from each population, which written in the SH space reads

$$\boldsymbol{s}_l = \sum_{i=1}^{N_f} \boldsymbol{W}_l(\theta_i,\varphi_i) * \boldsymbol{s}_{l,i} \quad [9]$$

where $\boldsymbol{s}_l$ is a column vector containing the SH coefficients of the mixture signal evaluated for order l and degree $m = -l, -l+1 \ldots, l$, similarly, $\boldsymbol{s}_{l,i}$ is a column vector containing the SH coefficients of the signal contribution from the i^{th} single-fiber

population, and $\boldsymbol{W}_l(\theta_i, \varphi_i)$ is the Wigner matrix of order l, which rotates the single-fiber coefficients from the coordinate system oriented along the single-fiber axis at (θ_i, φ_i) to the coordinates defined by the gradient set.

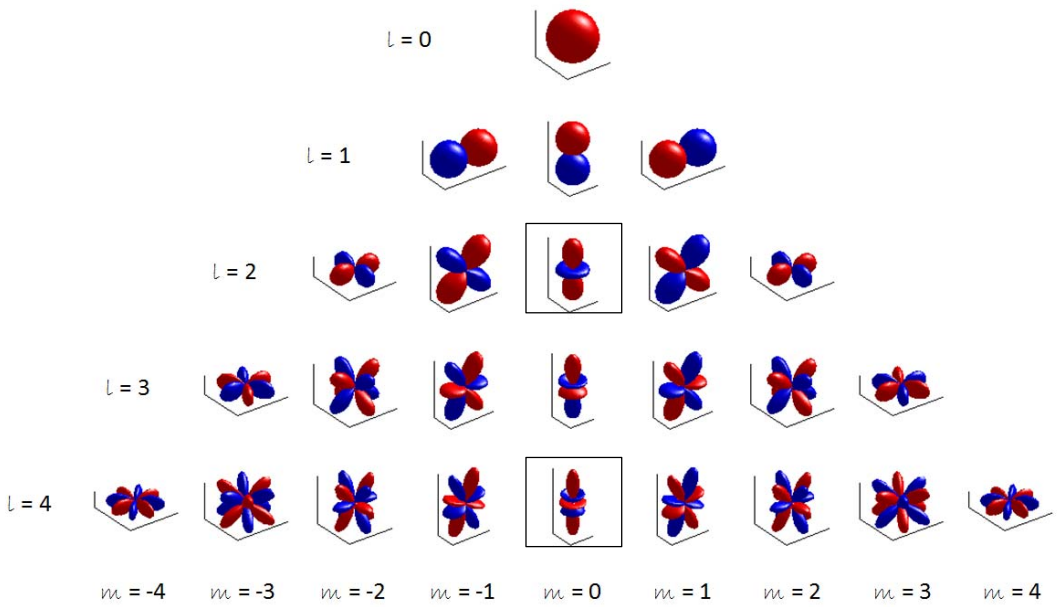

Figure 4. 1. Spherical harmonic basis functions of terms corresponding to l up to 4. Red represents positive amplitudes, while blue represents negative amplitudes. The terms, whose $l =$ even integers, $m = 0$, can be used to represent any axially symmetric real functions defined on a sphere. For example, the 0th order term is the spherical harmonic with zero variation, and thus represents the isotropic component of the measured signal; the non-zero order terms have bipolar shapes, and can be used to represent the anisotropy in diffusion weighted MR signals.

To identify the orientation of axes corresponding to multiple fiber populations, denote the aggregation of fiber orientations by $\boldsymbol{\Omega}$, i.e.,

$$\boldsymbol{\Omega} = \left(\theta_1, \varphi_1, \dots, \theta_i, \varphi_i, \dots, \theta_{N_f}, \varphi_{N_f}\right) \quad [10]$$

consider the fitting problem below:

$$\boldsymbol{\Omega} = \arg\min\{\left\|\tilde{S}(\theta,\varphi) - S(\theta,\varphi)\right\|\} \quad [11]$$

where $S(\theta,\varphi)$ is the measured signal, and $\tilde{S}(\theta,\varphi)$ is the model predicted signal, which can be written as

$$\tilde{S}(\theta,\varphi) = \sum_{l=0}^{\infty}\sum_{m=-l}^{l} s_{lm}Y_{lm}(\theta,\varphi) \quad [12]$$

or,

$$\tilde{\boldsymbol{S}} = \boldsymbol{Y} * \boldsymbol{s} \quad [13]$$

where $\tilde{\boldsymbol{S}}$ is a vector containing the spherical harmonic approximation of the measured diffusion weighted NMR signals, $\boldsymbol{s}$ is a vector containing SH coefficients s_{lm}, and $\boldsymbol{Y}$ is the design matrix of the linear regression problem

$$\boldsymbol{Y} = \begin{bmatrix} Y_{0,0}(\theta_1,\varphi_1) & Y_{1,-1}(\theta_1,\varphi_1) & Y_{1,0}(\theta_1,\varphi_1) & \cdots & Y_{l_{max},l_{max}}(\theta_1,\varphi_1) \\ Y_{0,0}(\theta_2,\varphi_2) & Y_{1,-1}(\theta_2,\varphi_2) & Y_{1,0}(\theta_2,\varphi_2) & \cdots & \vdots \\ Y_{0,0}(\theta_3,\varphi_3) & \vdots & \ddots & \cdots & \vdots \\ \vdots & \vdots & \vdots & \ddots & \vdots \\ Y_{0,0}(\theta_m,\varphi_m) & Y_{1,-1}(\theta_m,\varphi_m) & Y_{1,0}(\theta_m,\varphi_m) & \cdots & Y_{l_{max},l_{max}}(\theta_m,\varphi_m) \end{bmatrix} \quad [14]$$

Each row in $\boldsymbol{Y}$ corresponds to one diffusion weighting direction (θ_i,φ_i), and each column corresponds to one term of the spherical harmonics (l,m). Substituting equation [9] into equation [13], yields

$$\tilde{\boldsymbol{S}} = \boldsymbol{A}_0 \cdot s_{00} + \boldsymbol{A}_1 * \begin{Bmatrix} \boldsymbol{s}_{1,1} \\ \boldsymbol{s}_{1,2} \\ \vdots \\ \boldsymbol{s}_{1,N_f} \end{Bmatrix} + \cdots + \boldsymbol{A}_{l_{max}} * \begin{Bmatrix} \boldsymbol{s}_{l_{max},1} \\ \boldsymbol{s}_{l_{max},2} \\ \vdots \\ \boldsymbol{s}_{l_{max},N_f} \end{Bmatrix}$$

$$= \boldsymbol{A} * \begin{Bmatrix} s_{00} \\ \begin{Bmatrix} \boldsymbol{s}_{1,1} \\ \boldsymbol{s}_{1,2} \\ \vdots \\ \boldsymbol{s}_{1,N_f} \end{Bmatrix} \\ \vdots \\ \begin{Bmatrix} \boldsymbol{s}_{l_{max},1} \\ \boldsymbol{s}_{l_{max},2} \\ \vdots \\ \boldsymbol{s}_{l_{max},N_f} \end{Bmatrix} \end{Bmatrix} \quad [15]$$

$$\boldsymbol{A}_l = \begin{bmatrix} Y_{l,-l}(\theta_1, \varphi_1) & \cdots & Y_{l,l}(\theta_1, \varphi_1) \\ Y_{l,-l}(\theta_2, \varphi_2) & \cdots & Y_{l,l}(\theta_2, \varphi_2) \\ \vdots & \ddots & \vdots \\ Y_{l,-l}(\theta_m, \varphi_m) & \cdots & Y_{l,l}(\theta_m, \varphi_m) \end{bmatrix} * \left[\boldsymbol{W}_l(\theta_1, \varphi_1) \quad \cdots \quad \boldsymbol{W}_l\left(\theta_{N_f}, \varphi_{N_f}\right) \right] \quad [16]$$

$$\boldsymbol{A} = [\boldsymbol{A}_0 \quad \cdots \quad \boldsymbol{A}_l \quad \cdots \quad \boldsymbol{A}_{l_{\max}}] \quad [17]$$

wherein, the Wigner matrix acts as a rotation operator on the spherical harmonic coefficients. Assuming that the NMR signal profile, or response kernel, of a single-fiber population is symmetric about the fiber axis, the signal coefficients in a coordinate system aligned with the axis will satisfy

$$s_{lm,i} = 0, for\ m \neq 0 \quad [18]$$

Additionally, assuming that diffusion along any particular direction does not show polarity,

$$s_{lm,i} = 0, for\ l = odd\ integers, all\ i, all\ m \quad [19]$$

Then the equation [15] reduces to

$$\tilde{\boldsymbol{S}} = \boldsymbol{A}_0 \cdot s_{00} + \boldsymbol{A}_2 * \begin{Bmatrix} \boldsymbol{s}_{2,1} \\ \boldsymbol{s}_{2,2} \\ \vdots \\ \boldsymbol{s}_{2,N_f} \end{Bmatrix} + \cdots + \boldsymbol{A}_{l_{max}} * \begin{Bmatrix} \boldsymbol{s}_{l_{max},1} \\ \boldsymbol{s}_{l_{max},2} \\ \vdots \\ \boldsymbol{s}_{l_{max},N_f} \end{Bmatrix}$$

$$= \boldsymbol{A} * \begin{Bmatrix} s_{00} \\ \begin{Bmatrix} \boldsymbol{s}_{2,1} \\ \boldsymbol{s}_{2,2} \\ \vdots \\ \boldsymbol{s}_{2,N_f} \end{Bmatrix} \\ \vdots \\ \begin{Bmatrix} \boldsymbol{s}_{l_{max},1} \\ \boldsymbol{s}_{l_{max},2} \\ \vdots \\ \boldsymbol{s}_{l_{max},N_f} \end{Bmatrix} \end{Bmatrix} \quad [20]$$

$$\boldsymbol{s}_{l,i} = \left[0, 0, \ldots, s_{l0,i}, 0, \ldots, 0\right]^T, l = even\ integers \quad [21]$$

$$\boldsymbol{A} = \left[\boldsymbol{A}_0 \quad \boldsymbol{A}_2 \quad \ldots \quad \boldsymbol{A}_{l_{\max}}\right], l_{\max} = even\ integers \quad [22]$$

By solving for the orientations of fiber axes, $\boldsymbol{\Omega}$, the anisotropic components of the mixture NMR signal are decomposed into their single-fiber constituents.

4.2.1.3. Diffusivity estimates

Generally, it is challenging to perform tensor fitting (and hence derive the diffusivities of individual fiber populations) without separating the isotropic signal components pertaining to each tensor. However, it is even more challenging to decompose isotropic signal components without *a priori* knowledge of diffusivities, because isotropic signal contributions from different fiber populations are not distinguishable by orientation as anisotropic terms are. That becomes a major bottleneck

in algorithmic design, and makes the goal of estimating intrinsic diffusivities of multiple fiber populations extremely difficult to achieve.

By taking the spherical harmonic transformation of spherical functions (i.e., the NMR signal, response kernel and FOD function), the SH coefficients obtained can be considered a spectrum of the spherical variation in the particular function. Instead of using full spectra (i.e., all order terms), the fit for the response kernel becomes feasible by using partial spectra of the spherical functions ($l > 0$).

For the case of a single-fiber, the SH transformation of equation [6] simplifies to

$$s_{lm,i} = S_0 \cdot c_{l,i} \cdot p_{lm,i} \qquad [23]$$

where $s_{lm,i}$ is the SH coefficient of the measured signal $S(tr(\boldsymbol{b}), \theta, \varphi)$ corresponding to order l and degree m, $c_{l,i}$ is the SH coefficient of the response kernel of the i^{th} fiber (and is a function of $tr(\boldsymbol{b})$, $\lambda_{\perp i}$ and $\bar{\lambda}_i$), and $p_{lm,i}$ is the SH coefficient of the FOD function for the i^{th} fiber population (Anderson 2005). As shown above, $s_{lm,i}$ ($l > 0$) can be obtained by solving for $\boldsymbol{\Omega}$. Substituting different values of l and $tr(\boldsymbol{b})$ into equation [23] gives rise to a set of equations, with $\lambda_{\perp i}$, $\bar{\lambda}_i$ and $p_{lm,i}$ being unknowns. For example, if the number of $tr(\boldsymbol{b})$ values, denoted by N_b, is 3, and l_{max} is set to 6, this will give rise to $N_b * \frac{l_{max}}{2} = 9$ equations and $2 + \frac{l_{max}}{2} = 5$ unknowns (ignoring the isotropic l=0 terms, for the moment). While the experimental setting could be flexible, as

long as the number of equations is greater than (or equal to) the number of unknowns, the set of equations can be solved, resulting in a set of diffusivity estimates intrinsic to the i^{th} fiber population.

4.2.1.4. Fiber orientation distribution functions

The last step remaining to be completed is determining the FOD functions. The anisotropic components of the FOD are obtained together with the diffusivity estimates in the last step. The major goal of this step is to decompose the isotropic components to their respective fiber components.

The isotropic components of the signal do not have orientation dependence. The only contrast comes from the slight discrepancy in how the signal loss changes with respect to the *b* factor. To quantify the isotropic signal contributions from different single-fiber populations, we take the SH transformation of equation [6] again, and evaluate it for $l = 0$.

$$s_{00} = S_0 \cdot \sum_{i=1}^{N_f} (c_{0,i} \cdot p_{00,i}) \qquad [24]$$

In equation [24], s_{00} can be directly obtained by taking the SH transformation of the measured signal, $c_{0,i}$ is a known value given the diffusivity estimates from last section. Thus $p_{00,i}$ is the only unknown parameter. Additionally, $p_{00,i}$ is proportional to

volume fraction of the i^{th} fiber population, f_i, through the relation (Anderson, 2005):

$$p_{00,i} = \frac{1}{\sqrt{4\pi}} f_i \quad [25]$$

Thus,

$$\sum_{i=1}^{N_f} f_i + f_{iso} = 1 \quad [26]$$

Obviously, the number of *b* values used in the experiments sets an upper limit on the number of fiber bundles that can be identified. For example, the experimental setting of $N_b = 3$ gives rise to $N_b = 3$ equations (i.e., equation [24] for each *b* value), which can afford the degrees of freedom necessary to solve for the volume fractions of up to 3 different fiber bundles. The volume fraction of an isotropic compartment, f_{iso}, can be solved through equation [26] by assuming *a priori* knowledge of the diffusion coefficient. Depending on the needs of specific study, the MR acquisition can be adjusted to provide the desired information, namely, the degrees of freedom could be traded for scanning time.

4.2.1.5. Variations of the model

The model described above has the flexibility to be modified to fit the goals of a particular experiment. Given the practical trade-off between scanning time and the amount of information that can be drawn from the dataset, the signal to noise ratio (SNR)

in the acquired data may vary. In this section, we discuss how fitting for diffusivity and FOD simultaneously can affect the degrees of freedom in model fitting. We show how the number of unknown model parameters can be reduced in order to increase reliability at limited SNR. We also demonstrate how to incorporate extra parameters to provide a more precise description of complex tissue microstructure.

(a). Fitting for diffusivity and FOD simultaneously

Equations [23-26] use the anisotropic part of the signal corresponding to individual fiber populations to fit for the diffusivity and FOD separately. Alternatively, the diffusive and FOD parameters can be all included in a full model containing both anisotropic and isotropic components of the signal. Specifically, summing the signal contributions from all fiber populations gives

$$\{s_{lm}\} = \sum_{i=1}^{N_f} \boldsymbol{W}_l(\theta_i, \varphi_i) * \{s_{lm,i}\} \quad [27]$$

Substituing equation [23] into [27] yields

$$\{s_{lm}\} = S_0 \cdot \sum_{i=1}^{N_f} c_{l,i} \cdot \boldsymbol{W}_l(\theta_i, \varphi_i) * \{p_{lm,i}\} \quad [28]$$

where s_{lm} is the coefficient obtained by taking the SH transformation of the measured signal directly, $\boldsymbol{W}_l(\theta_i, \varphi_i)$ is the Wigner matrix corresponding to the ith fiber population. For all $l > 0$, equation [28] contains anisotropic components only, while for $l = 0$,

equation [27] should contain the contribution from the pure isotropic compartment in the voxel, which is written,

$$s_{00} = (S_0 \cdot \sum_{i=1}^{N_f} c_{0,i} \cdot \frac{f_i}{\sqrt{4\pi}}) + S_0 e^{(-tr(\boldsymbol{b})\cdot D_{iso})} \frac{f_{iso}}{\sqrt{4\pi}} \quad [29]$$

where D_{iso} and f_{iso} are the diffusivity and volume fraction of the isotropic compartment respectively.

The benefit of constructing the full model is increasing the degrees of freedom – the goodness of fit can be evaluated with the spherical harmonic coefficients of the measurements directly versus being evaluated with the $m = 0$ terms corresponding to a single fiber bundle. For example, consider the case of three fiber populations, that is, $N_f = 3$, $N_b = 3$, and $l_{max} = 6$. Fitting the anisotropic signal components gives rise to $N_b * \frac{l_{max}}{2} = 9$ equations for each fiber bundle. There are $N_f = 3$ separate sets of equations like this, and equation [24] can be evaluated once at each b value. As of unknowns, each fiber bundle yields $3 + \frac{l_{max}}{2} = 6$ unknowns corresponding to mean diffusivity, intrinsic FA, volume fraction and FOD coefficients for $l = 2, 4, 6$. In summary, putting N_f fiber bundles together yields $N_f \times N_b \times \frac{l_{max}}{2} + N_b = 30$ equations and $N_f \times 6 = 18$ unknowns. Now consider the larger model with an isotropic component of signals: taking the spherical harmonic transformation on both sides of

equation [6] gives rise to $N_b \cdot \sum_{l=0}^{l_{max}}(l+1) = 48$ $(l_{max} = even\ integer)$ equations in total, and the number of unknowns will be the same, i.e., $N_f \times 6 = 18$ in total. With different N_f, the number of known and unknown parameters are listed in Table 1. The main difference is the isotropic constituents of the signal. If the isotropic constituents of different fiber bundles are modeled, in contrast to fitting with anisotropic components only, we can evaluate the model with the measured signal directly.

Generally, increasing the degrees of freedom of the fitting problem will yield more stable results. On the other hand, including more unknown parameters elevates the complexity of the nonlinear search problem, which may increase computational cost and be detrimental to stability. Overall, the optimal approach depends on specific conditions, such as the number of shells, maximum order for SH fitting, each fiber population's intrinsic response kernel, and SNR.

(b). Simplifying the model: assuming the FOD is a Dirac delta function

Assuming axons are coherently aligned along the axis of the fiber bundle (i.e., there is no orientation spreading around the axis) is equivalent to treating the FOD as a spherical Dirac delta function. In the case of multiple, crossing fibers, each fiber would be represented by a delta function FOD with peak orientation aligned with the axis of that fiber and peak amplitude representing the volume fraction. With this additional

assumption, the ratio between the p_{l0} with different l is fixed, and the amplitudes are determined by the volume fraction of that particular fiber bundle in the voxel.

Treating the FOD as a spherical Dirac delta function is equivalent to fitting for multiple tensors. The benefit compared to allowing for axial splay (i.e., axon divergence) is that the number of parameters in each individual FOD representation decreases from 4 (p_{l0} corresponding to $l = 0, 2, 4, 6$) to 1 (the volume fraction of that fiber bundle). This helps to maintain the stability of the algorithm when the actual SNR in the data is low. The cost is that the splay will be reflected in the FA estimate, i.e., it will lead to underestimation of FA to account for axial splay (fiber divergence). The resulting total number of unknown parameters to fit was listed in Table 4.1.

(c). Model for more precision: fanning in single-fiber populations

There are situations in the brain where a fiber bundle splays in a planar manner, either branching or fanning. Since the m = 0 terms are axially symmetric, we need to consider including more terms in the representation of FOD in this case. As shown in the example in Figure 4.2, the amplitude modulation in each SH basis function is the combination of a sine-wave in the azimuthal angle (corresponding to degree m) and a Legendre polynomial in the polar angle (corresponding to order l). More examples of SH basis functions can be found in Figure 4.1. Obviously, we need azimuthal modulation

with period of π to describe planar splaying, or in other words, we need $m = 2$ terms in the FOD representations.

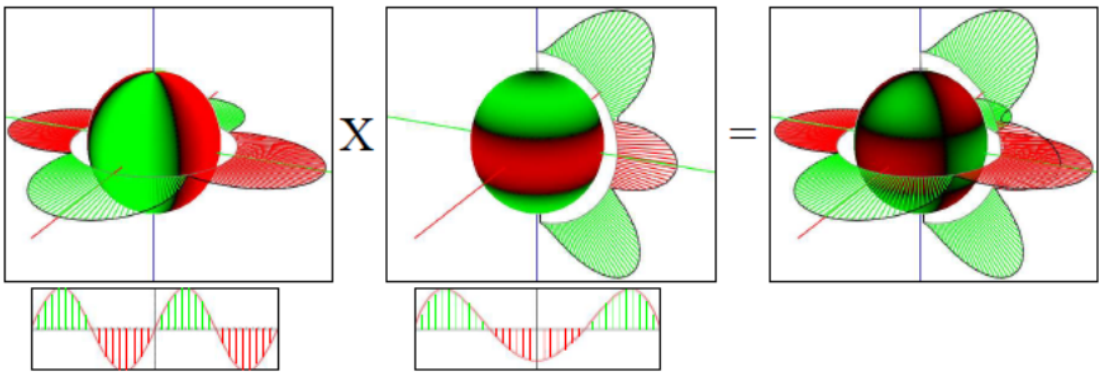

$\sin 2\varphi$ $\qquad$ $P_4^2(\cos\theta) = \frac{25}{2}(7\cos^2\theta - 1)\sin^2\theta$ $\qquad$ $Y_{4,2}(\theta, \varphi)$

Figure 4. 2. A demonstration of the angular variation in spherical harmonics. The left image shows the azimuthal dependence with the corresponding sine-wave (degree m = 2 in this example) while the center image displays the dependence on polar angle given by a Legendre polynomial (order l = 4 in this example). Combining both yields the right picture of the spherical harmonic basis function (Schönefeld, 2005).

Figure 4.3 illustrates how the m=2 terms can model fiber fanning with any arbitrary phase. Take s_{lm}, $l = 2$, $m = -2$, for example, the real part and imaginary parts of SH(2,-2) are orthogonal bases to each other, the relative ratio of real and imaginary parts of the coefficients determines the phase, and the absolute value of the complex coefficient determines the amplitudes of the peaks. Altogether, SH(2,-2) can characterize the phase and degree of fanning in FOD.

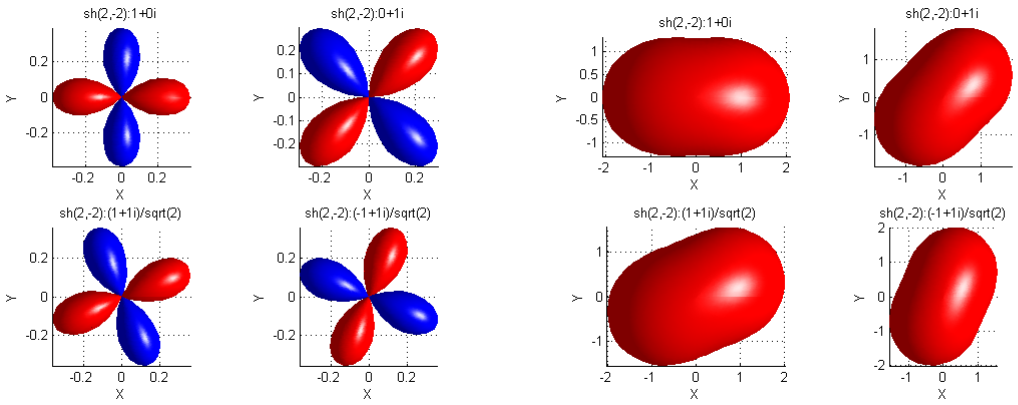

Figure 4. 3. Illustration of the SH representation of fanning at arbitrary phase angle. In the left are variations of SH(2,-2), whose primary axes are pointing out of the page. Red color represents positive peaks, and blue represents negative peaks. Peaks in the real and imaginary parts are 45 degrees apart, which is 1 period/4. A combination of two SH(2,-2) terms determines the net amplitude and phase of the angular variation. With an isotropic component added (right panel), the net function stretches out along the direction of positive peaks of SH(2,-2), and is damped in along the direction of negative peaks.

Hence, adding m = +/-2 terms allows for a more flexible FOD model to differentiate axially symmetric (including axial splay and FA) from the non-axially symmetric fiber orientation distributions. The resulting total number of unknown parameters in the fit was listed in Table 4.1.

Table 4. 1. Number of known and unknown parameters in response kernel fitting

N_f	total unknowns	Number of equations		Actual known/unknown in fitting	
		Assuming FOD is Dirac delta function			
		Anisotropic only	Full model	Anisotropic only	Full model
1	3	12	48	9/3	48/3
2	6	21	48	9/3	48/6
3	9	30	48	9/3	48/9
		Allowing axially symmetric splay			
		Anisotropic only	Full model	Anisotropic only	Full model
1	6	12	48	9/6	48/6
2	12	21	48	9/6	48/12
3	18	30	48	9/6	48/18
		Allowing axially symmetric splay and planar branching			
		Anisotropic only	Full model	Anisotropic only	Full model
1	10	21	48	18/10	48/10
2	20	39	48	18/10	48/20
3	30	57	48	18/10	48/30

Numbers are listed for $N_b = 3$.

4.2.2. Monte Carlo simulation

A Monte Carlo simulation was run to test for the variability of parameters estimated by the algorithm. A number of factors may exert an effect on the robustness of estimates, including the number of directions in the *b* matrix, SNR, crossing angles, number of fibers, mean diffusivity and intrinsic FAs. Different values for these variables were used to simulate the noise-free "truth" with Rician noise added. The values used for various variables are listed in Table 4.2. Three hundred iterations of Monte Carlo simulations were run for each combination of the values listed for all variable names.

Table 4. 2. Monte Carlo simulations of orientation and diffusivity estimates

Varying parameters for orientation estimates	
Variable name	values
nDirs	[33, 51, 70, 92]
SNR	[30, 50, 100, 200]
Crossing angle	[60^o, 90^o](2 fibers); $72^o/90^o/90^o$ (3 fibers)
Volume fractions	0.5/0.5 (2 fibers); 0.35/0.35/0.3 (3 fibers)
Mean diffusivity of all fibers	0.75 x 10^{-3} mm^2/s
Radial / mean diffusivity of all fibers	0.5
Varying parameters for diffusivity estimates	
Variable name	values
nDirs	70
SNR	[30, 50, 100, 120, 150, 200, 500]
Crossing angle	[60^o, 90^o](2 fibers); $72^o/90^o/90^o$(3 fibers)
Volume fractions	0.5/0.5 (2 fibers); 0.35/0.35/0.3 (3 fibers)
Mean diffusivity of fiber 1 (and 3)	0.75 x 10^{-3} mm^2/s
Mean diffusivity of fiber 2	[0.75, 0.65, 0.55, 0.45] x 10^{-3} mm^2/s
Radial / mean diffusivity of fiber 1 (and 3)	0.5
Radial / mean diffusivity of fiber 2	[0.2, 0.35, 0.5, 0.65]*

*The ratios of radial to mean diffusivity = [0.2, 0.35, 0.5, 0.65] are equivalent to FA = [0.9177, 0.8288, 0.7071, 0.5433]

4.2.3. In-vivo experiments

4.2.3.1. Data acquisition

In this study, diffusion weighted (DW) data were acquired along 70 directions evenly distributed on a sphere. Three shells of DW data were collected using a 3T Philips scanner with 32 channel head coil and *b* factor = 1000, 2000, 3000 s/mm^2. For each shell,

seven non-diffusion weighted images were collected for averaging, TR/TE = 10,000/63 ms, SENSE factor = 2. The scan time for each shell is about 13 minutes, which leads to a total scan time of 40 minutes for the diffusion measurement. The acquisition matrix was 96×96, and the voxel size was $2.5 \times 2.5 \times 2.5$ mm^3.

4.2.3.2. Image processing

Eddy current artifacts were corrected by registering the DW images to the non-DW image with an affine registration tool in the PRIDE toolset (Netsch and van Muiswinkel, et al., 2004. Image data from three separate scans (corresponding to the three different *b* values) were co-registered. The DTI FA maps were calculated in FSL (Jenkinson et al., 2003) using the FDT tool. The maps were then nonlinearly registered to the ICBM FA template using FNIRT (also part of the FSL package). The white matter atlas aligned with the ICBM template was then warped inversely to be aligned with the non-DW images in each individual's native space. These white matter masks were used for seed regions for fiber tracking.

The iterative spherical deconvolution (iSD, Dell'Acqua et al., 2007) algorithm was run on the data from each voxel in the brain. A watershed algorithm was used to detect peaks in the FOD resolved by the iSD method. When defining separate peaks: (a) if the crossing angle between two peaks was $\leq 35^{o}$, they were combined to produce one

peak; (b) if the magnitude ratio of a small peak to the largest peak is less than 1/8, the small peak is ignored, and its contribution to the FOD is combined into the large peak(s). The results of these analyses will be used as initial conditions for the nonlinear search in orientation estimates as the first step of the MKSD analysis. The implications of these threshold values are discussed below.

4.2.3.3. Fiber tracking

A deterministic fiber tracking algorithm was implemented in MATLAB. Seed points were evenly distributed in the seed regions, including the superior longitudinal fasciculus, corona radiata, and corpus callosum. Tracking began at each seed point, iteratively stepping along pathways. At each step, the local fiber orientation was trilinearly interpolated between surrounding voxels. MKSD fiber orientations more than 30 degrees from the current marching direction were reckoned as not belonging to the same anatomical fiber pathway, and were neglected from the interpolation. For voxels containing multiple fiber orientations, only the FOD peak yielding lowest curvature was selected. Fiber components with volume fractions below threshold (less than 1/8 of the total volume) were not included in the interpolation. Stopping criteria include: stepping into CSF or gray matter, turning sharply ($>45^{o}$), or reaching the threshold of maximum length (16cm).

4.2.4. Confidence estimation using the residual bootstrap

To estimate the reproducibility of the *in-vivo* results, we performed a residual bootstrap (Jeurissen et al., 2011) analysis to examine the variation range in the parameter estimates. Specifically, let $\boldsymbol{\varepsilon}$ be the noise vector, then

$$\boldsymbol{S} = \tilde{\boldsymbol{S}} + \boldsymbol{\varepsilon} \quad [30]$$

Where $\boldsymbol{S}$ is the measured DW signal vector, and $\tilde{\boldsymbol{S}}$, as described in equation [20], is the model predicted signal. Through the relation in equation [20], the spherical harmonic coefficients of signal contributions coming from each individual fiber population can be estimated using least-squares minimization:

$$\tilde{\boldsymbol{u}} = (\boldsymbol{A}^{\boldsymbol{T}}\boldsymbol{A})^{-1}\boldsymbol{A}^{\boldsymbol{T}} * \boldsymbol{S} \quad [31]$$

where

$$\tilde{\boldsymbol{u}} \triangleq \left\{ \begin{array}{c} s_{00} \\ \left\{ \begin{array}{c} \boldsymbol{s}_{2,1} \\ \boldsymbol{s}_{2,2} \\ \vdots \\ \boldsymbol{s}_{2,N_f} \end{array} \right\} \\ \vdots \\ \left\{ \begin{array}{c} \boldsymbol{s}_{l_{max},1} \\ \boldsymbol{s}_{l_{max},2} \\ \vdots \\ \boldsymbol{s}_{l_{max},N_f} \end{array} \right\} \end{array} \right\} \quad [32]$$

Given [20] and [31], the model predicted signal $\tilde{\boldsymbol{S}}$ can be calculated as

$$\tilde{\boldsymbol{S}} = \boldsymbol{H} * \boldsymbol{S} \quad [33]$$

with $$\boldsymbol{H} = \boldsymbol{A}(\boldsymbol{A}^{\boldsymbol{T}}\boldsymbol{A})^{-1}\boldsymbol{A}^{\boldsymbol{T}}$$ [34]

which is called the "hat-matrix". The resulting residual vector is given as

$$\tilde{\boldsymbol{\varepsilon}} = \boldsymbol{S} - \tilde{\boldsymbol{S}}$$ [35]

Then the raw residuals are corrected for leverage (Davison and Hinkley, 1999)

$$\tilde{\varepsilon}_{\boldsymbol{i}}^{\boldsymbol{m}} = \frac{\tilde{\varepsilon}_{\boldsymbol{i}}}{\sqrt{1 - h_{ii}}}$$ [36]

where h_{ii} is the i[th] diagonal entry in the hat matrix $\boldsymbol{H}$ in equation [34]. Next, the values from $\tilde{\boldsymbol{\varepsilon}}$ were randomly chosen with replacement to form a new set of bootstrapped residuals $\tilde{\boldsymbol{\varepsilon}}^*$. Finally, the bootstrapped residuals were added back to the signal fit, to create a synthetic set of DW signal:

$$\tilde{\boldsymbol{S}}^* = \tilde{\boldsymbol{S}} + \tilde{\boldsymbol{\varepsilon}}^*$$ [37]

We can then recalculate the fiber orientations using $\tilde{\boldsymbol{S}}^*$, get an updated $\boldsymbol{A}$ in equation [31] hence updated hat matrix $\boldsymbol{H}$ in equation [34], and iterate the process to build up a bootstrapped distribution of parameter estimates.

4.2.5. Reliability examination using the leave m out resampling algorithm

An alternative approach to estimate the reliability of the MKSD model is through the leave m out resampling (LMOR) approach. The original delete-one resampling method, or Jackknife, was introduced by Quenouille (1949) and Tukey (1958). It is widely used to sample the distribution and estimate the bias and variance of a statistic. It

can be generalized to ‘delete-m’ Jackknife. See Shao and Tu (1995) for Jackknife methods in more detail.

Inspired by the idea of ‘delete-m’ Jackknife, in this work, we used the LMOR approach to sample the distribution of estimated MKSD model parameters. Briefly, for each voxel, *N* observations were acquired, according to *N* diffusion weighting directions. The real estimate was obtained with all *N* data points. To sample the distribution of variance in model estimates, a subsample comprised of (*N*-*m*) observations was drawn from the original sample a total of *n* times. Each subsample was then passed to the MKSD analysis, yielding one sample of the distribution of model estimates. The sampled model estimates, together with the real estimate, could be assessed quantitatively then to judge the performance of the MKSD model in this particular voxel, i.e., whether the variance of model parameter estimates is below a preset threshold.

4.3. Results

4.3.1. Monte-Carlo simulation

4.3.1.1. Fiber orientation estimates

Two fibers crossing at 60 degrees (in the left panel) and at 90 degrees (in the right

panel) are shown in Figure 4.4. The result of each individual iteration is marked by a dot in the polar diagrams. The cross sign in black on top of individual dots marks the true value to simulate the noise-free signal. The distribution of fiber orientation estimates in polar and azimuthal angles was illustrated in rose histograms and bar histograms, respectively. Red color denotes information pertaining to the 1st fiber, and blue pertains to the 2nd fiber. As SNR and crossing angle increase, the estimates were increasingly robust. Similarly, as the number of directions increases, the estimates were increasingly robust, as shown in Figure 4.5.

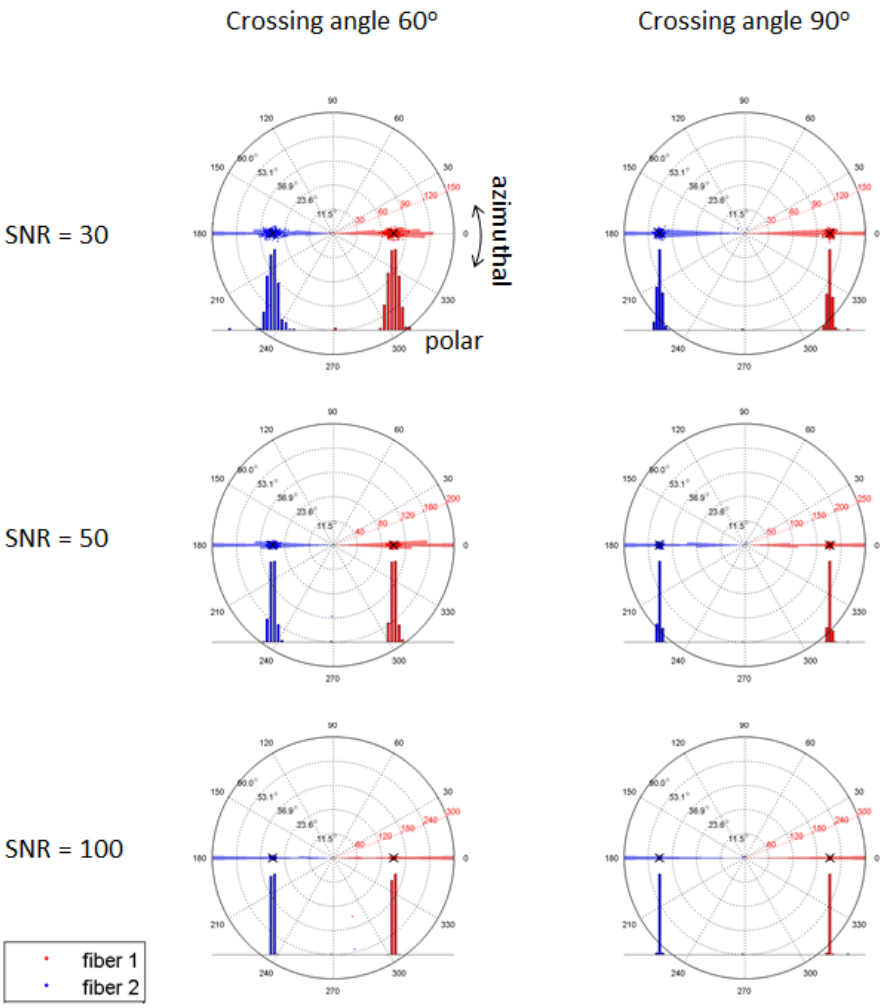

Figure 4. 4. Monte Carlo simulation of orientation estimates with different SNR and crossing angle. In the left panel, the crossing angle between the two fibers is 60 degrees; in the right panel, the crossing angle is 90 degrees. Each individual iteration was marked by a dot on the polar plot. The cross sign in black marked the true value to simulate the noise-free signal. The distribution of fiber orientation estimates in polar and azimuthal angles are illustrated in rose histograms and bar histograms, respectively. Red denotes information pertaining to the 1st fiber, and blue pertains to the 2nd fiber. The number of measurement directions was 70.

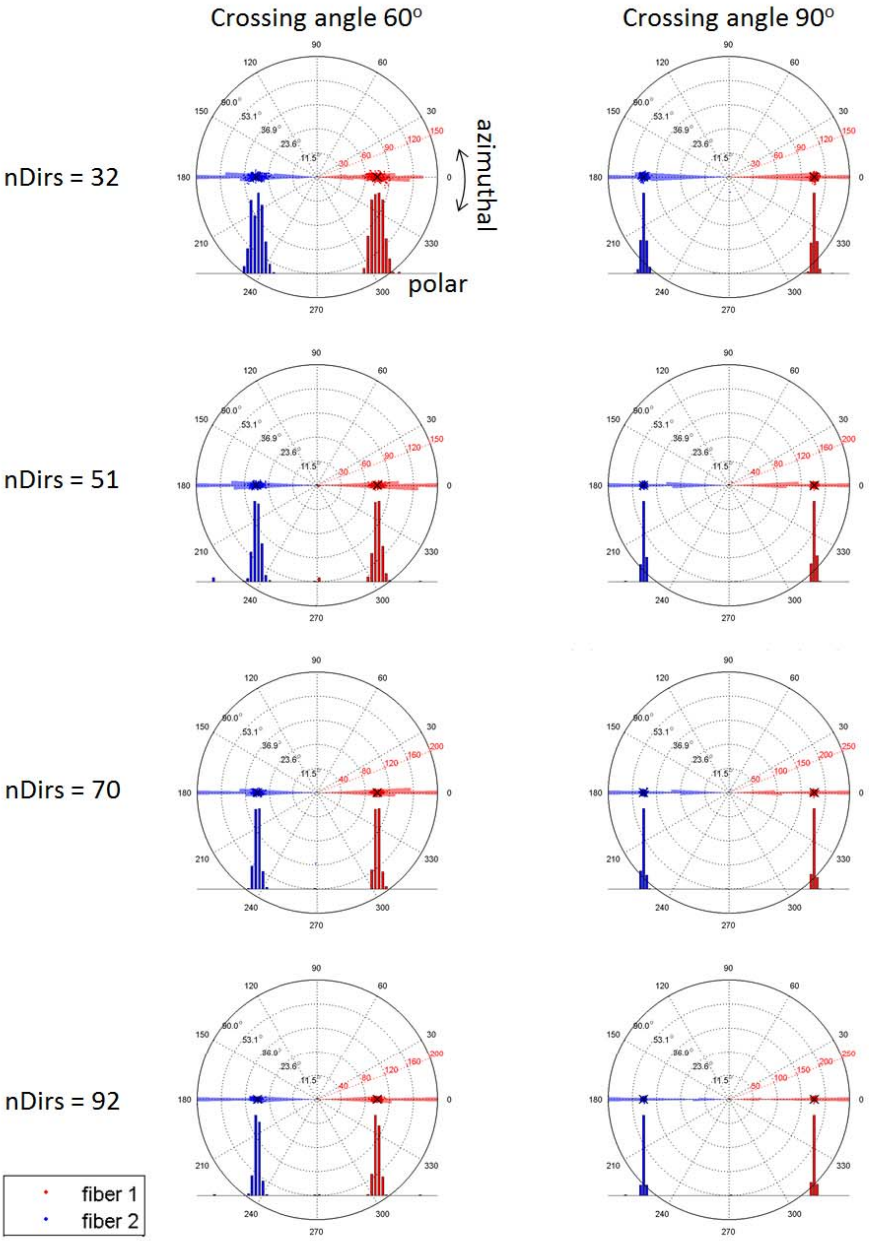

Figure 4. 5. Monte Carlo simulation of orientation estimates with different numbers of directions. In the left panel, the crossing angle between the two fibers is 60 degrees; in the right panel, the crossing angle is 90 degrees. Each individual iteration was marked by a dot on the polar plot. The cross sign in black marked the true value to simulate the noise-free signal. The distribution of fiber orientation estimates in polar and azimuthal angles are illustrated in rose histograms and bar histograms, respectively. Red denotes information pertaining to the 1st fiber, and blue pertains to the 2nd fiber. SNR was 50.

Across all different settings of SNR, number of directions, and crossing angles, the variability of the orientation estimates are summarized in Figure 4.6. The angular error was calculated as the angular difference between the calculated estimates and the true values used for signal generation. The variability of angular error was also estimated, calculated by the standard deviation of the angular errors across 300 iterations of Monte Carlo simulation. As expected, either increasing the number of diffusion weighting directions in the DW measurement or increasing the signal to noise ratio will help to decrease the estimation error and improve stability. It was also shown that the accuracy and reliability also depended on the crossing geometries. For example, it was more challenging to resolve more complex structures (3 fibers vs. 2 fibers), and fiber bundles whose axes were less far apart (60^o vs. 90^o).

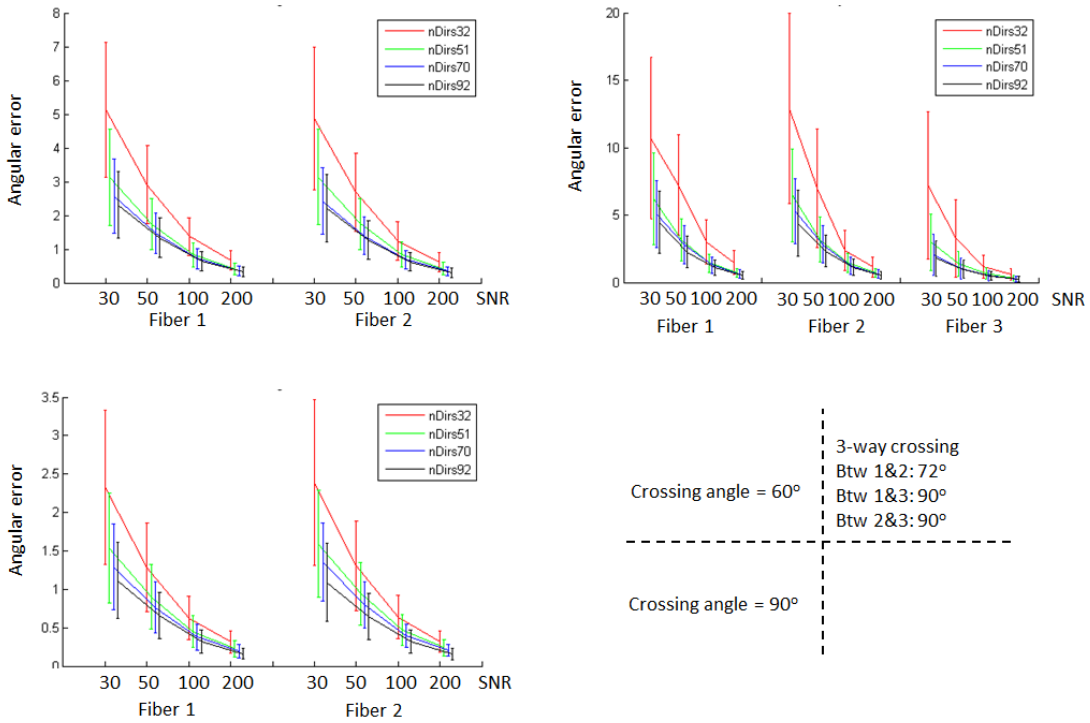

Figure 4. 6. Angular error in orientation estimates with various acquisition schemes and levels of SNR. Both the mean angular error and variability decreases as SNR increases. As the number of diffusion weighting directions increases, the variability decreases. The mean angular error was marked with the solid line, error bars denote the standard deviation. Different acquisition schemes were marked with different colors.

4.3.1.2. Diffusivity estimates

(a). Treating the FOD as a Dirac delta function

The simplest MKSD model treats the FOD of each individual fiber bundle as an ideal Dirac delta function. The Monte Carlo simulation results for this case are listed in Figures 4.7-4.8. As SNR increases, the variability decreases. There is not an obvious effect of intrinsic mean diffusivity on the variability.

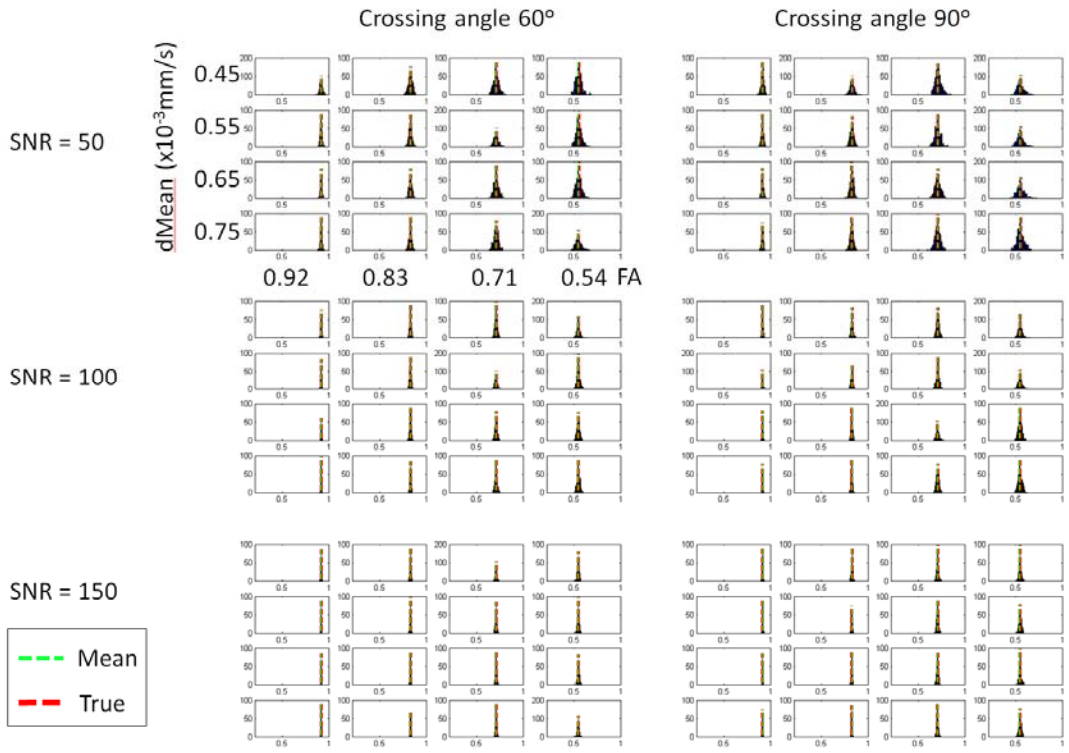

Figure 4. 7. Monte Carlo simulation of FA estimates for a Dirac delta FOD. In the left panel, the crossing angle between the two fibers is 60 degrees; in the right panel, the crossing angle is 90 degrees. The true values used to simulate the noise-free signal are marked with a green dashed line, and the mean value of the estimates are marked with red.

The variability of FA estimates with different combinations of crossing angle, mean diffusivity, FA and SNR were summed up in Figure 4.8. The standard deviation across all iterations of Monte Carlo simulation decreases as SNR increases. In addition, when other conditions are identical, high intrinsic FA leads to high robustness to noise. No bias was observed.

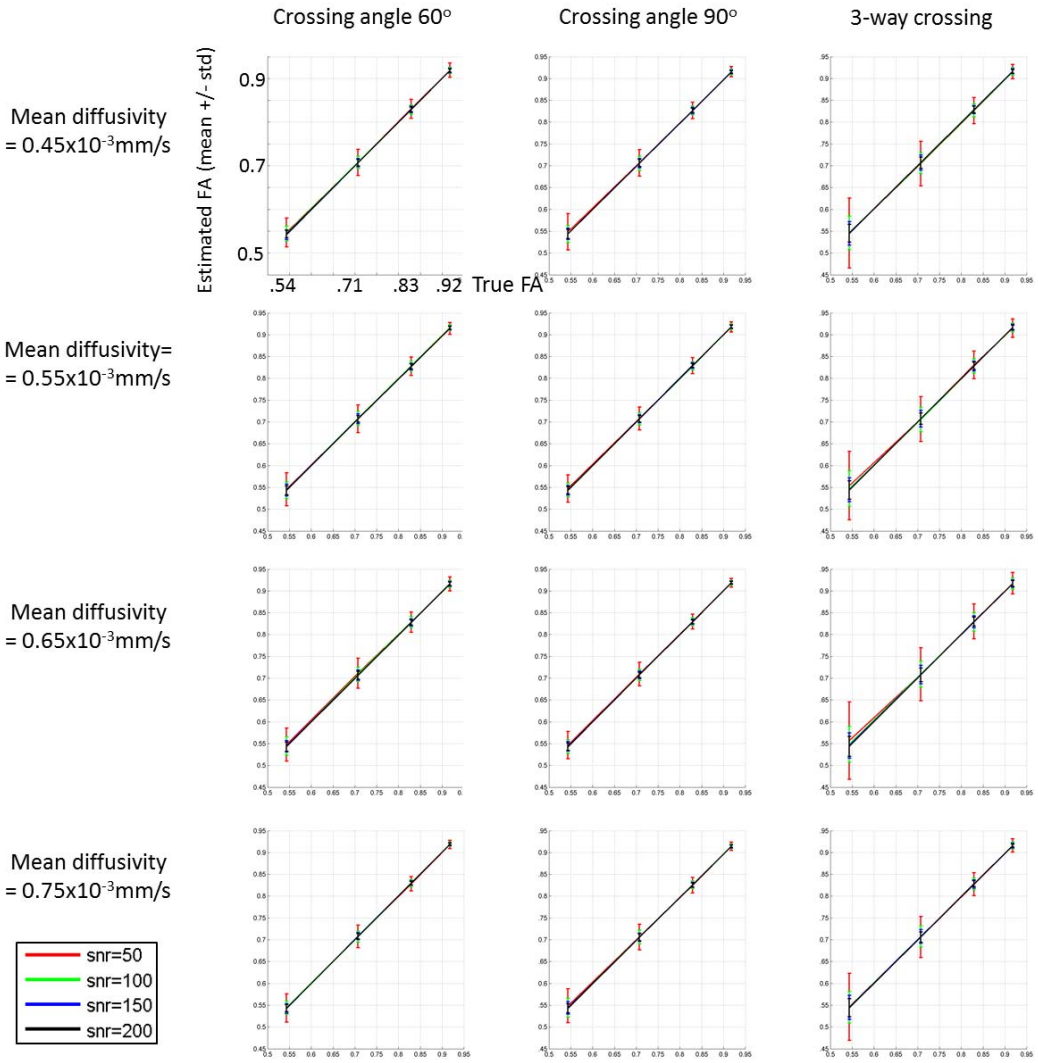

Figure 4. 8. FA estimates for treating the FOD is a Dirac delta function. Different settings were listed including various combinations of crossing angle, mean diffusivity, FA, and SNR. The mean values are joined by solid lines and the standard deviations across all iterations are marked with error bars. Different SNRs are labeled with different colors.

(b). Allowing for axially symmetric splay in the FOD

Similar to the previous case, if allowing for axially symmetric splays in the

FODs, as SNR increases, the variability in FA estimates decreases (Figure 4.9). The distributions are slightly more skewed when the intrinsic mean diffusivity is lower.

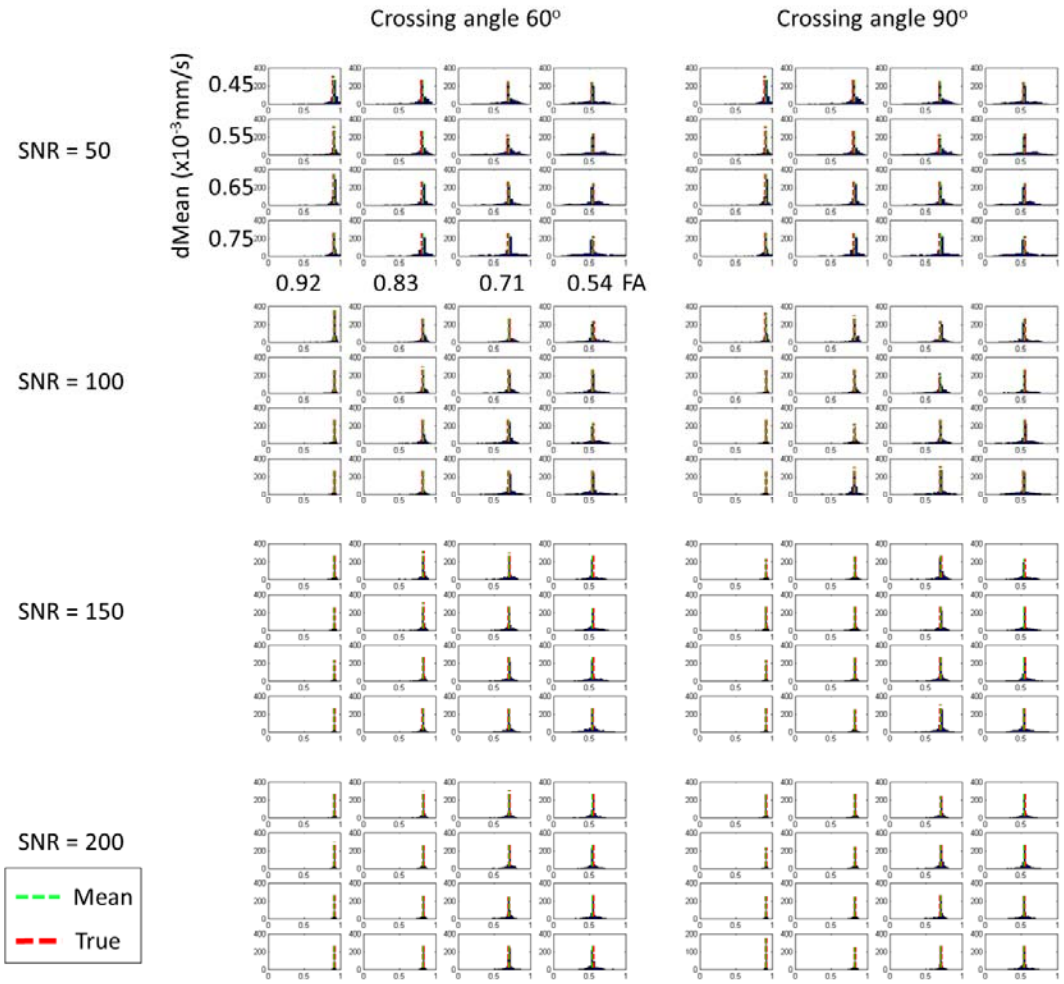

Figure 4. 9. Monte Carlo simulation of FA estimates allowing for axially symmetric splay in the FOD. In the left panel, the crossing angle between the two fibers is 60 degrees; in the right panel, the crossing angle is 90 degrees. The true values used to simulate the noise-free signal is marked with a green dashed line and the mean value of the estimates is marked with red.

The variability of FA estimates with different combinations of crossing angle, mean diffusivity, FA and SNR are summarized in Figure 4.10.

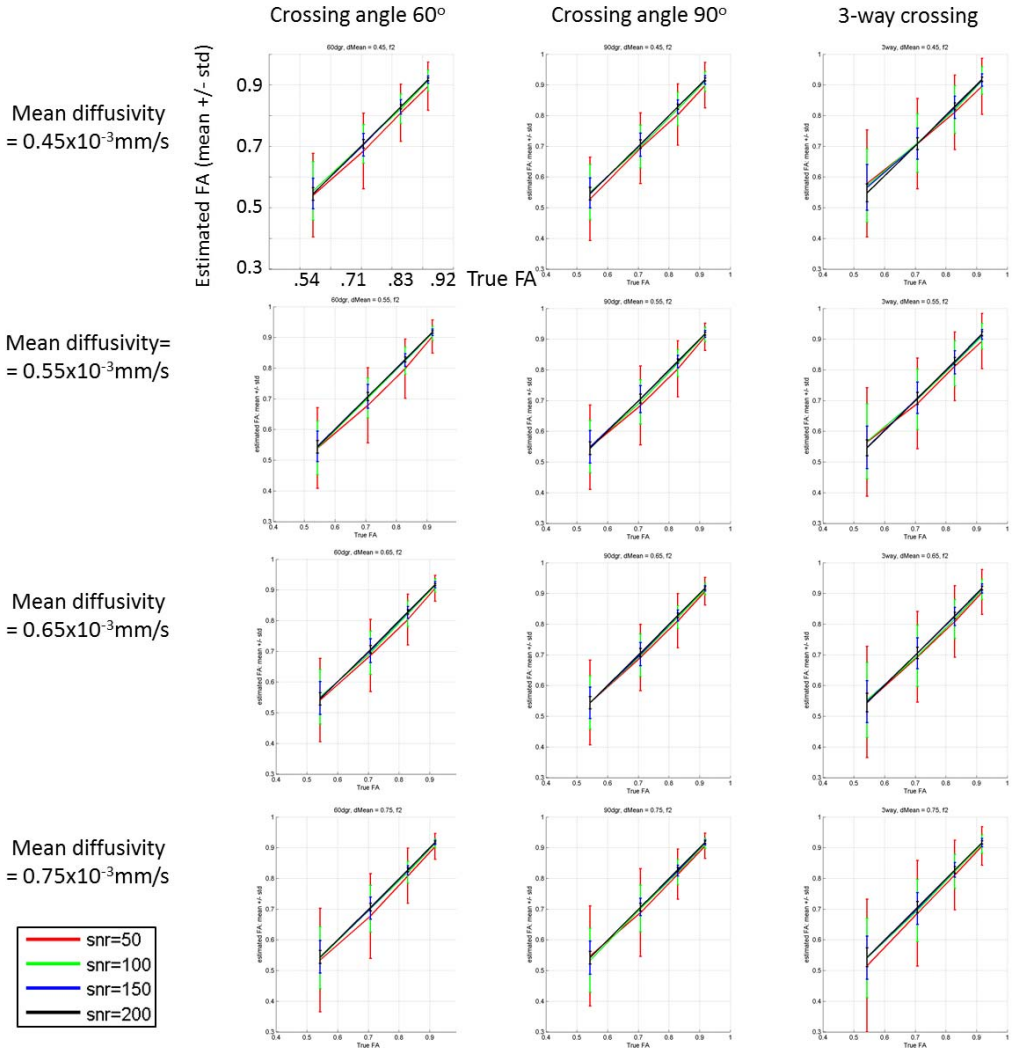

Figure 4. 10. FA estimates allowing for axially symmetric splay in the FOD. Different settings were listed including various combinations of crossing angle, mean diffusivity, FA, and SNR. The mean values are joined by solid lines and the standard deviations across all iterations are marked with error bars. Different SNRs are labeled with different colors.

(c). Allowing for planar fanning

Planar fanning was simulated as a group of discrete fiber axes in a vertical plane. The angle between each pair of consecutive fiber axes is 0.1^{o}. As the fanning increases,

i.e., the outmost fiber axis from the positive z-axis increases from 5° to 20° (Figure 4.10), the FOD became narrower in the y direction. Note that the width in the y direction does not reflect fanning, rather it is due to the truncation of higher order terms (in this exemplary demonstration, the maximum order l_{max} = 6). For example, the narrowing in y direction from 5° splay to 10° splay originates from normalization – the area under the FOD has to be 1, so as it gets wider in x, it must get narrower in y.

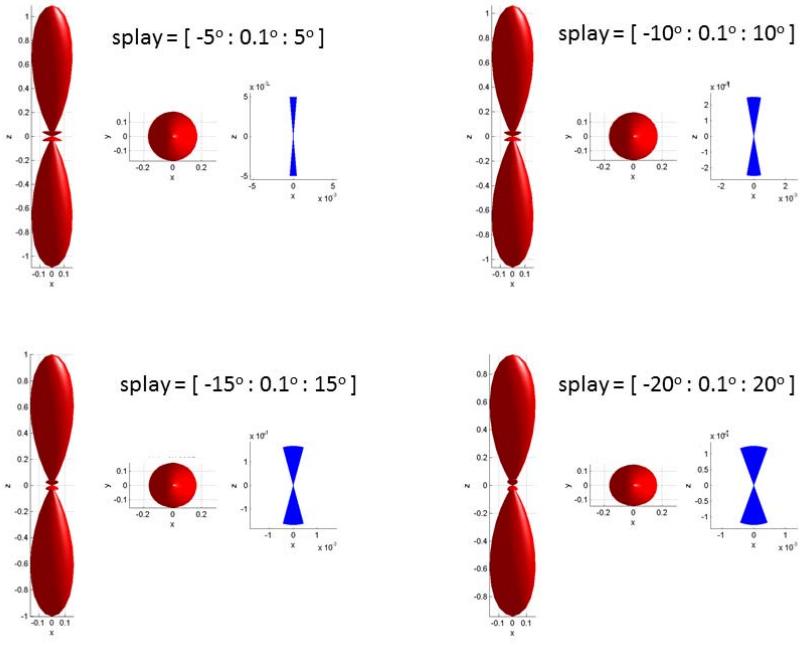

Figure 4. 11. Fanning in the FOD. Planar fanning in the FOD was simulated with a group of discrete fiber axes in the vertical plane (illustrated in blue). The angle between consecutive fiber axes is 0.1°, maximum fanning angles ranges from 5° to 20°. These discrete fiber orientations were used to generate noise-free DW signals according to the tensor relationship, and each orientation had the same volume fraction. The estimated FOD was rendered as surface plot in red, both front and top views are shown. The corresponding splaying fiber axes used for simulating the signal are shown on the right in blue.

When two fiber bundles cross, each with planar fanning, (Figure 4.12), the obtained FODs are squeezed in the direction perpendicular to the fanning plane.

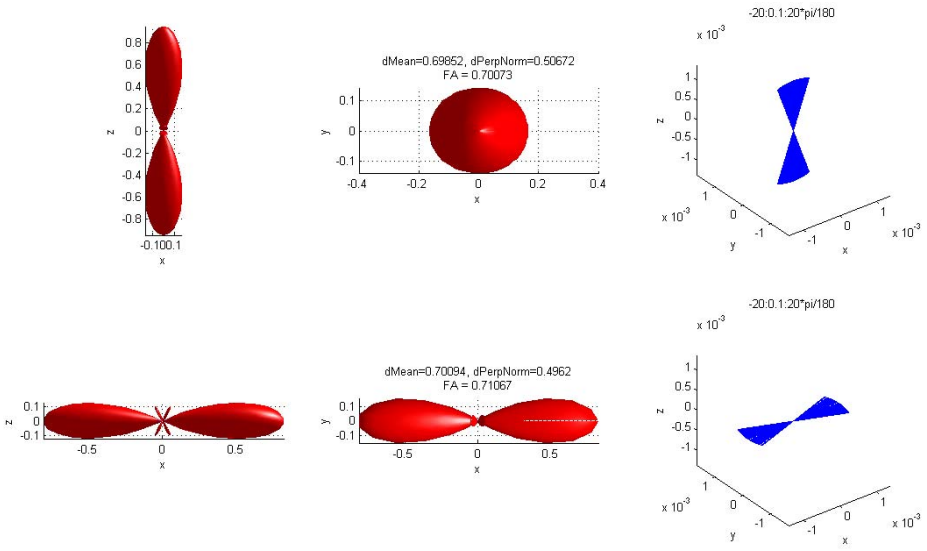

Figure 4. 12. Crossing fiber bundles with planar fanning. The obtained FODs were squeezed in the direction perpendicular to the fanning plane. The estimated FOD was rendered as a surface plot in red, both front and top views are shown. The corresponding splaying fiber axes used for simulating the signal are shown on the right in blue. The upper fiber simulates fanning in the x-z plane, and the fanning of the lower fiber bundle is in x-y plane.

The results of Monte Carlo simulation are shown in Figures 4.13.

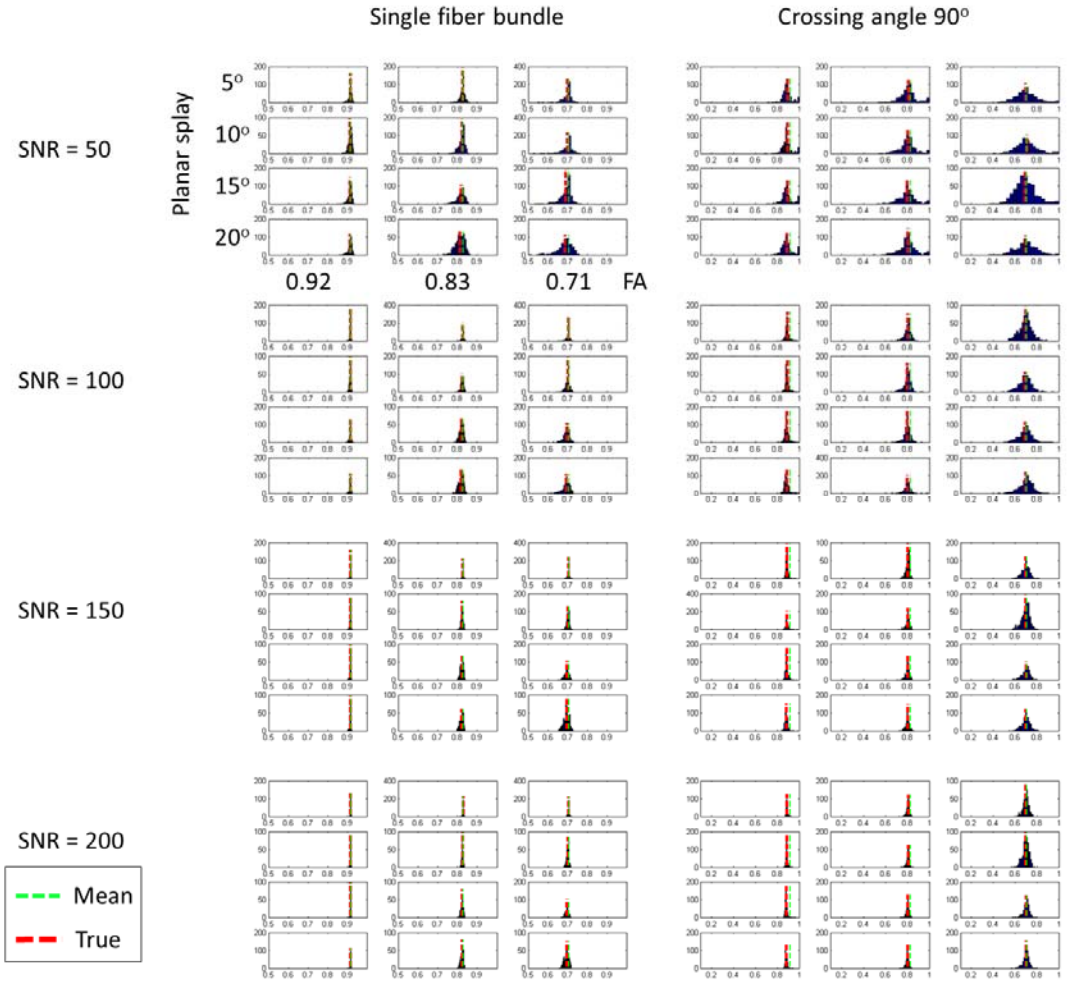

Figure 4. 13. Monte Carlo simulation of FA estimates for fanning fiber bundles. In the left panel, the signal was generated with a single fiber bundle with planar branching of different angles; in the right panel, two fiber bundles were aligned perpendicular to each other, as shown in Figure 4.11. The true values used to simulate the noise-free signal are marked with green dashed line and the mean values of the estimates are marked with red.

Similar to the results shown in Figures 4.8 and 4.10, in both single bundle and crossing cases, the variability of FA estimates decreases as SNR and true FA increase (Figure 4.14).

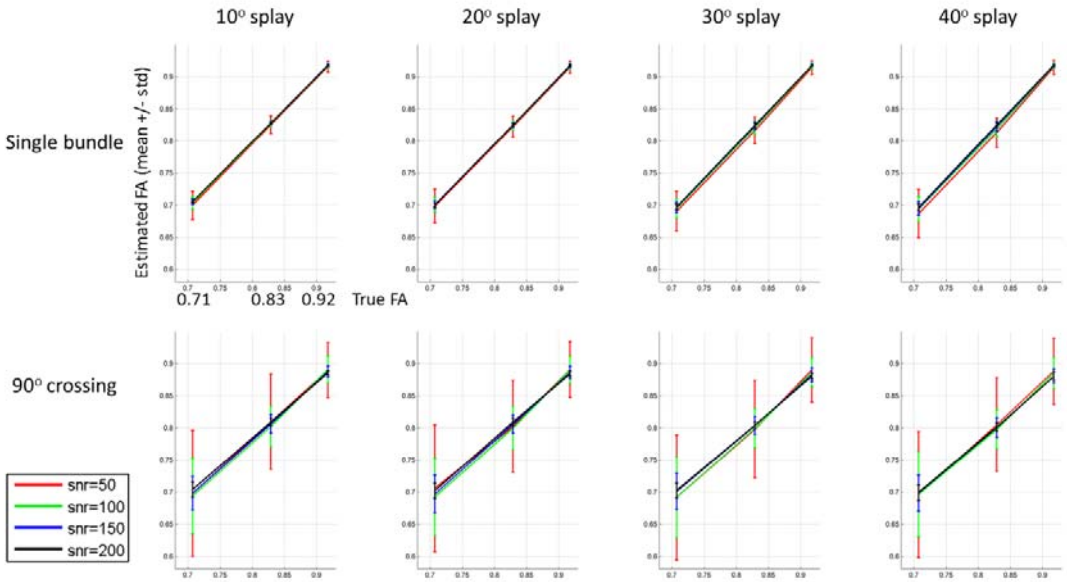

Figure 4. 14. FA estimates allowing for planar fanning in the FOD. Different parameter settings are shown including various combinations of crossing angle, degree of fanning and SNR. The mean values are joined by solid lines and the standard deviations across all iterations are marked with error bars. Different SNRs were labeled with different colors. Mean diffusivity was 0.75×10^{-3} mm^2/s.

4.3.2. In-vivo experiments

4.3.2.1. Multiple Kernel Spherical Deconvolution Fractional Anisotropy

The goals of MKSD analysis is to resolve crossing fibers and provide an estimate of the intrinsic FA in each fiber. Results are shown for one healthy adult participant in Figure 4.15c. Three crossing fiber bundles in the left hemisphere, namely the superior longitudinal fasciculus (SLF), corona radiata (CR) and callosal fibers (CF) were identified. The FA value intrinsic to each fiber bundle was rendered on the streamlines

(Figure 4.15 a-b). Considering the SNR in this dataset (SNR ~ 40) and the previous Monte Carlo simulation results, the whole brain MKSD analysis assumes the FOD of individual fiber bundles to be Dirac delta functions. For each vertex on the streamline, trilinear interpolation was performed among neighboring voxels which contain a fiber peak of the anatomic structure that current streamline belongs to (angular deviation $\leq 30°$).

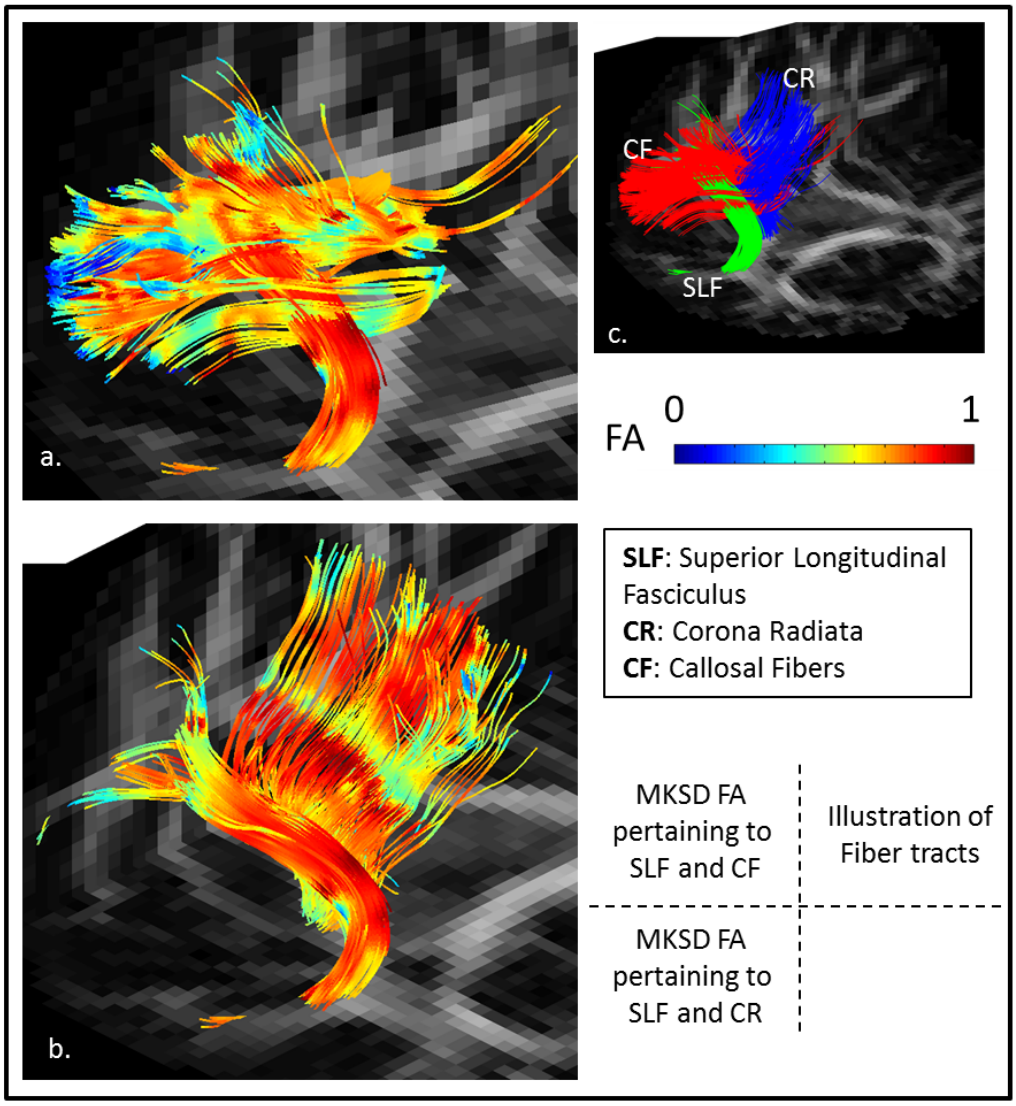

Figure 4. 15. The FA intrinsic to specific fiber bundles. Three fiber bundles were identified (c), and the FA of each fiber bundle, estimated by MKSD, was rendered on the streamlines (a, b).

4.3.2.2. Consistency with DTI FA

To test whether the FA estimates obtained from MKSD analysis are consistent with DTI analysis results, the cerebral peduncle was selected as region of interest, since this portion of the cortical spinal tract exhibits a high degree of fiber coherence. The

JHU-ICBM white matter atlas was used to identify voxels inside the cerebral peduncles. A simple linear correlation was performed between DTI FA and MKSD FA among voxels within bilateral cerebral peduncles where only one fiber peak was identified by iterative spherical deconvolution. On both sides of the brain, the MKSD FA was significantly correlated with the MKSD FA (R^2>0.94, p<0.0001).

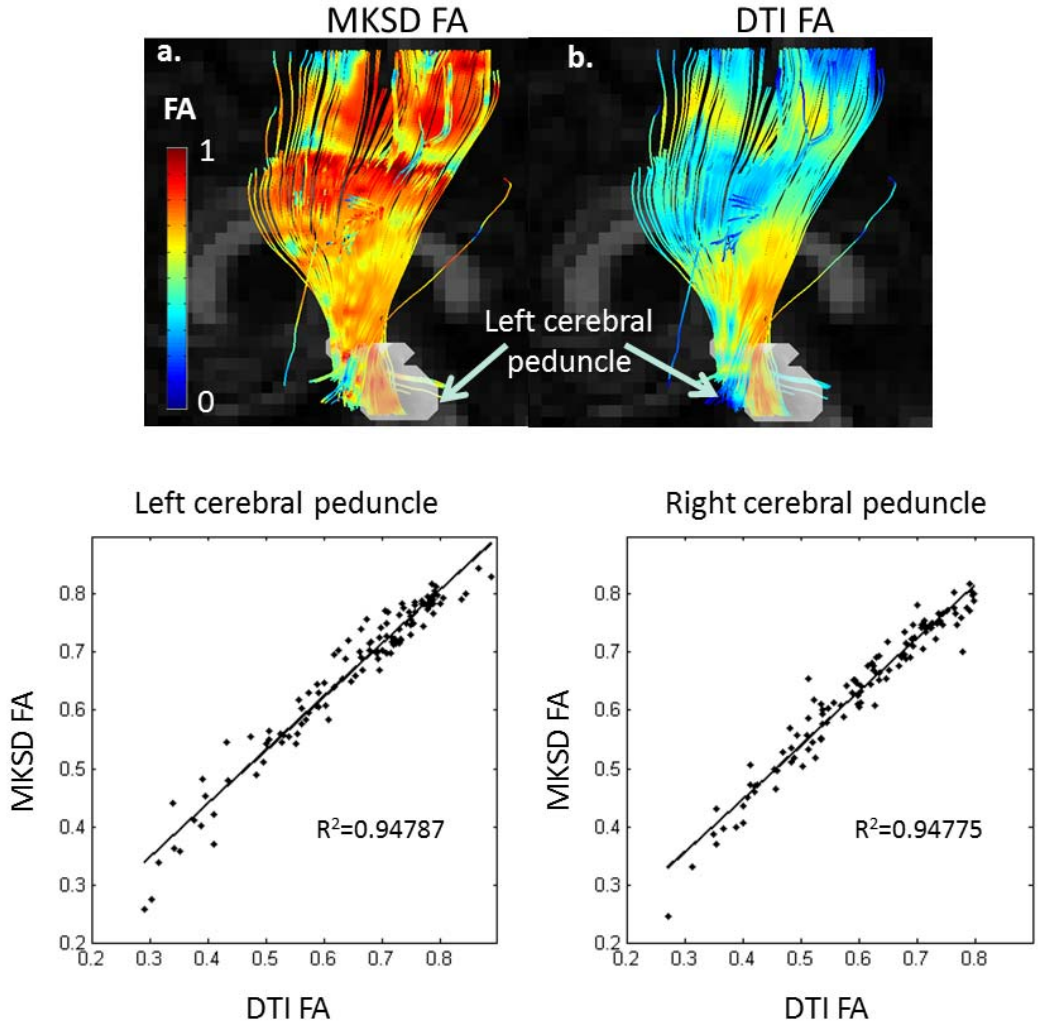

Figure 4. 16. FA estimates by DTI and MKSD. In the upper panel, the FA estimated by MKSD and DTI is shown on a sagittal view of the left cortical spinal tract. In the lower panel, the correlation between DTI FA and MKSD FA in the cerebral peduncle (rendered in transparent gray) is shown for each side separately. Note the high correlation of FA values between methods in coherent fibers.

4.3.2.3. Confidence estimated by residual bootstrap

The bootstrap results for six consecutive voxels in the SLF (interdigitating with CF) are shown in Figure 4.17, which demonstrates spatially smooth FA values that are

larger than those of the partial volume averaged single tensor model (shown in blue) in the right panel.

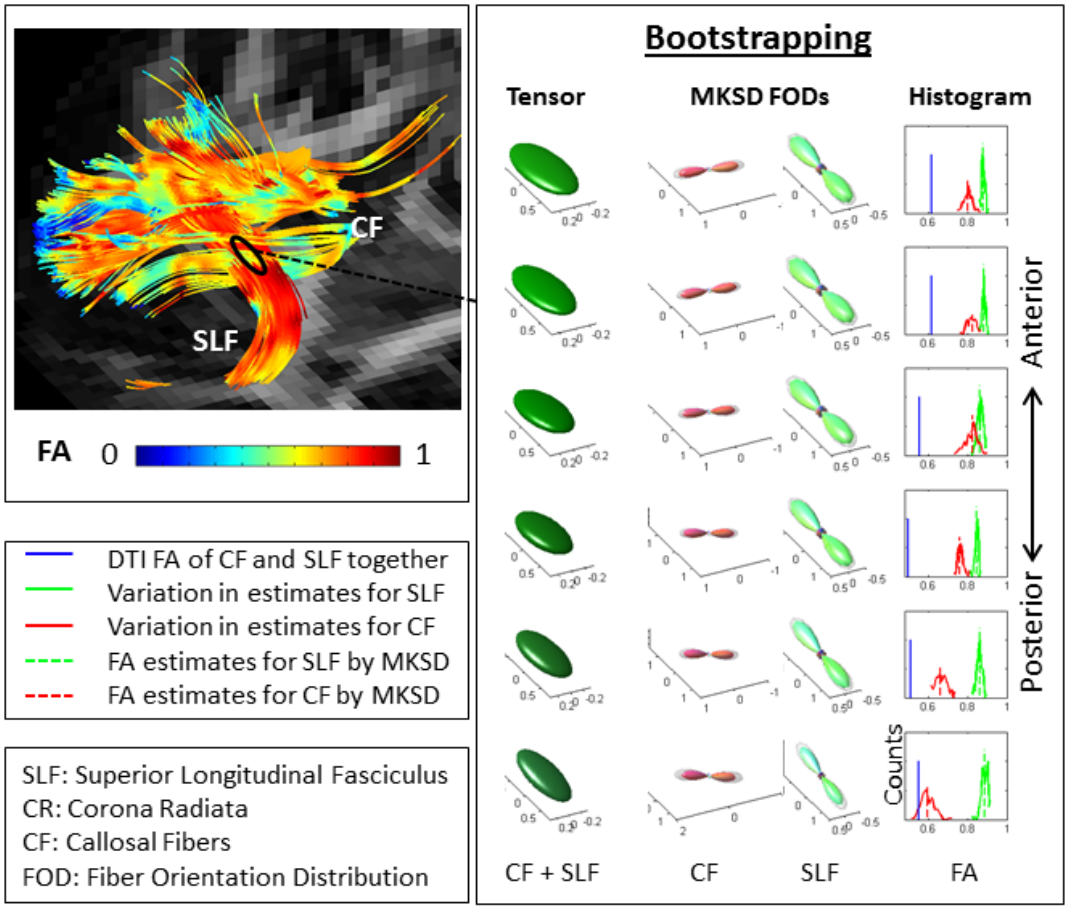

Figure 4. 17. MKSD FODs and stability of the estimates. Six consecutive voxels in the SLF (interdigitating with CF) demonstrate higher FA values than estimated from the partial volume averaged single tensor model (shown in blue) in the right panel. DTI tensors and FODs pertaining to CF (red) and the SLF (green) are also shown. Transparent gray surfaces around the FODs show the mean plus three times the standard deviation over bootstrap trials.

4.3.2.3. Cross-talk between fiber compartments

The individual iterations of the bootstrap corresponding to the voxels shown in

Figure 4.17 are plotted in Figure 4.18. This shows that the errors in FA estimates of one fiber compartment are correlated with the errors in FA estimates of the other fiber compartment, i.e., cross-talk exists when separating signal to individual fiber compartments.

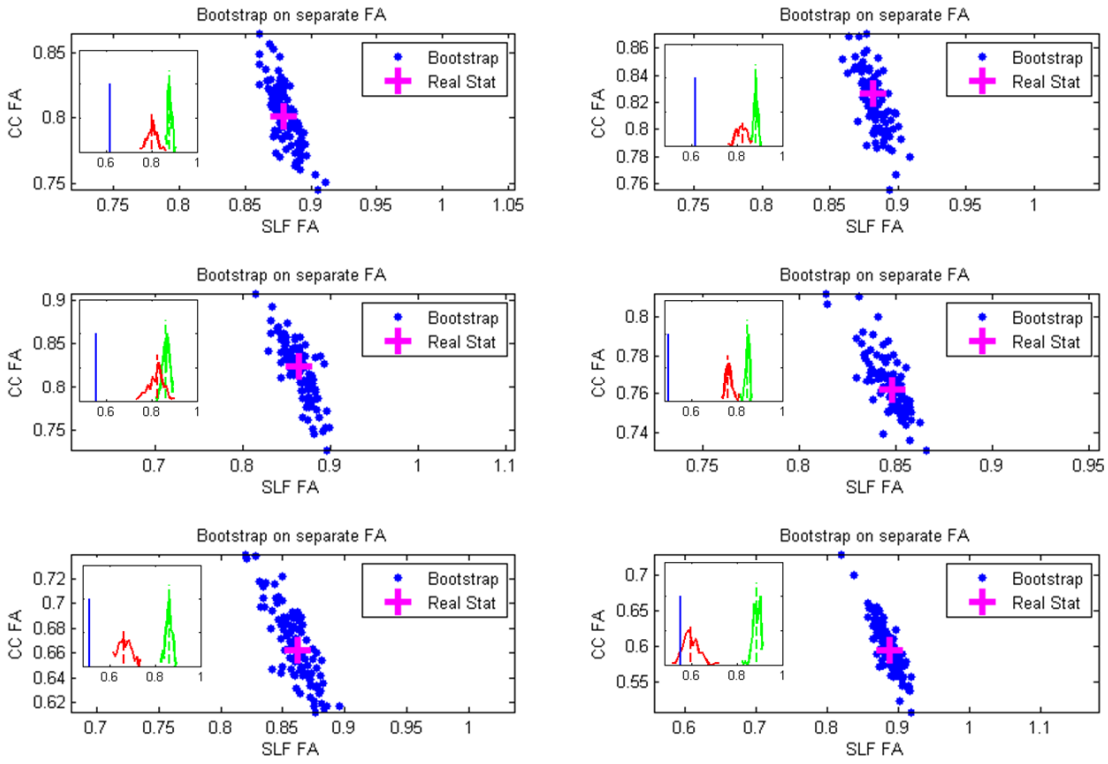

Figure 4. 18. Scatter plot of individual iterations of the bootstrap. The six scatter plots correspond to the six voxels shown in the bootstrap results (Figure 4.17), which were displayed on their left. Each blue dot corresponds to one iteration of the bootstrap sampling, and the pink cross marks the estimates from the original data.

4.3.2.4. Reliability examination using the LMOR approach

Another approach to estimate the reliability of FA estimates is through Jackknife-like resampling, or leave-m-out resampling (LMOR). This method was used to evaluate

reproducibility in an ROI in the left hemisphere where the SLF and CR cross (Figure 4.19a).

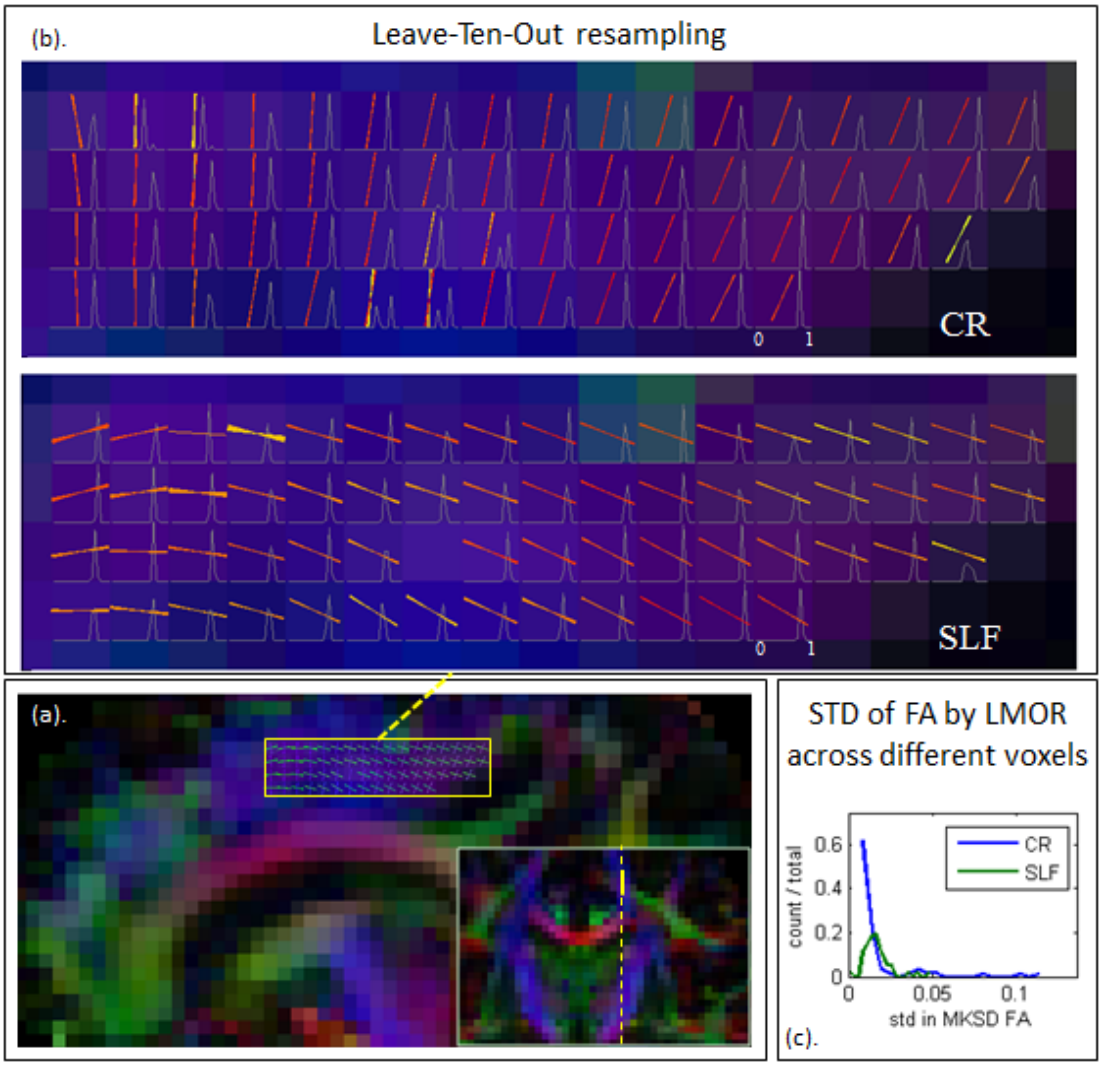

Figure 4. 19. Evaluation of reliability using the LMOR method. An ROI in the left hemisphere was selected where the SLF and CR cross (a). 30 iterations of resampling were performed with 10 randomly drawn data points left out to establish a sampled distribution of fiber orientation and FA estimates. The peaks of these LMOR samples were then assigned to CR or SLF(b). Also plotted in each voxel in gray is a histogram of the FA estimates across LMOR samples corresponding to the CR or SLF.

For each voxel in the ROI, 30 iterations of resampling were performed with 10 randomly drawn data points left out to establish a sampled distribution of fiber orientation and FA estimates. To calculate the standard deviation of FA corresponding to each fiber bundle separately, the multiple peaks of LMOR samples were assigned to CR or SLF (Figure 4.19b). The histogram of FA estimates across LMOR samples were plotted in each voxel with the full range from 0 to 1. A standard deviation for each voxel was calculated for the CR and SLF separately, and the distribution of standard deviations (STDs) across all the voxels in the ROI is shown in Figure 4.19c.

4.3.2.5. Impact of small crossing angles

When crossing angles are too small to resolve individual fiber bundles (e.g., two fiber bundles crossing at $<30^{o}$), the fibers are modeled as one loose fiber bundle. In this case, FA estimates are reflections of the loose (divergent) fiber bundle and thus should be interpreted with caution. For example, if the DW acquisition with b = 2000 s/mm^2 was used to determine number of peaks in the FOD, then a horizontal band of relatively low FA values was found on a group of inferior-superior running fibers (putatively in left CR). These values were not consistent with the FA in neighboring voxels along the fibers (Figure 4.20). On the other hand, if the DW acquisition with b = 3000 s/mm^2 was used to determine number of peaks in the FOD, the number of peaks has a smoother spatial

distribution, and the resulting FA estimates show a higher degree of smoothness along fibers as well. Generally, the resolving power at b = 3000 s/mm^2 is better than at lower b values (as can be seen by comparing the number of peaks detected in the top panels of Figure 4.20). The improved results based on b = 3000 s/mm^2 peak detection suggest that the dip in FA along the fibers is an artifact of unresolved peaks in the FOD, which appear as a single divergent peak with anomalously low FA.

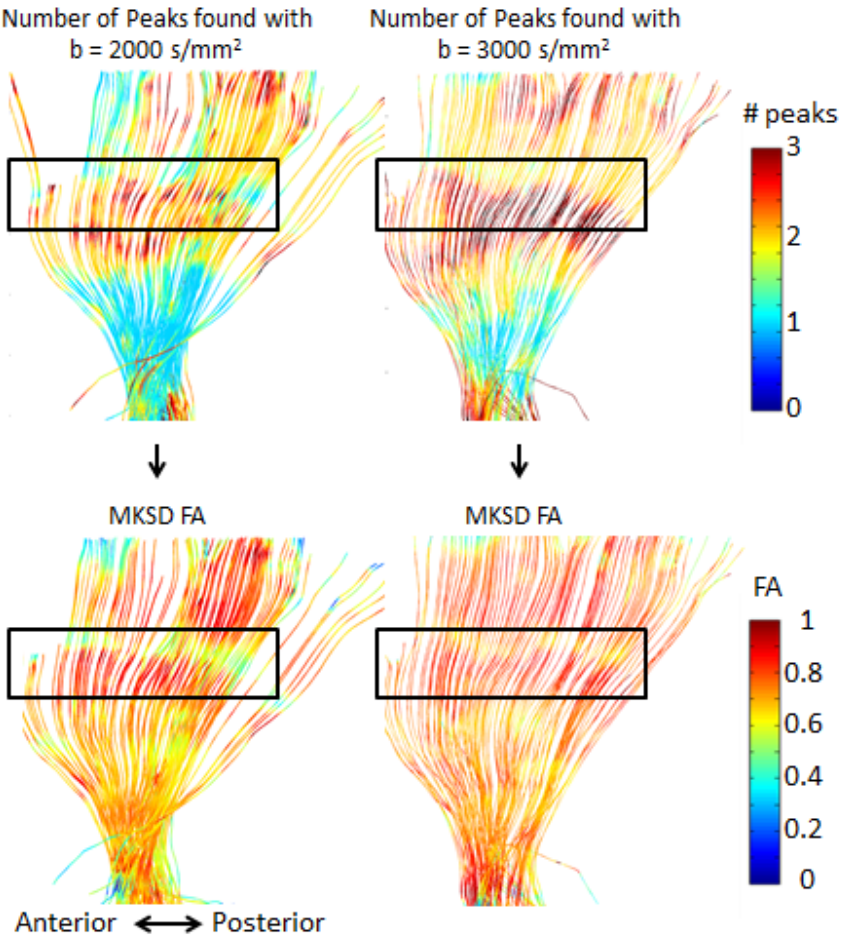

Figure 4. 20. Impact of small crossing angles on FA estimation. A single shell (i.e., *b* value) of DW data was used to identify number of peaks in each voxel using the iterative spherical deconvolution algorithm (Dell'Acqua at al., 2007) with b = 2000 s/mm^2 and b = 3000 s/mm^2 respectively (upper panel). The corresponding FA estimates are shown in the lower panel. Comparison of the top and bottom panels shows that an underestimation in the number of peaks will yield underestimation in FA, i.e., the lower FA reflects a divergent fiber bundle comprised of two or more fiber bundles crossing at a small angle between.

A follow up analysis showed that the horizontal blue band found in the MKSD FA rendered on superior-inferior oriented fibers shown on the lower left of Figure 4.20

originates from interdigitating callosal fibers (Figure 4.21).

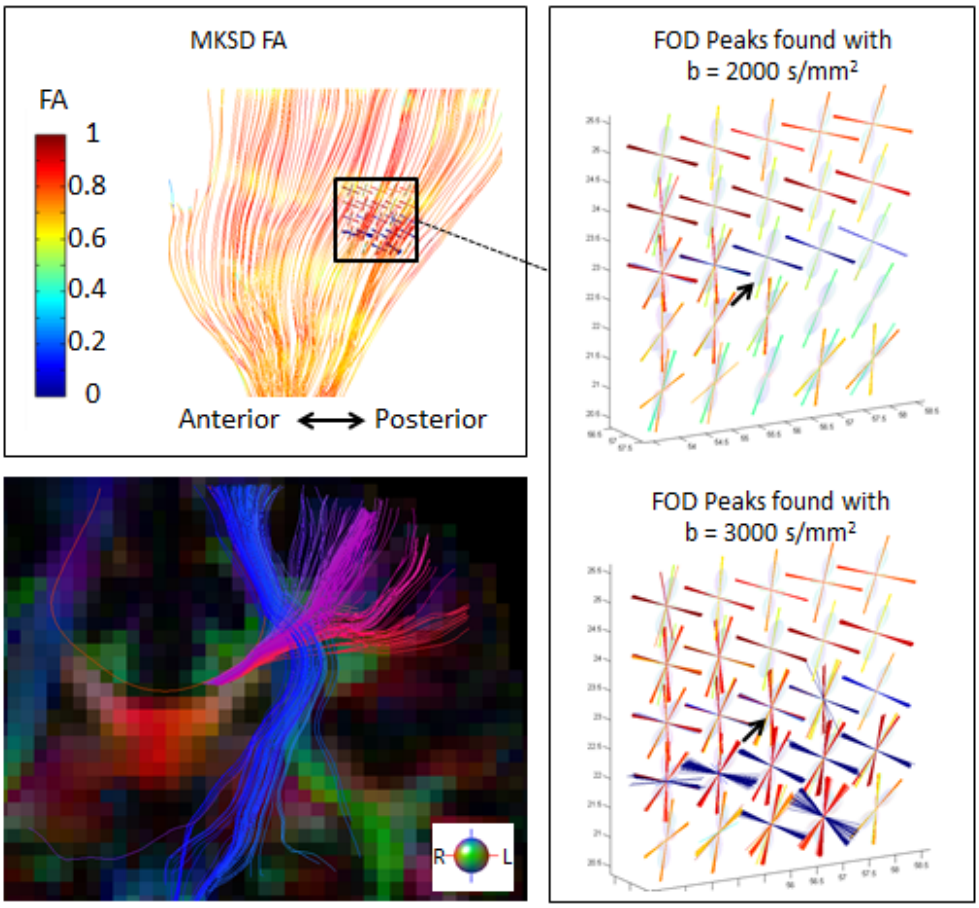

Figure 4. 21. Impact of small crossing angles between the CR and callosal fibers on FA estimation. An ROI on a lateral plane was selected to run Jackknife analysis using the LMOR approach. For each iteration out of 50 in total, ten data points corresponding to ten DW directions were left out, and the rest of the data points were included for FOD peak identification and FA estimation. With b = 2000 s/mm^2 data, crossing bundles with small angles were more likely to be modeled as one fiber bundle with lowered FA; while with b = 3000 s/mm^2 data, crossings were more likely to be detected and the FA estimates were more consistent with the neighborhood. The black arrow points to a voxel where the peaks aligned with CR and callosal fibers cannot be identified with b = 2000 s/mm^2 data, but can be reliably identified with b = 3000 s/mm^2 data.

As shown in Figure 4.21, the callosal fibers projecting laterally and superiorly

into the cortex form a continuous fanning in the coronal plain, and consequently the crossing angles between CR and callosal fibers range from 0^o (i.e., joining to form one bundle) to 90^o (i.e., laterally projecting callosal fibers and perpendicular CR fibers). When the crossing angle decreased gradually to reach the threshold at which the crossing can no longer be identified, the two bundles were reckoned as one fiber bundle; yet, the crossing angle was large enough to be reflected as the lowered FA value. As the crossing angle decreased further, for example, the two fiber bundles form one large bundle running in parallel, the FA reflected the property of this large fiber bundle, and the contribution from crossing diminished.

4.4. Discussion and conclusion

In this work, the MKSD method is proposed as a way to resolve crossing fiber bundles and estimate their intrinsic diffusivity properties. We showed that the MKSD framework has the flexibility to decrease or increase model parameters depending on the tradeoff in practice between scanning time and the amount of information/precision desired for specific research questions. The effects of various factors, including SNR, intrinsic diffusivities, and geometry of complex white matter structures were studied through Monte Carlo simulation. We also demonstrated with *in vivo* data that the MKSD

approach can provide reasonable FA estimates along anatomically well-defined white matter structures.

In the Monte Carlo simulation of FA estimates, as SNR increases, the variability of FA estimates decreases for all MKSD models. No obvious effect of intrinsic mean diffusivity on the variability was observed. In addition, when other conditions are identical, higher intrinsic FA leads to greater robustness to noise.

By allowing for axially symmetric splay, the number of degrees of freedom decreases by 4 and 6 for the 2-fiber and 3-fiber cases, respectively. As a result, the observed variation in FA estimates increases. At SNR=50, the bias in FA towards underestimation might be due to the forced restriction in the nonlinear search algorithm. For example, the higher limit for FA was set to 1. As a result, the right tail of the distribution was squeezed, which lead to a skewed distribution towards the left.

It was demonstrated that intrinsic FA could be estimated by MKSD with fanning or splaying crossing fiber bundles. It is worth noting that fanning in the FOD tends to yield underestimated FA. This might be a reflection of cross-talk (i.e., covariance) between the FOD geometry and intrinsic fiber anisotropy. For example, in the noise-free situation, signal contrast from DW measurements with different *b* values provides a way to differentiate (a) high intrinsic FA with fiber splay and (b) low intrinsic FA with no fiber

splay. However, when noise is present, FA could be confounded with coherence of axonal fiber axes (i.e., in the tensor model, any axonal splay/fanning is reflected in lower FA). In this particular case, when the maximum order l_{max} = 6 is used, as shown in Figure 4.10-4.11, the planar fanning is not well represented with up to 6th order terms, or in other words, there is limited contrast resulting from planar fanning. However, the effect on the FOD perpendicular to the fanning plane was decreased width, which if misinterpreted as axial coherence, would result in underestimated intrinsic FA.

For the *in vivo* examination, we found good agreement between FA estimated from the DTI and MKSD methods in regions where only one fiber bundle is present. It is worth noting that at lower FA (FA<0.5), the MKSD FA was higher than DTI FA; however, the discrepancy diminished at higher FA (FA~0.8). It is likely that at lower FA, the DTI FA is underestimated due to partial volume effects with isotropically diffusing tissues, while MKSD analysis models the isotropic compartment. At higher FA, however, the high FA itself is a sign of less partial volume averaging, and thus the two estimates coincide better.

We also observed cross-talk (covariance) between FA estimates of co-existing fiber bundles in the bootstrap analysis. The MKSD analysis relies on identification of contributions from each fiber bundle. The cross-talk might be due to errors in this

separation of signal contributions. For example, an overestimated FA for one fiber bundle due to noise will likely coincide with an underestimated isotropic contribution from this fiber bundle. Assuming the total isotropic signal contribution is divided between two fiber compartments, the other fiber bundle will be assigned with more than the true value, which favors an underestimated anisotropy estimate.

Another limitation of MKSD is vulnerability to errors in peak number estimates. At lower crossing angles (i.e., $<30^{o}$), where crossing could not be identified by the preprocessing algorithm, the FA estimates obtained from MKSD analysis should be interpreted with caution.

In summary, the MKSD method can provide intrinsic FA estimates of crossing fiber bundles. In regions with a single fiber bundle, MKSD gives results consistent with the tensor model; in regions with crossing fibers, MKSD can provide more information to complement conventional HARDI methods, which focus on fiber orientation. Methods that resolve crossing fibers and provide robust estimates of the fibers' intrinsic diffusion properties may become important tools in neurobiological studies of brain injury, developmental disabilities, as well as normal brain development and aging.

REFERENCES

1. Anderson, A.W., 2005. Measurement of fiber orientation distributions using high angular resolution diffusion imaging. Magn Reson Med 54, 1194-1206.

2. Basser, P.J., Mattiello, J., LeBihan, D., 1994. MR diffusion tensor spectroscopy and imaging. Biophys J 66, 259-267.

3. Behrens, T.E., Berg, H.J., Jbabdi, S., Rushworth, M.F., Woolrich, M.W., 2007. Probabilistic diffusion tractography with multiple fibre orientations: What can we gain? Neuroimage 34, 144-155.

4. Dell'Acqua, F., Rizzo, G., Scifo, P., Clarke, R.A., Scotti, G., Fazio, F., 2007. A model-based deconvolution approach to solve fiber crossing in diffusion-weighted MR imaging. IEEE Trans Biomed Eng 54, 462-472.

5. Dell'acqua, F., Scifo, P., Rizzo, G., Catani, M., Simmons, A., Scotti, G., Fazio, F., 2010. A modified damped Richardson-Lucy algorithm to reduce isotropic background effects in spherical deconvolution. Neuroimage 49, 1446-1458.

6. Jansons, K., Alexander, D., 2003. Persistent Angular Structure: New Insights from Diffusion MRI Data. Dummy Version. In: Taylor, C., Noble, J.A. (Eds.), Information Processing in Medical Imaging. Springer Berlin Heidelberg, pp. 672-683.

7. Jenkinson, M., Beckmann, C.F., Behrens, T.E., Woolrich, M.W., Smith, S.M., 2012. FSL. Neuroimage 62, 782-790.

8. Jeurissen, B., Leemans, A., Jones, D.K., Tournier, J.D., Sijbers, J., 2011. Probabilistic fiber tracking using the residual bootstrap with constrained spherical deconvolution. Hum Brain Mapp 32, 461-479.

9. Jeurissen, B., Leemans, A., Tournier, J.D., Jones, D.K., Sijbers, J., 2012. Investigating the prevalence of complex fiber configurations in white matter tissue with diffusion magnetic resonance imaging. Hum Brain Mapp.

10. Klingberg, T., Hedehus, M., Temple, E., Salz, T., Gabrieli, J.D., Moseley, M.E., Poldrack, R.A., 2000. Microstructure of temporo-parietal white matter as a basis for reading ability: evidence from diffusion tensor magnetic resonance imaging. Neuron 25, 493-500.

11. Le Bihan, D., Breton, E., Lallemand, D., Grenier, P., Cabanis, E., Laval-Jeantet, M., 1986. MR imaging of intravoxel incoherent motions: application to diffusion and perfusion in neurologic disorders. Radiology 161, 401-407.

12. Netsch, T., van Muiswinkel, A., 2004. Quantitative evaluation of image-based distortion correction in diffusion tensor imaging. IEEE Trans Med Imaging 23, 789-798.

13. Niogi, S.N., McCandliss, B.D., 2006. Left lateralized white matter microstructure accounts for individual differences in reading ability and disability. Neuropsychologia 44, 2178-2188.

14. Parker, G.D., Marshall, D., Rosin, P.L., Drage, N., Richmond, S., Jones, D.K., 2012. A pitfall in the reconstruction of fibre ODFs using spherical deconvolution of diffusion MRI data. Neuroimage 65C, 433-448.

15. Quenouille, M., 1949. Approximate tests of correlation in time series. J Roy Stat Soc Series B 11, 68-84.

16. Rimrodt, S.L., Peterson, D.J., Denckla, M.B., Kaufmann, W.E., Cutting, L.E., 2010. White matter microstructural differences linked to left perisylvian language network in children with dyslexia. Cortex 46, 739-749.

17. Shao, J. and Tu, D., 1995. The Jackknife and Bootstrap. Springer-Verlag, Inc.

18. Scherrer, B., Warfield, S.K., 2010. Why multiple b-values are required for multi-tensor models: evaluation with a constrained log-Euclidean model. IEEE international conference on Biomedical imaging: from nano to Macro. IEEE Press, Rotterdam, Netherlands, pp. 1389-1392.

19. Tournier, J.D., Calamante, F., Gadian, D.G., Connelly, A., 2004. Direct estimation

of the fiber orientation density function from diffusion-weighted MRI data using spherical deconvolution. Neuroimage 23, 1176-1185.

20. Tuch, D.S., 2004. Q-ball imaging. Magn Reson Med 52, 1358-1372.

21. Tukey, J.W., 1958. Bias and confidence in not-quite large samples (abstract).The Annuals of Mathematical Statistics 29, 2, 614.

22. Wedeen, V.J., Hagmann, P., Tseng, W.Y., Reese, T.G., Weisskoff, R.M., 2005. Mapping complex tissue architecture with diffusion spectrum magnetic resonance imaging. Magn Reson Med 54, 1377-1386.

CHAPTER V

CONCLUSION

The work discussed in this dissertation centered on an improved assessment of the reading network in the brain using Diffusion Weighted (DW) MRI.

We first carried out two studies which used Diffusion Tensor (DT) tractography to examine brain connectivity and its association with children's reading ability: one focuses on the putative visual word form area (VWFA) and its connectivity pattern with the rest of the cortical brain, the other focuses on the thalamus and its connectivity with the cortical brain. In the VWFA study, it was found that the architecture of the VWFA connectivity is fundamentally different between TD and RD groups, with TD showing greater connectivity to linguistic regions than RD, and RD showing greater connectivity to visual regions than TD. The central finding of the thalamus study revealed that children with RD have significantly higher thalamo-sensorimotor connectivity, which suggested that sensorimotor function is over-relied upon in children with RD.

In both studies, the RD group was found to be over-connected with the brain regions engaged in lower level information processing as compared to the TD group, i.e.,

visual perception for the VWFA study, and somatosensory and motor cortex for the thalamus study. These results indicate that association areas in the brain, which are responsible for integrating sensory information into a coherent model to support abstract thinking and language, such as inferior temporal, fusiform, orbitofrontal regions etc., comprise an important part of the network that underpins proficient reading in children.

In spite of the abundant information that brain connectivity analysis can provide, it is not a direct measure of the physical properties of the connecting white matter fiber bundles. Diffusion Tensor Imaging (DTI) can provide a direct quantitative description of such properties, but DTI suffers from some fundamental limitations, especially when multiple fiber bundles are present in a single voxel. To address the partial volume effects, the third study focused on developing a new MR method to resolve the crossing between different fiber bundles and at the same time provide estimates of diffusion properties intrinsic to each fiber bundle. Both the Monte Carlo simulation and *in vivo* experimental results have demonstrated that the Multiple Kernel Spherical Deconvolution (MKSD) approach can estimate the FA of different fiber bundles in a voxel. These results demonstrated the potential of MKSD in assessment of the reading network, which is comprised of complex white matter structures, in terms of identification of the real neurocorrelates of behavioral performance.

Currently, the challenge for MKSD to be widely applied to reading and other neurobiological research areas is the long scanning time, i.e., approximately 40 minutes in total, especially if the population of interest is young children. To decrease the scanning time, accelerated imaging techniques may provide an opportunity. Actually, some accelerating techniques have already been demonstrated to be effective in reducing acquisition time for diffusion imaging, such as simultaneous multi-slice echo planar imaging (Feinberg et al., 2010; Feinberg and Setsompop, 2013; Setsompop et al., 2012), and compressed sensing (Landman et al., 2010, 2012). With the maturation of these techniques, we hope that the MKSD approach will finally find its significance in reading and similar neurobiological studies.

REFERENCES

1. Feinberg, D.A., Moeller, S., Smith, S.M., Auerbach, E., Ramanna, S., Gunther, M., Glasser, M.F., Miller, K.L., Ugurbil, K., Yacoub, E., 2010. Multiplexed echo planar imaging for sub-second whole brain FMRI and fast diffusion imaging. PLoS One 5, e15710.

2. Feinberg, D.A., Setsompop, K., 2013. Ultra-fast MRI of the human brain with simultaneous multi-slice imaging. J Magn Reson.

3. Landman, B.A., Bogovic, J.A., Wan, H., El Zahraa ElShahaby, F., Bazin, P.L., Prince, J.L., 2012. Resolution of crossing fibers with constrained compressed sensing using diffusion tensor MRI. Neuroimage 59, 2175-2186.

4. Landman, B.A., Wan, H., Bogovic, J.A., Bazin, P.L., Prince, J.L., 2010. Resolution of Crossing Fibers with Constrained Compressed Sensing using Traditional Diffusion Tensor MRI. Proc Soc Photo Opt Instrum Eng 7623, 76231H.

5. Setsompop, K., Cohen-Adad, J., Gagoski, B.A., Raij, T., Yendiki, A., Keil, B., Wedeen, V.J., Wald, L.L., 2012. Improving diffusion MRI using simultaneous multi-slice echo planar imaging. Neuroimage 63, 569-580.

APPENDIX A

LIST OF PROGRAMS USED

The purpose of this appendix is to provide a description of the MATLAB scripts that were written for data analysis related to the project discussed in Chapter IV of this dissertation

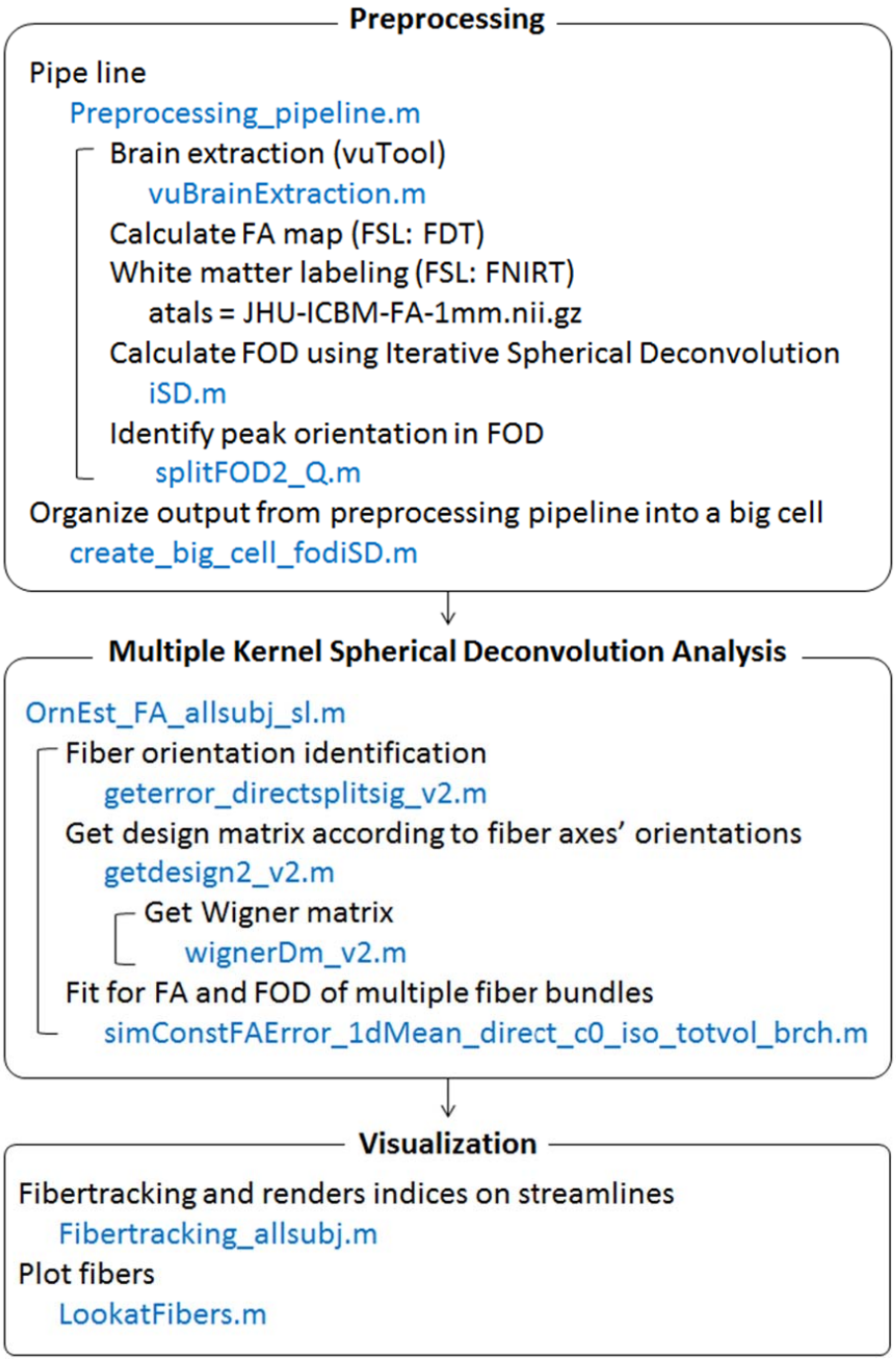

Figure A. 1. Flow chart of list of programs used. The names of the MATLAB functions are listed in blue, and were categorized into preprocessing, analyzing and visualization categories.